Nonlinear Photonics with Applications in Lightwave Communications

By

UMAIR AHMED KORAI BALOCH

Submitted in fulfilment of the requirements for the degree of

Doctor of Philosophy

Department of Electronic and Electrical Engineering

University of Strathclyde

2020

Certificate

This thesis is the result of the author's original research. It has been composed by the author and has not been previously submitted for examination which has led to the award of a degree.

Umair Ahmed Korai Baloch

Date: 4 March 2020

This thesis is dedicated to my supervisors, parents, brother, and friends who have supported me throughout

Acknowledgements

In the name of ALLAH, the most Beneficent and the most Merciful. ALLAH belongs [all] praise - Lord of the heavens and Lord of the earth, Lord of the worlds (Quran 45:36). First and foremost, praise is to ALLAH, who has given me an opportunity to study the doctorate of philosophy degree at the University of Strathclyde, Glasgow, UK. He Himself mentioned that “Indeed, with hardship [will be] ease (Quran 94:6)”.

PhD was a dream of my father, Ghulam Mustafa Korai (late). Whatever I am today is just because of his constant support, motivation and cherish talk. I was in 2nd year of my PhD when he passed away but he is always in my memory and his motivated words are always in my mind like whisper of the breeze.

I would like to thank my supervisor, Professor Ivan Glesk, who supported me throughout my PhD time. He helped me like a colleague in my experiments, guided me, and he is always keen to provide information which is beneficial for me. I am extremely thankful to him for providing an opportunity to work under his supervision for the PhD degree in Electronic and Electrical Engineering. He has supported me a lot during the hardest days of my life and didn’t put any work pressure on me.

I would like to thank my co-supervisors, Dr Michael J. Strain and Dr Vladimir Stankovic who helped me throughout my thesis. I specially thank to Dr Michael who assisted me for the first experiment and trained me for the nonlinear optical communication. Indeed, he is the one who introduced nonlinear optics to me. I would also like to thank Professor Lawrence R. Chen for providing massive guidance, help

and for arranging experimental setups at the McGill University. I would also like to thank Dr Aitor V. Velasco from National Research Council, Spain, who propped me to understand the concept related to the subwavelength structure of the waveguide. I would like to thank Prof Ivan, Dr Helena Gleskova, Dr Lina Stankovic and Dr Vladimir for providing an opportunity and fund for my McGill University study exchange visit for 06 months.

I am very thankful to my sponsor, the Commonwealth Scholarship Commission, United Kingdom, for financing me to study the PhD degree at the University of Strathclyde and supported me during the days of my father's death. Indeed, without the support of my family, supervisor, and my sponsor (the Commonwealth Scholarship Commission), this would not have been possible.

I am very grateful and thankful to all my friends, colleagues at Strathclyde University and McGill University, who not only boosted me in my PhD but also cheered me up every time whenever I lose my hope by having long laugh, a cup of tea/coffee, sharing a meal and so forth. There is a long list of my friends but the closer one's are: Alan, Dr Stuart, Jiangfeng, Mohamad Abuhelala, Dr Shakil, Dr John, Dr Paul, Dr Anderson, Sami, Arif, Dr Eslam, Bruno, Dr Reza, Hao and many more…

Lastly, I would like to thank my family members. Despite of major loss of all of us, my mother (Fahmida Korai Baloch) and brother (Fahad Ahmed Korai Baloch) allowed me to continue my studies. Thank you all for playing a significant role in my PhD degree and life.

Author’s declaration

I declare that all the work presented in this thesis has been carried out by me, unless otherwise acknowledged.

Umair Ahmed Korai Baloch

04 March 2020

Abstract

This doctoral dissertation investigates the use of nonlinear photonics in targeted Lightwave communication applications. Different highly nonlinear optical materials have been considered for the investigation of Lightwave communications data carriers, with a focus on the optical carrier pulsewidth. A state-of-the-art novel method has been developed to measure pico-second optical carrier pulses using highly nonlinear optical fiber. This method is based on the nonlinear optical loop mirror (NOLM), with consideration focused on the third order nonlinearity. Silicon is considered to be one of the most attractive materials for photonics integrated circuit technology (PIC) due to its compatibility with complementary metal oxide semiconductor (CMOS). As such, the method has been applied to the SOI platform Mach-Zehnder interferometer (MZI), also by considering the third order nonlinearity.

In the NOLM approach, the picosecond optical data carrier pulsewidth is measured by using an optical power meter. Simulations for both the self-phase and cross-phase modulation schemes are carried out, and as expected, the cross phase modulation gives an increment in the sensitivity twice that of the self-phase modulation. Due to very high repetition rates of the order 10 GHz, the effect of counter propagating non-linear interactions in the NOLM are also considered in the theoretical evaluation. In the experimental validation, the pulses from an active fiber mode-locked laser at a repetition rate of 10 GHz were incrementally temporally dispersed using an SMF–28 fiber. The optical data carrier pulses over a range of 2–10 ps were successfully measured with a resolution of 0.25 ps. By extrapolating the theoretical

evaluation and by selecting different physical parameters for the setup, the method was found to exhibit an extended range of 0.25 to 40 ps.

The concept described above is then extended to the investigation of nonlinear SOI devices using an MZI, thus miniaturizing the setup. In this investigation, the silicon waveguide has been simulated for self-phase and cross-phase modulation by solving the nonlinear Schrodinger equations using the split step method. Silicon has strong two photon absorption at telecommunication wavelengths, i.e. 1550 nm, and therefore all nonlinear losses (i.e. TPA and free carriers generated through TPA) are included in the split step simulations. The results obtained show that the on-chip nonlinear MZI (based on the SOI platform) can also be used for the measurement of optical data carrier pulse-widths of up to 10 ps.

In the last part of this doctoral dissertation, a novel design for a temperature insensitive MZI is presented. Temperature dependence is one of the main challenges in the design of the SOI platform due to the large thermo-optic coefficient of its core material. A change in temperature can cause the device properties to deviate significantly, and can also alter the nonlinear properties of the device. Therefore, a design of an all-passive athermal MZI device based on the SOI platform has been developed and investigated. The MZI's temperature compensation is achieved by optimizing the relative length of the wire and subwavelength grating arms, and by tailoring the thermal response of the subwavelength structure. The simulation results of the athermal MZI design indicated that an overall temperature sensitivity of 7.5 pm/K could be achieved over a 100 nm spectral range near the 1550 nm region.

Table of contents

List of figures

List of tables

Abbreviations:

CIR	Optical circulator
CMOS	Complementary metal oxide semiconductor
CW	Continuous wave
CWDM	Coarse wavelength division multiplexer
DC	Duty cycle
DCA	Digital communication analyzer
DIC	Directional coupler
EDFA	Erbium-doped fiber amplifier
FCA	Free carrier absorption
FCD	Free carrier dispersion
FROG	Frequency resolve optical gating
FSO	Free space optics
FSR	Free spectral range
FT	Fourier-transform
FWM	Four wave mixing
GVD	Group velocity dispersion
HNLF	Highly non-linear fiber
ISI	Inter symbol interference
LAN	Local area network
Li-Fi	Light-fidelity
MMI	Multimode interference
MZI	Mach-Zehnder interferometer
NLSE	Nonlinear Schrodinger equations
NOLM	Nonlinear optical loop mirror
OA	Optical attenuator
OAC	Optical auto-correlator
OPD	Optical path differences
OSA	Optical spectrum analyzer
OWC	Optical wireless communication

PC	Polarization controllers
PIC	Photonic integrated circuits
PROUD	Phase reconstruction using optical ultrafast differentiation
RF	Radio frequency
SNOI	Silicon nitrite on insulator
SNR	Signal-to-noise ratio
SOI	Silicon on insulator
SPIDER	Spectral phase interferometry for direct electric-field reconstruction of ultra-short optical pulses
SPM	Self phase modulation
SRN	Silicon rich nitrite
SWG	Subwavelength grating
TE	Transverse electric
TPA	Two photon absorption
UV	Ultraviolet
VLC	Visible light communication
VLSI	Very large scale integration
VLSMF	Variable length single mode fiber
WDM	Wavelength division multiplexing
XPM	Cross phase modulation

List of Publications

Journal Papers

1. M. Abuhelala, **U. A. Korai**, A. Sanches, W. C. Kwong, and I. Glesk, "Investigation of SOA induced frequency shift on 2D-WH/TS OCDMA code carriers," *IEEE Photonics Technology Letters* (under review).
2. **U. A. Korai**, A. H. Bermello, M. J. Strain, I. Glesk, and A. V. Velasco, "Design of an Athermal Interferometer Based on Tailored Subwavelength Metamaterials for On-Chip Microspectrometry," *IEEE Photonics Journal*, Vol. 11, No. 6, Dec. 2019, DOI: 10.1109/JPHOT.2019.2943774.
3. **U. A. Korai**, Z. Wang, C. Lacava, L. R. Chen, I. Glesk, and M. J. Strain, "Technique for the measurement of picosecond optical pulses using a non-linear fiber loop mirror and an optical power meter," *Optics Express*, Vol. 27, Issue 5, pp. 6377-6388, January 2019, https://doi.org/10.1364/OE.27.006377

Conference Papers/Posters

1. **U. A. Korai**, A. H. Bermello, M. J. Strain, I. Glesk, and A. V. Velasco, "Temperature Insensitive Waveguide Interferometer Based on Subwavelength Gratings," *2nd IEEE British and Irish Conference on Optics and Photonics* (*IEEE-BICOP*), London, 2019.

2. **U. A. Korai**, Z. Wang, C. Lacava, L. R. Chen, M. J. Strain, and I. Glesk, "Measurement of Optical Pulsewidth in the Picosecond Regime Using a Non-linear Fiber and Power Meter," *Conference on Lasers and Electro-Optics (CLEO)*, San Jose, CA, 2019, paper SW3H.5, https://doi.org/10.1364/CLEO_SI.2019.SW3H.5.

3. **U. A. Korai**, M. J. Strain, I. Glesk, "Nonlinear effects in silicon waveguides," *8th SU2P Annual Symposium*, Heriot-Watt University, 2017.

4. **U. A. Korai**, L. Luini, R. Nebuloni, and I. Glesk, "Statistics of attenuation due to rain affecting hybrid FSO/RF link: Application for 5G networks," *11th European Conference on Antennas and Propagation* (*EUCAP*), Paris, 2017, https://doi.org/10.23919/EuCAP.2017.7928821.

Chapter 1

Introduction

The Lightwave communication is considered as the backbone of the modern data networks. The Lightwave communication systems are continuously evolving to provide the high speed data networks which can fulfil the future demands of the users. As per the visual networking index of Cisco, the global IP traffic will nearly triple from 2017 to 2022 [1]. This demand is continuously increasing due to the increasing number of wideband applications such as cloud services (i.e. Dropbox or Google Drive) and virtual reality. Therefore, in order to fulfil the demands of the users, Lightwave communication system is the best choice. Since this system is continuously evolving, therefore, due to the high bandwidth capability of current Lightwave communication systems, one can access any sort of information in a matter of seconds

[2]. In order to design a Lightwave communication system, which can provide the capacity that is approaching to zettabyte threshold [3], one has to increase the metro and core network capacities which correspondence to increase in capacity of the access network of the system. A typical Lightwave communication system is shown in Figure 1.1 [2].

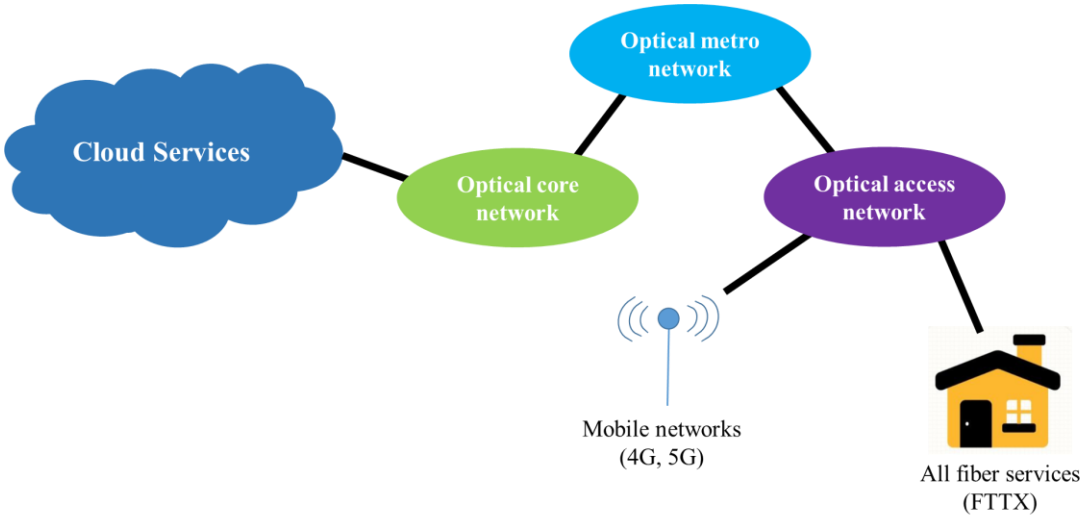

Figure 1.1: *A typical diagram of a Lightwave communication system, where FTTX – fiber to the (home, building curb…), 4G – fourth generation mobile network, 5G – fifth generation mobile network.*

The communication through Lightwave can be possible by using optical fiber [4], and free space optics (FSO), which is also known as optical wireless communication (OWC) [5], (this includes visible light communication (VLC) [6] and invisible light communication [7]). The eye safety risk must be considered while using the OWC as mentioned in [8].

OWC is a type of Lightwave communication in which the optical signal, i.e. visible, infrared or ultraviolet (UV) band, is propagated in an unguided propagation medium. The VLC communication is best suited for the short range communication.

It has been proposed that the VLC communication can be one of the possible source of communication for the 5G networks [9], [10] where it can also be used for light-fidelity (Li-Fi), which mean that the home lamps or the LED bulbs will be considered as the access point for providing the internet services [11]. Therefore, the VLC networks can be used either for indoor communication [12] or for short range outdoor communication.

The OWC using invisible laser, also known as FSO, provides high data rate communication between two fixed points and can cover the range up to few kilometers. The FSO links has high bandwidth range in comparison with the radio frequency (RF) communication, hence this allows communication at much higher data rates. The FSO links can be used for the wide range of applications such as local area network (LAN) to LAN connectivity, fiber back-up, backhaul for wireless cellular networks, disaster recovery, high definition TV and medical image/video transmission, wireless video surveillance/monitoring, and many others [13]. Despite of all these advantages, the OWC (both VLC and FSO) is very sensitive to the weather changes. According to [7], the fog effect can attenuate the FSO signals up to 300 dB/km. In the areas where fog is not an issue, rain can be the important weather parameter and can limit the signal coverage severely [14]. In order to improve the signal coverage, one option is to increase the power level of the free space laser signal but the power levels cannot be increased beyond a certain limits set by international electro technical commission standards based on the affection of human eye at some particular wavelength (i.e. 10 mW power for Class 1 M laser in 1550 nm wavelength) [15].

The communication using optical fiber is a traditional way for transmitting the data from one point to another and provides enormous advantages, i.e. very high

bandwidth, reliable, and immune to electromagnetic waves interference. Mostly the core networks of every communication system (guided or unguided) is inter-connected by using optical fiber. The fiber optics communication systems use the optical fiber for transmitting the data from one point to another in form of light signals. The light signals can be visible or invisible. Usually, the signal in optical fiber is propagated at the wavelength windows of 1310 nm and 1550 nm due to low loss. Losses in optical fibres vary for different wavelength bands and there are several factors (such as material absorption and Rayleigh scattering) that contributes to high losses on wavelength bands other than 1310 and 1550 [4]. The wavelength of 1550 nm exhibits very low losses hence the wavelength range near 1550 nm is considered as the telecommunication wavelength whereas the wavelength near 1310 nm is considered as a zero dispersion wavelength [4]. The optical fiber can be used for various application including dispersion compensation [16], nonlinear effects [17], [18], sensing [19] and many more applications [20], [21].

Photonic integrated circuit (PIC) [22] is a technology in which several optical devices, made of different platforms (such as silicon on insulator, lithium niobate on insulator and so forth) are fabricated in one single chip with dimension ranges from 10s to 100s of millimeters. The most commonly used platforms are silicon on insulator (SOI), silicon nitrite on insulator (SNOI), polymers, and lithium niobate. This technology is similar to electronics in which many circuits are combined in a chip. Like electronic chip, in PIC several devices are fabricated onto a single chip and this chip is known as photonic chip. The difference between an electronic and photonic chip is that in photonic chip the devices use the Lightwave signal on optical wavelengths, typical in visible or infrared regions whereas in electronic chip, electrical

current, voltage at different frequency band is used. The PIC can be used in optical network for various linear and nonlinear applications including, wavelength division multiplexing [23], wavelength conversion [24], nonlinear switching [25] and many more [26]–[29].

High bandwidth applications require Lightwave communication based infrastructure and advanced networking technology. One key part of this is the monitoring of ultra-short pulses across the network. So it is advantageous to use low power, point of use devices rather than large laboratory equipment as feedback monitoring. A good way to achieve this is through non-linear all optical devices. In this thesis, a technique for picosecond pulse width measurement using the highly nonlinear optical fiber and PIC has been presented. Within the PIC, we have considered only SOI platform for the nonlinear photonic application. The SOI platform is the combination of silicon and silicon oxide materials. It is one of the highly cited platforms due to its extensive advantages. Few of them are: the SOI platform is compatible with complementary metal oxide semiconductor (CMOS) fabrication technology, which means that the photonic and electronic chip can be fabricated on the same chip, it offers a high mode confinement due high refractive index contrast between silicon and silica material therefore, the single mode operation can be achieved with submicron dimensions, thus making this platform attractive for the applications in telecommunication [30], [31], bio-sensing [32] and quantum optics [33]–[35].

Pulse width measurement is one of the key challenges and is still being explored by many researchers. Due to limited bandwidth availability of the electronics, the optical oscilloscope is unable to accurately measure the pulse width less than 10

ps. In this thesis, my contribution is to introduce another method which can measure the pico-second pulse width using a nonlinear medium and a power meter. Therefore, we have developed a method which uses the nonlinear optical loop mirror comprises of highly nonlinear optical fiber as a nonlinear medium and an optical power meter to measure the desired optical pulse width. The experimental characterization along with the simulation has been carried out using a highly nonlinear optical fiber and a power meter. In order to miniaturize the whole setup, this method is further extended for PIC using SOI platform. The modelling of pulse width measurement using SOI platform is presented in the thesis. The silicon waveguide is modelled by solving the nonlinear Schrodinger equations (NLSE) using split step method.

Temperature plays a very important role in PIC technology. Change in the temperature can alter the performance of the device significantly. Since silicon has a very high temperature coefficient, i.e. $1.86 \times 10^{-4} K^{-1}$ for TE polarization[36], hence small change in the temperature can change the behavior of the device, and therefore, the nonlinear properties of the material will change too. There are various methods to compensate for the effects of temperature, some of the methods use the active elements to control the change in temperature [37] but this approach require external power and space and hence can increase the cost of fabrication. Some methods are based on the usage of polymer as cladding [38] as it has negative thermo-optic coefficient, and can compensate the thermo-optic response of the device by appropriately choosing the width and height of the polymer cladding but this solution is limited by the polymer dependence on changing environment conditions such as the moisture or mechanical pressure [39]. In this thesis, we have shown a design of a novel SOI platform based device using wire and subwavelength grating (SWG) [40] waveguide which can

passively compensate the thermo-optic effect. Thus, the change in the temperature will not vary the property of the device, therefore, the nonlinear properties of the device will remain constant.

Within the presented scenario, this doctoral dissertation is therefore focused on the development of a state-of-the-art method which is simple to use, and can be portable for the measurement of the optical pulse width using the highly nonlinear optical fiber and an optical power meter. The concept of this method is also analyzed for SOI platform by analytically solving the nonlinear Schrodinger equation(s) using split step method. Furthermore, a state-of-the-art design for temperature insensitive device is presented in this dissertation which can passively compensate the thermo-optic effect. Thus the nonlinear properties will remain constant when there is a change in the temperature.

Thesis outline:

The dissertation is structured as follows:

In Chapter 2, the background theory related to the nonlinear optics is described, precisely the third order nonlinearity along with its application is discussed. Furthermore, the nonlinear Schrodinger equation is derived separately for dispersion and nonlinearity. The split-step method for analytically solving the NLSEs in presence of both dispersion and nonlinearity is discussed later in this chapter.

In Chapter 3, the state-of-the-art method for measuring the picosecond pulse width of an optical signal using nonlinear optical loop mirror (NOLM) and an optical power meter is presented. The NOLM is designed using highly nonlinear optical fiber.

Some of the most common techniques for the measurement of an optical pulse width, including frequency resolve optical gating (FROG) and spectral phase interferometry for direct electric-field reconstruction (SPIDER) of ultra-short optical pulses are also discussed. The experimental results of the proposed method are verified by the theoretically simulating the NLSEs for cross phase modulation (XPM) and self-phase modulation (SPM).

Chapter 4 is about one of the most common platforms which is used in PIC, i.e. silicon photonic technology. The Silicon photonics technology, also known as silicon on insulator platform, is explained along with its different applications in the fields of optics. The refractive index and dispersion relation calculated using Lumerical mode solution are discussed as well. The working principles of the most commonly used devices in PIC, such as: directional coupler (DIC), micro-ring resonator, NOLM and Mach-Zehnder interferometer (MZI), are described along with their simulations' results later in this chapter.

Chapter 5 is an extension of the method discussed in Chapter 3 of this dissertation. In this chapter, the nonlinear MZI based on SOI platform is modelled by solving the NLSEs analytically using split step method for cross phase modulation and self-phase modulation for calculating the pulse width of an optical signal in pico-second regime. The NOLM based on highly nonlinear optical fiber, discussed in Chapter 3, is replaced by a PIC device (i.e. nonlinear MZI) based on SOI platform. This potentially leads to improvements in device miniaturization, stability and power. All the nonlinear losses, i.e. two photon absorption, free carrier absorption and free carrier dispersion, are considered in the split step simulation.

Since the temperature changes the refractive index of the device which can directly alter the nonlinear properties of the device. Therefore, in order to keep the nonlinear properties unaltered due to temperature, a fully temperature compensated device is required. In Chapter 6, a state-of-the-art novel device is presented that can compensate the effect of temperature for SOI technology using the combination of wire and subwavelength grating waveguide. The temperature compensation is introduced by tailoring the subwavelength structure in the MZI. This device is based on SOI platform and passively compensate the overall thermo-optic coefficient of the device hence doesn't require any other component and power to perform the require operation.

Finally, Conclusions about the presented results are given in Chapter 7, together with considerations on future activities and research

Chapter 2

Background Theory and Modelling

The aim of this chapter is to present the background theory and the modelling related to the nonlinear optics, especially the third order nonlinearity and its applications. The modelling of the nonlinear Schrodinger equation is also included in this chapter. The Maxwell's equations of the light are discussed in section 2.1. As this work mainly focuses on the applications of the third order nonlinearity that's why a brief introduction to the 3rd order optical nonlinearity is also given in section 2.2. Furthermore, the generalized equation for the nonlinear optical communication, known as NLSE, has been derived for the self-phase modulation and the dispersion

effects, separately and both are discussed in section 2.3, this section also briefly introduces the effect of cross phase modulation. Since the NLSE contain the nonlinear and dispersion effects simultaneously, therefore, to solve such equation(s) an analytical method, developed by [41] known as split step method, is discussed in later section of this chapter, i.e. section 2.4.

2.1 Maxwell's Equations

The nonlinear optics is the branch of physics in which the medium is dependent on the input power of the light signal. It is very complex field and has range of the application. The main introduction of the nonlinear optics can be started from the Maxwell's equations of the light. The time (t) and space (r) dependent formulation of the Maxwell's equation in the international standard of units is given as [42]:

$$\nabla \times \boldsymbol{E}(\boldsymbol{r},t) = -\frac{\partial}{\partial t}\boldsymbol{B}(\boldsymbol{r},t) \tag{2.1a}$$

$$\nabla \times \boldsymbol{H}(\boldsymbol{r},t) = \boldsymbol{J}(\boldsymbol{r},t) + \frac{\partial}{\partial t}\boldsymbol{D}(\boldsymbol{r},t) \tag{2.1b}$$

$$\nabla . \boldsymbol{D}(\boldsymbol{r},t) = \rho_f(\boldsymbol{r},t) \tag{2.1c}$$

$$\nabla . \mathbf{B}(\boldsymbol{r},t) = 0, \tag{2.1d}$$

where, E and H are the electric and magnetic field vectors, respectively, and D and B are the electric and magnetic flux densities respectively. ρ_f is the free charge density and J is the current density vector. The electric flux density (D) and magnetic flux density (B) are related to the electric field (E) and magnetic field (H) propagating in the medium hence the constitutive relation between the flux densities is given by the following set of equations:

$$\boldsymbol{D}(\boldsymbol{r},t) = \varepsilon_0 \boldsymbol{E}(\boldsymbol{r},t) + \boldsymbol{P}(\boldsymbol{r},t) \quad (2.2a)$$

$$\boldsymbol{B}(\boldsymbol{r},t) = \mu_0 \boldsymbol{H}(\boldsymbol{r},t) + \boldsymbol{M}(\boldsymbol{r},t) \quad (2.2b)$$

where, μ_0 = 0.4π μH/m is the permeability in vacuum and ε_0 = 8.85 pF/m the permittivity in vacuum, $\boldsymbol{P}$ and $\boldsymbol{M}$ is the electric and magnetic polarization induced in the medium. Optical fiber has negligible magnetic polarization, i.e. $\boldsymbol{M}$ = 0, $\boldsymbol{J}$ = 0 and ρ_f = 0 [41]. By taking the curl of equation (2.1a) and using the relation $\nabla \times \nabla \times \boldsymbol{E} = -\nabla^2 \mathbf{E}$ (where $\nabla . D = \varepsilon \nabla . E = 0$) along with equations (2.1b), (2.2a) and (2.2b), the relation can be written as:

$$\nabla^2 \mathbf{E}(\boldsymbol{r},t) = \frac{1}{c^2}\frac{\partial^2 \boldsymbol{E}(\boldsymbol{r},t)}{\partial t^2} + \mu_0 \frac{\partial^2 \boldsymbol{P}(\boldsymbol{r},t)}{\partial t^2} \quad (2.3)$$

where, c is the speed of light in vacuum, i.e. 3×10^8 m/s. The total polarization is given as:

$$\boldsymbol{P}(\boldsymbol{r},t) = \varepsilon_0 \chi \mathbf{E}(\mathbf{r},\mathrm{t}) \quad (2.4)$$

where, χ is the optical susceptibility. This includes the linear and nonlinear polarization which will be discussed in next sections.

2.2 Third Order Nonlinearity

The general relation of the total polarization in terms of linear and nonlinear electric dipoles in the electric field is given as [41]:

$$\boldsymbol{P} = \boldsymbol{P_L} + \boldsymbol{P_{NL}} = \varepsilon_0\left(\chi^{(1)}\mathbf{E} + \chi^{(2)}\mathbf{E^2} + \chi^{(3)}\mathbf{E^3} + \cdots\right) \quad (2.5)$$

where, $\chi^{(1)}$ is the linear susceptibility and $\chi^{(2)}$ and $\chi^{(3)}$ is the nonlinear susceptibility. $\chi^{(2)}$ is the second order nonlinear susceptibility and it has application in sum frequency generation and second harmonic generation [43]. For optical fiber and

waveguides based on SOI platform, $\chi^{(2)}$ is zero due to centrosymmetric structure. The lowest nonlinear order which can be observed in the optical fiber is the third order nonlinearity, i.e. $\chi^{(3)}$ [44]. Therefore, by including the linear and nonlinear polarization, equation (2.4) for optical fiber can be modified as:

$$\boldsymbol{P} = \varepsilon_0\left(\chi^{(1)}\mathbf{E}^1 + \chi^{(3)}\mathbf{E}^3 + \cdots\right) \tag{2.6}$$

Therefore, the overall wave equation (2.3) for optical fiber becomes:

$$\nabla^2\mathbf{E}(\mathbf{r},\mathrm{t}) = \frac{1}{c^2}\frac{\partial^2\boldsymbol{E}(\boldsymbol{r},t)}{\partial t^2} + \mu_0\varepsilon_0\left(\frac{\partial^2\chi^{(1)}(\boldsymbol{r},t)\mathbf{E}^1(\boldsymbol{r},t)}{\partial t^2} + \frac{\partial^2(\chi^{(3)}(\boldsymbol{r},t)\mathbf{E}^3(\boldsymbol{r},t)+\cdots)}{\partial t^2}\right) \tag{2.7}$$

Since this thesis is based on the usage of nonlinear optics using SOI [45] waveguide and optical fiber, from now to onwards only 3rd order nonlinearity will be used throughout this thesis.

2.3 Generalized Nonlinear Schrodinger Equation

In this section, the generalized form of the nonlinear Schrodinger equation [46] will be discussed with the propagation of modes in the optical waveguides (i.e. optical fiber and silicon photonics based waveguide). In addition, the role of dispersion and nonlinearity along with self-phase modulation (SPM) and the cross phase modulation (XPM) effects is also briefly explained.

2.3.1 Mode in Optical Waveguide

Optical medium, such as optical fiber or waveguide based on silicon photonic technology, at central wavelength, λ_0, only supports limited number of optical modes.

For some applications, multimode optical fiber is required whereas for long-haul communication, generally single mode optical fiber is desired. In order to get the better understanding of the modes in optical waveguide, the Fourier domain is an easy way to perform the calculations as the $\frac{\partial}{\partial t}$ is replaced by ω. Therefore, by taking the Fourier transform of equation (2.3) and considering only the linear part of E (i.e. $P_{NL} = 0$), the wave equation is given as:

$$\nabla^2 \tilde{\mathbf{E}}(\boldsymbol{r}, \omega) + \frac{n^2(\omega)\omega^2}{c^2} \tilde{\mathbf{E}}(\boldsymbol{r}, \omega) = 0. \qquad (2.8)$$

A solution of equation (2.8) is the superposition of plane wave, therefore, a linearly polarized solution when the light is confined in the transverse direction can be written as:

$$\tilde{\mathbf{E}}(\boldsymbol{r}, \omega - \omega_0) = F(x, y).A(z, \omega - \omega_0).e^{-i(\beta_0 z - \omega_0 t)}, \qquad (2.9)$$

where, A is the slowly varying amplitude (square of the magnitude of A, i.e. $|A|^2$ is known as the optical power of the signal), ω_0 is the central frequency, β_0 is the wave number at the central frequency, and F is the transverse field amplitude. A couple of conditional equations for the product of transverse and longitudinal parts of the wave equation can be written as:

$$\left(\frac{\partial^2}{\partial x^2} + \frac{\partial^2}{\partial y^2}\right) F(x, y) + \varepsilon(\omega) k_0^2 \, \mathrm{F}(x, y) = \tilde{\beta}^2 \mathrm{F}(x, y) \qquad (2.10)$$

$$2i\beta_0 \frac{\partial}{\partial z} A(z, \omega) + (\tilde{\beta}^2 - \beta_0^2) A(z, \omega) = 0. \qquad (2.11)$$

where, $\varepsilon(\omega)$ is the di-electric constant, $k = \frac{2\pi}{\lambda}$, $\tilde{\beta}$ is the wave number. Equation (2.11) can be used as a base to form a NLSE, discussed in later this section. For most of the application, single mode condition is preferred. The number of mode of any waveguide at some specific wavelength depends on its dimensions. For silicon based devices, the

dimensions are width and height of the waveguide. To have a single mode operation for silicon photonics, the width and height of the silicon waveguide is considered as 500 nm and 220 nm respectively [45]. The further explanation of how to achieve a single mode operation using silicon photonics technology is discussed in Chapter 4.

For optical fiber, the number of modes depends on the dimensions are the core radius (a) and the difference between the index of refraction of cladding and core of the optical fiber. The normalized frequency by which one can determine the number of mode is given as [47]:

$$V = k_0 . a . NA \tag{2.12}$$

where, $k_0 = \frac{\omega_0}{c}$, c is the speed of light, $NA = \sqrt{n_1^2 - n_2^2}$, n_1' is the refractive index of core and n_2' is the refractive index of cladding. For single mode operation, V<2.405 [48].

Figure 2.1 shows the silicon waveguide with lower and upper cladding as silicon oxide or oxide (SiO_2) calculated using Lumerical Mode Solution [49]. The width and height of the silicon waveguide for single mode operation is considered as 500 nm and 200 nm respectively [45]. Figure 2.1(b) shows the mesh of the silicon waveguide with upper and lower cladding of SiO_2. Figure 2.1(c) shows the mode of the transverse electric (TE) mode of silicon waveguide.

When the effect of nonlinearity is considered, the dielectric constant is modified as:

$$\varepsilon(\omega) = 1 + \tilde{\chi}^{(1)}(\omega) + \varepsilon_{NL} \tag{2.13}$$

where, ε_{NL} is the nonlinear part and given by $\varepsilon_{NL} = \frac{3}{4}\chi^{(3)}|E(\boldsymbol{r}, t)|^2$. The dielectric constant can be approximated as:

$$\varepsilon = (n + \Delta n)^2 \approx n^2 + 2n\Delta n \qquad (2.14)$$

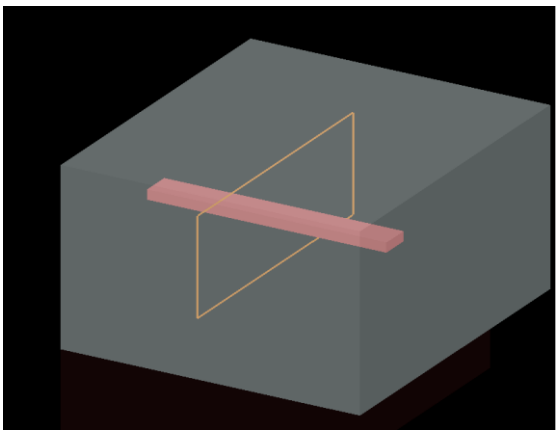

(a)

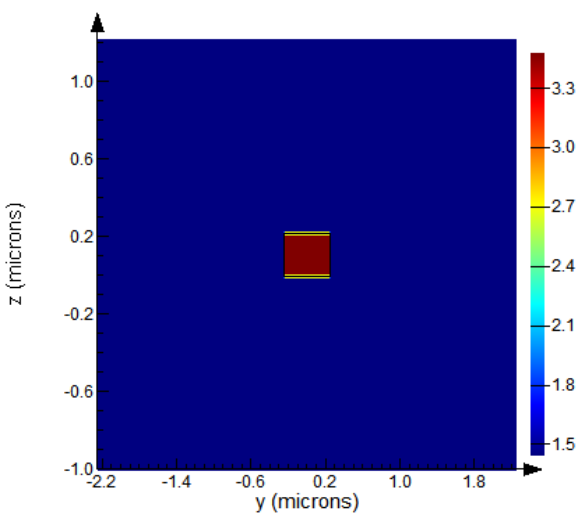

(b)

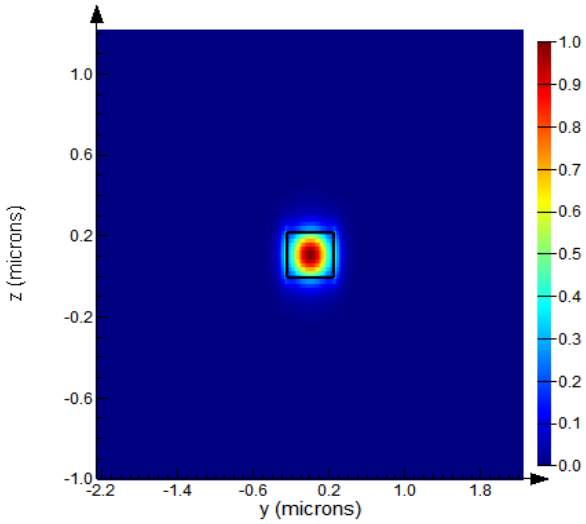

(c)

Figure 2.1: *shows the calculation of mode of silicon on insulator waveguide with dimension of 500x220 nm^2 using Lumerical mode solution. (a) simulation region of silicon waveguide. (b) mesh of silicon waveguide and (c) the mode in the silicon waveguide.*

The term

$$\Delta n = n_2|E|^2 + \frac{i\alpha}{2k_0}, \qquad (2.15)$$

is the small perturbation, n_2 is the nonlinear refractive index (discussed later in this section), α is the linear absorption coefficient, Δn can be neglected due to its very small value hence the dielectric constant is equal to the square of the refractive index, i.e. $\varepsilon = n^2$. The wave number parameter when considering the Δn for the single mode fiber is given as:

$$\tilde{\beta}(\omega) = \beta(\omega) + \Delta\beta \tag{2.16}$$

where,

$$\Delta\beta = \frac{k_0 \int\int_{-\infty}^{\infty} \Delta n |F(x,y)|^2 dxdy}{\int\int_{-\infty}^{\infty} |F(x,y)|^2 dxdy} \tag{2.17}$$

$\beta(\omega)$ can be expanded using Taylor series at the central frequency of ω_0 as:

$$\beta(\omega) = \beta_0 + (\omega - \omega_0)\beta_1 + \frac{1}{2!}(\omega - \omega_0)^2\beta_2 + \frac{1}{3!}(\omega - \omega_0)^3\beta_3 + \cdots, \tag{2.18}$$

where, $\beta_j = \left(\frac{\partial^j \beta}{d\omega^j}\right)_{\omega=\omega_0}$ $j = 1,2, ...$, where β_1 (rad/m) is inverse group velocity, β_2 (ps^2/km) is the group velocity dispersion, β_3 (ps^3/km) is the third order dispersion and so forth. As the spectral width is significantly smaller than central frequency, cubic and higher terms becomes negligible and can be neglected.

By substituting equation (2.18) in equation (2.11), with using an approximation relation as $\tilde{\beta}^2 - \beta_0^2 \sim 2\beta_0(\tilde{\beta} - \beta_0)$, and taking an inverse Fourier transform in order to convert the signal back in time domain, the time-dependent slowly varying amplitude is given as:

$$\frac{\partial A}{\partial z} + \beta_1 \frac{\partial A}{\partial t} + \frac{i\beta_2}{2}\frac{\partial^2 A}{\partial t^2} - \frac{\beta_3}{6}\frac{\partial^3 A}{\partial t^3} = i\Delta\beta A. \tag{2.19}$$

The term $\Delta\beta$ can be solved using equations (2.15) and (2.17), and substituting the updated value in equation (2.19):

$$\frac{\partial A}{\partial z} + \beta_1 \frac{\partial A}{\partial t} + \frac{i\beta_2}{2}\frac{\partial^2 A}{\partial t^2} - \frac{\beta_3}{6}\frac{\partial^3 A}{\partial t^3} = \frac{in_2\omega_0}{cA_{eff}}|A|^2 A - \frac{\alpha}{2}A. \quad (2.20)$$

The first term on the right side of equation (2.20) is known as the nonlinear part and can be written in form of nonlinear parameter (γ) in $(Wkm)^{-1}$ as:

$$\gamma = \frac{n_2\omega_0}{cA_{eff}} \quad (2.21)$$

where, A_{eff} (μm^2) is the effective area of the core and is given by:

$$A_{eff} = \frac{\left(\int\int_{-\infty}^{\infty}|F(x,y)|^2 dxdy\right)^2}{\int\int_{-\infty}^{\infty}|F(x,y)|^4 dxdy} \quad (2.22)$$

Equation (2.20) is known as the general NLSE for single mode optical fiber considering the dispersion and nonlinear, both effects. These both effects are discussed individually in the next sections of this chapter. The NLSE for silicon photonic technology is discussed in Chapter 4.

2.3.2 Dispersion

Dispersion is related to the broadening of the optical pulse inside the optical waveguide [50]. Optical signals at different wavelength propagate at different velocity as the refractive index of the material depends on the wavelength, and the speed of the optical signal depends on the refractive index of the material. When multiple signals travel inside the same optical fiber, they broader at different rate and all the signals are degraded due to broadening at different rate, usually observed in multimode optical fiber. This phenomenon is known as dispersion. The dispersion in multimode optical fiber severely degrades the signal as compared to the single mode. That's the reason, the single mode optical fiber is preferable for the long distance communication[51].

Optical pulses in single mode optical fiber also experience dispersion due to material properties. Material dispersion is related to the signal's wavelength dependency on the medium's refractive index. Consider a scenario, shown in Figure 2.2, in which a data stream of "01011" is propagated inside the optical fiber and output is recorded at different distances. Due to dispersion, each bit will experience the broadening. After some distance, a point comes when bits start to overlap each other; this phenomenon is known as the inter-symbol interference (ISI). This overlapping causes the severe degradation hence at the receiver side, it will be very hard to distinguish both signals. Therefore, the original signal will be impossible to recover with high accuracy [51]. Hence to avoid the effects of ISI, one must install the repeater at particular distance.

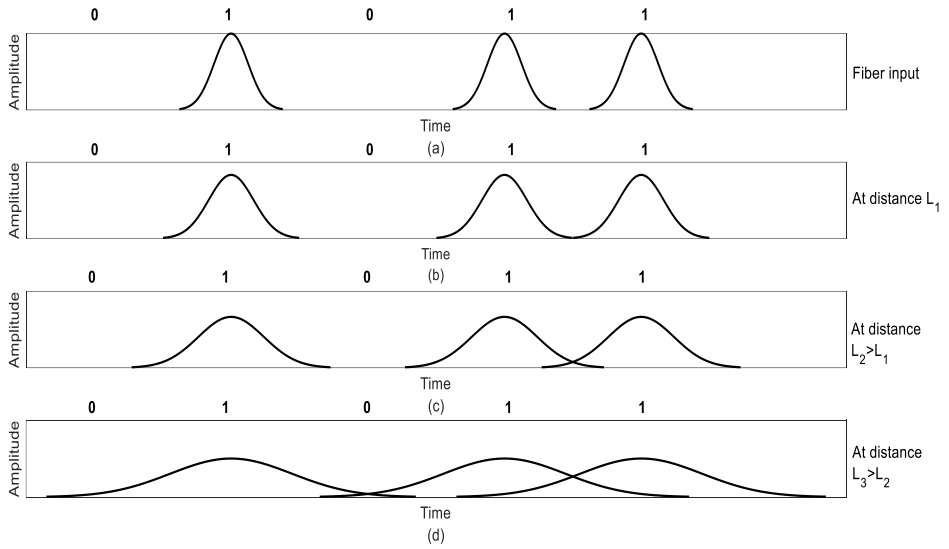

Figure 2.2: *Data stream of '01011' has been simulated at the different lengths. (a) at the input of the fiber. (b) at the distance L_1, (c) at the distance L_2, where $L_2>L_1$, and (d) at distance L_3, where $L_3>L_2$.*

Equation (2.18) is the main equation for the dispersion. At some particular group velocity, v_g, where a frame of reference moves with the pulse, the following transformation has been assumed;

$$T = t - \frac{z}{v_g} \equiv t - \beta_1 z \tag{2.23}$$

Substituting equation (2.23) in equation (2.20) and assuming that the pulse width $T_0 > 10\ ps$ and the third order dispersion parameter is also small for such long pulses. For simplicity we are considering the normalized amplitude of the signal (i.e. $\alpha = 0$) hence the equation (2.20) will be:

$$\frac{\partial A}{\partial z} = i\gamma|A|^2 A - \frac{i\beta_2}{2}\frac{\partial^2 A}{\partial T^2}. \tag{2.24}$$

This is known as the NLSE for optical fiber. The equation (2.24) will be used for the optical fiber. The two terms on the right side of equation (2.24) reflects the effect of nonlinearity and dispersion, respectively. It is very important to determine the minimum length at which the effect of nonlinearity and dispersion are critical. For this the nonlinear length (L_{nl}) and the dispersion length (L_d) is defined as [52]:

$$L_d = \frac{T_0^2}{|\beta_2|} \tag{2.25}$$

$$L_{nl} = \frac{1}{\gamma P_{peak}}, \tag{2.26}$$

where T_0 is the pulse width of the laser, P_{peak} is the input peak power of the optical signal. In order to calculate the effect of dispersion only, we will assume that the length of the fiber (L) is $L_{nl} >> L >> L_d$, hence the effect of nonlinearity is negligible, i.e. $\gamma = 0$. By considering this assumption, equation (2.24) can be written as:

$$\frac{\partial A}{\partial z} + \frac{i\beta_2}{2}\frac{\partial^2 A}{\partial T^2} = 0 \tag{2.27}$$

Taking the Fourier transform of equation (2.27), it can be rewritten as:

$$\tilde{A}(z,\omega) = \tilde{A}(0,\omega)\exp(\frac{i\beta_2\omega^2 z}{2}) \quad (2.28)$$

It can be analyzed from equation (2.28) that β_2 changes the phase of each spectral component whereas the spectrum of the pulse is unaltered. By taking the inverse Fourier transform of equation (2.28), the signal in time domain given by:

$$A(z,T) = \frac{1}{2\pi}\int_{-\infty}^{\infty}\tilde{A}(0,\omega)\exp(\frac{i\beta_2\omega^2 z - i2\omega T}{2})d\omega \quad (2.29)$$

By considering Gaussian pulse, $A(0,T) = \exp(-\frac{T^2}{2T_0^2})$, equation (2.29) is modified as:

$$A(z,T) = \left(1-\frac{iz}{L_d}\right)^{-\frac{1}{2}}\exp\left(-\frac{T^2}{2T_0^2}\frac{1}{\left(1-\frac{iz}{L_d}\right)}\right) \quad (2.30)$$

From equation (2.30), it can be analyzed that $z = L_d$, the pulse gets broader by a factor of $\sqrt{2}$ but the shape of the pulse is still remains Gaussian. It can also be noted that the input pulse was unchirped but with the group velocity dispersion, the pulse gets chirped. The time dependent phase shift (θ) of the signal is given as:

$$\theta(z,T) = -\frac{\mathrm{sgn}(\beta_2)\left(\frac{z}{L_D}\right)}{1+\left(\frac{z}{L_D}\right)^2}\frac{T}{T_0^2} \quad (2.31)$$

The difference in frequency, $\Delta\omega$, (also known as chirp) can be calculated by using the phase shift (θ) of equation (2.30), and can be written as:

$$\Delta\omega = -\frac{\partial\theta}{dT} = \frac{2\beta_2 L_d z}{(L_d^2+z^2)}\frac{T}{T_0^2} \quad (2.32)$$

Equation (2.32) shows that the chirp depends on the sign of β_2. In order to observe the effect of dispersion (D), I have considered the following parameters of SMF-28 optical fiber as: central wavelength (λ_0) of 1550nm, pulse width (T_0) is 10ps, pulse shape is Gaussian, length of the fiber (L) is 2 km, dispersion (D) is 18 ps/nm/km

[53], input average power (P_{av}) of 1 mW. The effect of dispersion is shown in Figure 2.3.

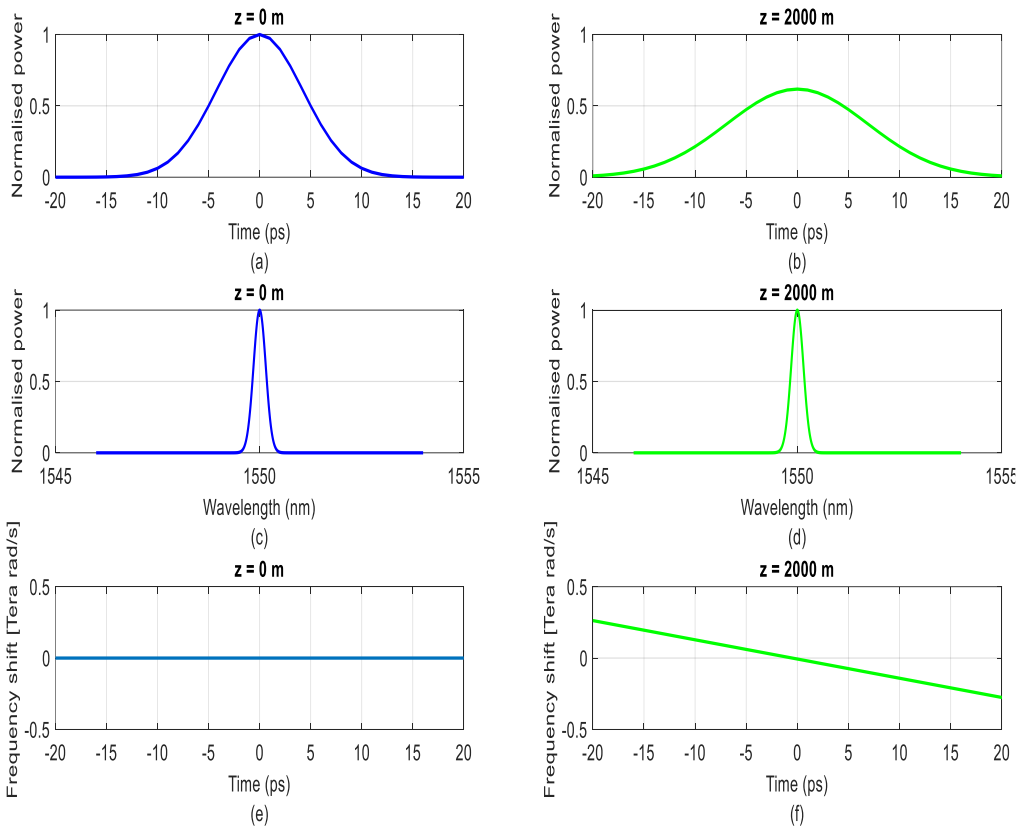

Figure 2.3: *Effect of dispersion experienced by an optical pulse in SMF-28 optical fiber. (a) Optical pulse in time domain at distance z = 0, (b) Optical pulse in time domain at distance z = 2 km, (c) Optical pulse in frequency domain at distance z = 0, (d) Optical pulse in frequency domain at distance z = 2 km, (e) Frequency shift (chirp) due to dispersion at distance z = 0, (f) chirp due to dispersion at z = 2 km.*

The relationship between β_2 and D is given as: $D(\lambda) = -\frac{2\pi c}{\lambda^2}\beta_2(\lambda)$ It can be observed that with distance, the pulse gets broader in time domain whereas the spectrum of the pulse is unaltered, which means that the effect of dispersion doesn't change the spectrum, only broader the pulse in time domain. The effect of dispersion changes the chirp of the signal and as it can be observed from Figure 2.3 that the input

pulse is unchirped but due to the dispersion effect, the pulse is chirped (linear). Since the dispersion, *D*, is positive (β_2 is negative) hence this chirp is known as linearly down-chirped.

2.3.3 Self-Phase Modulation

In this section, the effect of nonlinearity will be considered only. The term self-phase means that the phase of the signal depends on the power of the signal itself. It means that the phase of the signal will be modulated when the properties of the medium (i.e. refractive index of optical waveguides) are changed by the intensity of the signal itself, such phenomenon is known as the SPM effect [54]. The SPM effect can be used also for mitigating the chirp introduced by dispersion. In this section, the effect of nonlinearity in the optical fiber is investigated. Therefore, the length of the fiber (L) is $L_d >> L >> L_{nl}$, hence the effect of dispersion is negligible, i.e. $\beta_2 = 0$. Using this value in equation (2.24), it can be modified as:

$$\frac{\partial A}{\partial z} = i\gamma|A|^2 A \tag{2.33}$$

The solution of equation (2.33) can be written as:

$$A(z,T) = A(0,T)\exp(i\gamma|A|^2 z) \tag{2.34}$$

where, $A(0,T)$ is the field amplitude at $z = 0$. The nonlinear phase shift in SPM is given by:

$$\emptyset_{NL\_SPM}(L,T) = |A(0,T)|^2 \left(\frac{L_{eff}}{L_{NL}}\right) \tag{2.35}$$

where $L_{eff} = \frac{1-\exp(-\alpha L)}{\alpha}$ [54], is the effective length of an optical fiber and $L_{NL} = \frac{1}{\gamma P_0}$, is the nonlinear length with P_0 is the input peak power of the optical signal and γ is

the nonlinear coefficient. It can be observed from equation (2.34) that the nonlinearity in the optical fiber does not change the shape of the pulse in time domain, it only modifies the phase of the signal. Since the phase shift changes with respect to the peak power therefore, the phase shift is maximum at $T = 0$. Since the normalized amplitude is assumed in the calculations, hence $|A(0,0)| = 1$. Therefore, the maximum phase shift is given as:

$$\emptyset_{NL\_SPM(max)} = \frac{L_{eff}}{L_{NL}} = \gamma P_0 L_{eff} \qquad (2.36)$$

Figure 2.4 shows the simulated nonlinear effects, with the parameters of optical fiber (SMF–28) I have considered as: central wavelength (λ_0) of 1550nm, pulse width (T_0) is 10ps, with 10 GHz of repetition rate, pulse shape is unchirped Gaussian pulse, length of the fiber (L) is 2 km, nonlinear coefficient (γ) is 1.1×10^{-3} $W^{-1}m^{-1}$) [55], input average power (P_{av}) of 300 mW. It can be observed the shape of the pulse in time domain is not changed but the spectrum of the signal is changed. Hence we can say that the effect of SPM only changes the pulse spectrum (broaden) whereas the signal is same in the time domain. The nonlinear phase shift of 3.5π can be observed in Figure 2.4(d) due to the SPM effect. Figure 2.4(e) and Figure 2.4(f) shows that the nonlinear effect also introduces the chirp in the pulse, like GVD. But in the GVD, the chirp of the pulse was linear where as in SPM, the chirp is linear at the center of the pulse but near wings, the chirp is nonlinear. Hence, by appropriately choosing the sign of the GVD, the chirp introduced by the dispersion can be cancelled with the linear chirp introduced by the SPM. It will cause the signal to neither vary in time domain nor in frequency domain, a phenomenon known as a soliton. With the help of solitons, the optical signal can propagate in the optical fiber for thousands of kilometers without

degrading and has successfully been used for data transmission in the telecommunication network [56], [57].

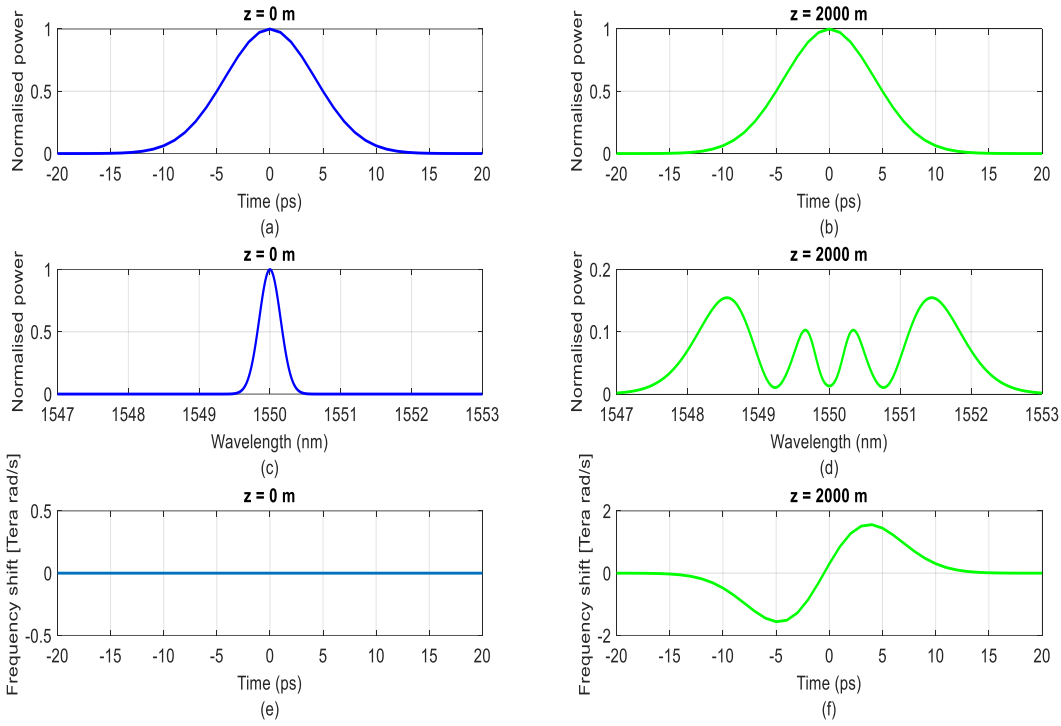

Figure 2.4: *Effect of self phase modulation experienced by an optical pulse in SMF-28 optical fiber. (a) Optical pulse in time domain at distance z = 0, (b) Optical pulse in time domain at distance z = 2 km, (c) Optical pulse in frequency domain at distance z = 0, (d) Optical pulse in frequency domain at distance z = 2 km, (e) Frequency shift (chirp) due to SPM at distance z = 0, and (f) chirp due to SPM at z = 2 km.*

2.3.4 Cross Phase Modulation

The major difference between the XPM and SPM is that in SPM only one high power signal is transmitted in a nonlinear medium and the phase of the signal is proportional to the power of itself whereas in XPM [58], two signals are coupled (usually one signal is high power and other is low power) in the same highly nonlinear

medium. The high power signal (known as 'pump') changes the phase of itself (due to SPM effect) and also changes the phase shift of the low power signal (known as 'probe'). The phenomenon by which the phase change of probe signal varies due is pump signal is known as XPM. By introducing another signal, the overall sensitivity (phase shift) is doubled than SPM [41]. Therefore, by using the same strategy as used in SPM, i.e. $L_d >> L >> L_{nl}$, thus $\beta_2 = 0$; the equation (2.24) for XPM can be modified as:

$$\frac{\partial A_a}{\partial z} = i\gamma|A_a + 2A_b|^2 A_a \tag{2.37}$$

$$\frac{\partial A_b}{\partial z} = i\gamma|A_b + 2A_a|^2 A_b \tag{2.38}$$

where, the subscript *a* and *b* shows the pump and probe signal respectively. It can be analyzed from equation (2.37) and (2.38) that by introducing another signal, the sensitivity gets double and this is true for the nonlinear phase shift. The nonlinear phase shift in XPM is almost double that of the nonlinear phase shift in SPM; and given as:

$$\emptyset_{NL\_XPM(max)} = 2\gamma P_0 L_{eff} \tag{2.39}$$

We will use the effect of SPM and XPM to extract the pulse width information in Chapter 3.

2.4 Split Step Method

Since equation (2.24) has the simultaneous effects of nonlinearity and dispersion, hence both parts can be solved analytically using the split step method [41]. Equation (2.24) can be written in this way:

$$\frac{\partial A}{\partial z} = \left(\widehat{D} + N\right)A, \tag{2.40}$$

Where $\widehat{D}$ is a differential operator and *N* is a nonlinear operator. The $\widehat{D}$ operator includes the dispersion and the linear losses whereas, the *N* operator includes the nonlinearities effect on the input optical pulsed signal. The higher order dispersion and nonlinearity has not been considered for the split step method. The operators are given by:

$$\widehat{D} = -\frac{i\beta_2}{2}\frac{\partial^2}{\partial T^2} - \frac{\alpha}{2} \tag{2.41}$$

$$N = i\gamma(|A|^2) \tag{2.42}$$

In the fiber medium, the nonlinearity and the dispersion both act together along the fiber but in the split step method, the author [41] has approximated the solution by splitting the main equation in to two parts, dispersion and nonlinear, and solve each equation for a small distance (*h*). Hence, the propagation of a pulse from *z* to *z* + *h* is carried out in two steps.

In the first step, the nonlinear component is absent, i.e. *N* = 0, and only dispersion is considered and in the second step, the nonlinear component is considered and dispersion is absent, i.e. $\widehat{D}$ = 0. Mathematically,

$$A(z+h,T) \approx \exp\left(h\widehat{D}\right)\exp(hN)\,A(z,T). \tag{2.43}$$

Where, the operator $exp(h\widehat{D})$ can be evaluated in the Fourier domain as:

$$\exp(hD)\,B(z,T) = F_T^{-1}\exp[h\widehat{D}(i\omega)]F_T B(z,T) \tag{2.44}$$

Where, F_T is the Fourier transform and $(F_T)^{-1}$ is the inverse Fourier transform

The exact solution of equation (2.40) is given as:

$$A(z+h,T) = \exp[h\left(\widehat{D}+N\right)]\,A(z,T). \tag{2.45}$$

If the propagation distance, *z*, is divided in very large values such that the spacing between the two points (*h*) is very small, the accuracy can be improved. The equation (2.43) can be written as follow:

$$A(z+h,T) \approx \exp\left(\frac{h}{2}\widehat{D}\right)\exp\left(\int_{z}^{z+h} N(z')dz'\right)\exp\left(\frac{h}{2}\widehat{D}\right)A(z,T). \quad (2.46)$$

Figure 2.5 shows the graphical illustration of the split step method.

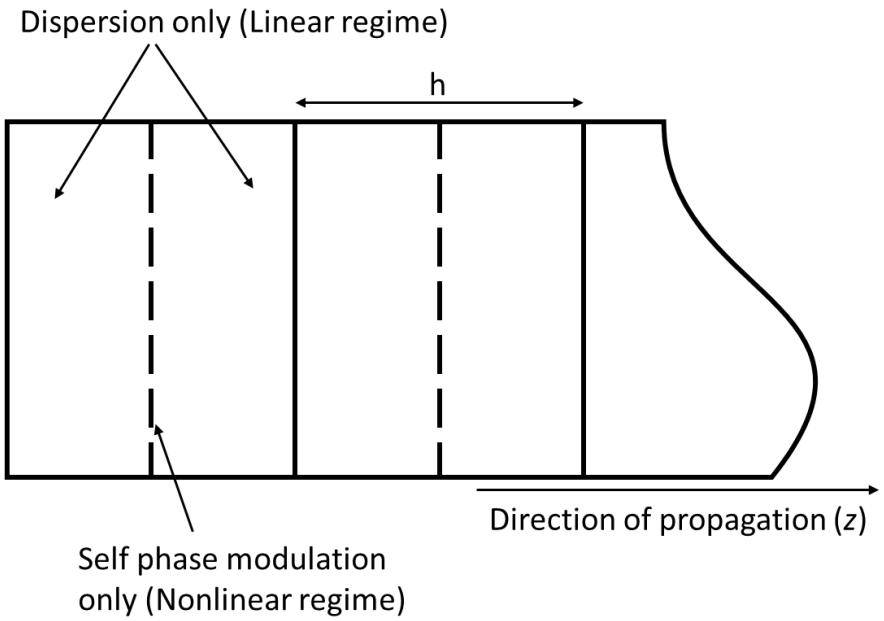

Figure 2.5: *Graphical illustration of the split step method*

The split step method is applicable to both fiber optic and optical waveguides.

Chapter 3

Picosecond Pulse Width Measurement Using Nonlinear Loop Mirror and Power Meter

This chapter introduces novel way of measuring the pico-second optical pulse width using an optical power meter and a highly nonlinear optical fiber. The working principles and required components are listed in this chapter. Commonly used measurement techniques which extract/characterize the optical pulse width are also listed in this chapter. The most common techniques are frequency resolve optical gating (FROG) and spectral phase interferometry for direct electric-field

reconstruction of ultra-short optical pulses (SPIDER). The experimental results of the proposed method are verified by the theoretically simulating the NLSE for XPM and SPM using split step method. Section 3.1 listed the literature in which the commonly used techniques are mentioned to extract/characterize the pulsewidth and amplitude information. Section 3.2 explains the proposed pulse width measurement technique using nonlinear optical loop mirror and power meter. Simulated results are also discussed in this section. Section 3.3 explains the experimental setup of this techniques for both SPM and XPM. Section 3.4 discusses the main experimental results obtained from this method. The results are verified by simulating the NLSEs. Whereas section 3.5 is about the device limitation which explains the working range of this device. Finally, section 3.6 explains the summary of this chapter.

3.1 Introduction

The efficient generation of ultra-short laser pulses in the picosecond regime has enabled a wide range of applications from optical communications [59] to the measurement of ultra-fast physical processes [60]. In order to measure the characteristics of picosecond optical fields, a number of techniques have been developed including FROG [61]–[63], SPIDER [64], [65] and sonogram [66], [67]. Since the ultra-short pulse has a very short duration than the temporal resolution of the measuring devices like optical oscilloscope or digital communication analyzer (DCA), optical spectrum analyzer (OSA) and so forth, therefore, by using such techniques, one can characterize the pulse up to sub-picosecond level [62].

Some modified versions of FROG have also been reported using XPM and four wave mixing (FWM) for the full characterization of an optical pulse [68], [69]. In addition to these non-linear methods, there are a number of linear self-referencing methods, for example, phase reconstruction using optical ultrafast differentiation (PROUD), that avoid the requirement of high pump powers and provide a complete pulse characterization [70]–[72]. These methods allow for the full amplitude and phase reconstruction of the pulse. Compact methodologies based on on-chip technologies have also been demonstrated making use of highly non-linear optical waveguide technology [73], [74]. In general, ultra-short pulse measurement techniques either require high pulse energies or expensive measurement equipment such as optical spectrometers in order to operate.

All optical performance monitoring is crucial for achieving stable optical networks, in particular with regards to the effects of dispersion. There are several parameters that can alter the dispersion of an optical link, i.e. temperature, path reconfiguration or physical maintenance around the fiber site [75]. Also, in some applications, for example in optical networks or in cases where well-behaved (non-distorted) optical pulses are used as a temporal probe, it is often enough to monitor the temporal envelope of the pulse to allow compensation of any dispersion that may be induced between the laser source and the monitor point. High-speed photodetectors and sampling oscilloscopes, intensity auto-correlators or cross-correlators can be used in laboratory environments for this purpose.

In this chapter, an alternative method is presented which uses a fiber amplifier, NOLM [76] and optical power meters. Since the system is implemented in an all-fiber configuration, with no moving parts or complex measurement equipment, it can be

implemented as a simple system bolt-on, or in remote locations with the potential for distributed arrays of monitors across networks. Unlike optical sampling oscilloscopes and optical auto-correlators, this method does not monitor the shape of the optical pulses. Only the temporal width are monitored by using this method; hence, it can also be used to monitor the residual dispersion of the optical link [75].

Design of the method was carried out using simulations of the NLSEs using well-defined split step method [41]. From simulations we found that this method is compatible with well-behaved pulses with slowly varying envelopes such as $sech^2$ or Gaussian. The measurement range is related to the non-linear phase shift introduced by the measured signal (its peak power can be boosted by using an erbium-doped fiber amplifier (EDFA) up to its saturated output power) and to the length of the non-linear medium and its non-linear coefficient. In this work, pulse widths up to 10 ps are measured, with a resolution of 0.25 ps, assuming a $sech^2$ or Gaussian pulse envelope with slowly varying phase internal structure. The measurement range can be extended to cover 0.25 to 40 ps by careful selection of the physical parameters in the setup.

3.2 Picosecond Pulse Width Measurement Using a Non-linear Optical Loop Mirror

As noted in the section 3.1, the method presented here relies on the assumption that the optical picosecond pulses under investigation are of a simple form with typically a $sech^2$ or Gaussian shape and little internal phase structuring. The purpose of this method is to provide a means to monitor pulse width variation induced, for example by dispersion between the pulse origin and monitor point. We present two

variations of the measurement technique, both based on a $\chi^{(3)}$ optical non-linearity process in a NOLM (see Figure 3.1). In both approaches optical pulses are coupled to the NOLM and the resulting average power at its output ports is measured using a slow optical power meters. The ratio $\frac{P_{out_1}}{P_{out_2}}$ of the measured average output powers is a function of the optical switching induced by either self-phase or cross-phase modulation depends on the peak power of a laser pulse injected into the NOLM. For well-behaved pulses, the peak power is simply related to average power through the envelope shape and pulse train duty cycle. In order to over-sample the measurement, the input pulses are incrementally amplified by an EDFA to produce a series of power splitting ratios as a function of the measured average power of the input pulse train.

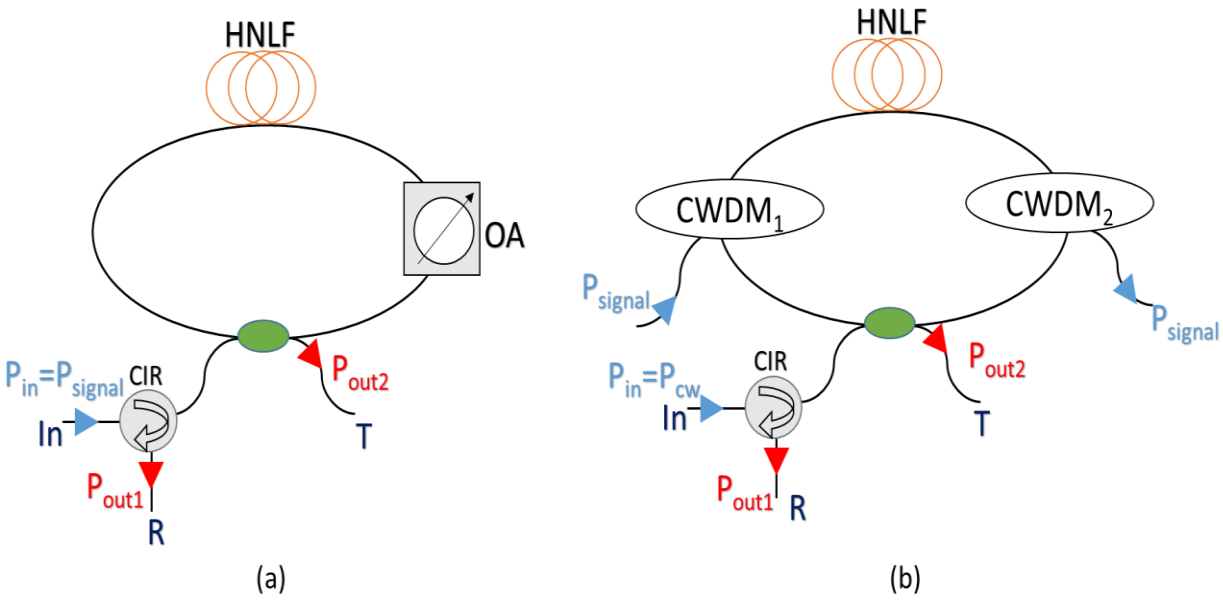

Figure 3.1: *Non-linear optical loop mirror (a) in self phase modulation configuration; (b) in cross phase modulation configuration using CWDM couplers for injecting and filtering out the pulsed signal. Where OA – optical attenuator, CWDM – course wavelength division multiplexing/de-multiplexer, CIR – optical circulator, and HNLF – highly non-linear fiber*

The system behavior can be modelled by the NLSE, numerically solved using a split-step method [41] as explained in section 2.4. Input values to this numerical method were chosen to match parameter values of highly nonlinear fiber (HNLF), which was used in the experiment, and are summarized in Table 3.1.

The repetition rate of the pulse source was taken as 10 GHz, matching the erbium doped fiber mode-locked laser source used in the experiments. In this chapter we use a non-linear fiber length of 100 m and an EDFA with a saturated power level of 17 dBm and therefore simulations are carried out to demonstrate the performance of the system under these constraints. However, the achievable pulse width measurement range of the method can be tuned by varying the setup components, discussed in more detail in section 3.5.

Table 3.1: *Simulation Parameters of HNLF for solving the NLSE using split step method for pulse width measurement.*

Parameter	**Value**	**Unit**
Length (L_{HNLF})	100	m
Gamma (γ)	10.8	$(W\ km)^{-1}$
Dispersion (D)	0.11	ps/nm/km
Dispersion slope (S)	0.016	$ps/nm^2/km$
Absorption coefficient (α)	0.9	dB/km
Splice Loss (HNLF to SMF28)	0.2	dB
Signal wavelength (λ_1)	1550	nm
Probe wavelength(λ_2)	1530	nm

3.2.1 Simulations for Self-phase modulation:

Figure 3.1(a) shows the SPM variant of the scheme. In this case, the amplified pulse train (P_{signal}) is coupled in to one port of the NOLM, where the coupler ratio is unbalanced (80:20) in order to create asymmetry in the counter-propagating modes. An additional optical attenuator (10 dB) is added to the loop to give control of this imbalance. The higher power replica of the pulse undergoes SPM in the HNLF creating a phase shift between the replicas as they recombine at the output coupler.

The proportion of the total power coupled to each port is dependent on the relative phase between the two pulse replicas, and their relative powers:

$$P_{out} = \begin{pmatrix} P_{out_1} \\ P_{out_2} \end{pmatrix} = \begin{pmatrix} n_x \\ n_y \end{pmatrix} P_{in} \tag{3.1}$$

where,

$$n_x = e^{\phi_L}\sqrt{p(1-p)}(1 + e^{j\theta_{NL}})e^{j\frac{\pi}{2}} \tag{3.2}$$

$$n_y = e^{\phi_L}(pe^{j\theta_{NL}} - (1-p)) \tag{3.3}$$

ϕ_L includes the linear phase shift and linear loss and can be computed as $\phi_L = j\beta L_{HNLF} - \alpha L_{HNLF}$, β is the propagation constant of the field in the optical fiber, α is the linear absorption loss, p is the splitting ratio of the input coupler, and L_{HNLF} is the length of the HNLF. θ_{NL} is the non-linear phase shift and is proportional to the input power. The equations (3.2) and (3.3) are modified from [77] due to the inclusion of a coarse wavelength division multiplexer (CWDM) coupler to inject the amplified pulse train into the loop mirror. The non-linear phase shift can be computed by numerically solving the NLSEs discussed in chapter 2. The higher orders of dispersion

are considered as negligible, thus, the NLSE for SPM is listed as equation (3.4) and the NLSEs for XPM are listed as equations (3.5) and (3.6). These NLSE are solved using the split step method where the non-linear phase shift induced by XPM is approximately twice that accumulated through SPM [41].

$$\frac{\partial A}{\partial z} + \frac{i\beta_2}{2}\frac{\partial^2 A}{\partial T^2} = i\gamma|A|^2 A - \frac{\alpha}{2}A \tag{3.4}$$

$$\frac{\partial A_a}{\partial z} + \frac{i\beta_{2a}}{2}\frac{\partial^2 A_a}{\partial T^2} = i(\gamma|A_a|^2 + 2\gamma|A_b|^2)A_a - \frac{\alpha}{2}A_a \tag{3.5}$$

$$\frac{\partial A_b}{\partial z} + \frac{i\beta_{2b}}{2}\frac{\partial^2 A_b}{\partial T^2} = i(\gamma|A_b|^2 + 2\gamma|A_a|^2)A_b - \frac{\alpha}{2}A_b \tag{3.6}$$

Where, the subscript 'a' shows the high power signal parameters and 'b' shows the low power continuous wave probe signal. $A_{(a,b)}$ is the slowly varying amplitude of the pulse envelope, $\beta_{2(a,b)}$ is the group velocity dispersion, $\gamma_{(a,b)}$ is the non-linear coefficient, $\lambda_{(a,b)}$ is the operating wavelength and α is the linear loss of the waveguide. The values of all the above parameters are summarized in Table 3.1. The splice loss and absorption has already included in the experimental results; hence both are not included in the simulations.

The effect of counter propagating non-linear interactions in the NOLM can be significant when using high repetition rate signals [78], hence the total effective non-linear phase shift using SPM and XPM, by taking the counter clockwise non-linear phase shift into account, can be calculated using equation (3.7);

$$\Delta\theta_{eff} = \theta_{cw\_NL} - \theta_{ccw\_NL} \tag{3.7}$$

Where $\Delta\theta_{eff}$ is the total effective phase shift, θ_{cw_NL} is the non-linear phase shift produced in the clockwise direction and θ_{ccw_NL} is the non-linear phase shift produced in counter-clockwise direction due to XPM. Figure 3.2 (a) and Figure 3.2 (b) shows

the normalized reflected power (P_{out_2}) at the reflected port (*R*) and transmitted power (P_{out_2}) at transmitted port (*T*) of NOLM plotted as a function of the input average power (P_{in}), with the pulse width as a parameter. An optical circulator (CIR) is used for separating the input and output reflected power of the NOLM. A $sech^2$ pulse envelope is assumed in this case. The output powers follow sinusoidal variations as a function of the input average power for a given input pulse width, with maximum and minimum values defined by the asymmetric coupling fraction of the input/output coupler. The input average power inducing a $\pi/2$ phase-shift results switching of power between *R* and *T* ports of the NOLM and subsequently can be used to extract the pulse width from measurements of the power splitting between *R* and *T* ports as a function of P_{in}, as shown in Figure 3.2 (c).

The relationship between pulse widths and $\pi/2$ switching point can be adequately fitted to a second order polynomial. It is also apparent that to achieve this switching, average powers in the range of 10's of mW are required for few picosecond pulses. This limits the useful range of this method to pulses of ~5 ps with our EDFA having a saturated power of ~50 mW (17 dBm).

3.2.2 Simulations for Cross-phase modulation:

With a minor modification of the setup in Figure 3.1(a), the sensitivity of the SPM scheme can be significantly enhanced. Figure 3.1(b) shows a setup that includes a secondary CW laser source as a probe of the loop non-linearity in a XPM scheme. In this case, the probe signal is coupled in to one input port of NOLM and the pulse train is added to travel the NOLM only in one direction using a CWDM. The probe

signal experiences strong XPM in one of the counter propagating modes, inducing a relative phase shift between the modes at the output coupler. In order to avoid cross-talk at the detectors, the pulse train is coupled out of the loop, using a second CWDM, before reaching the output coupler.

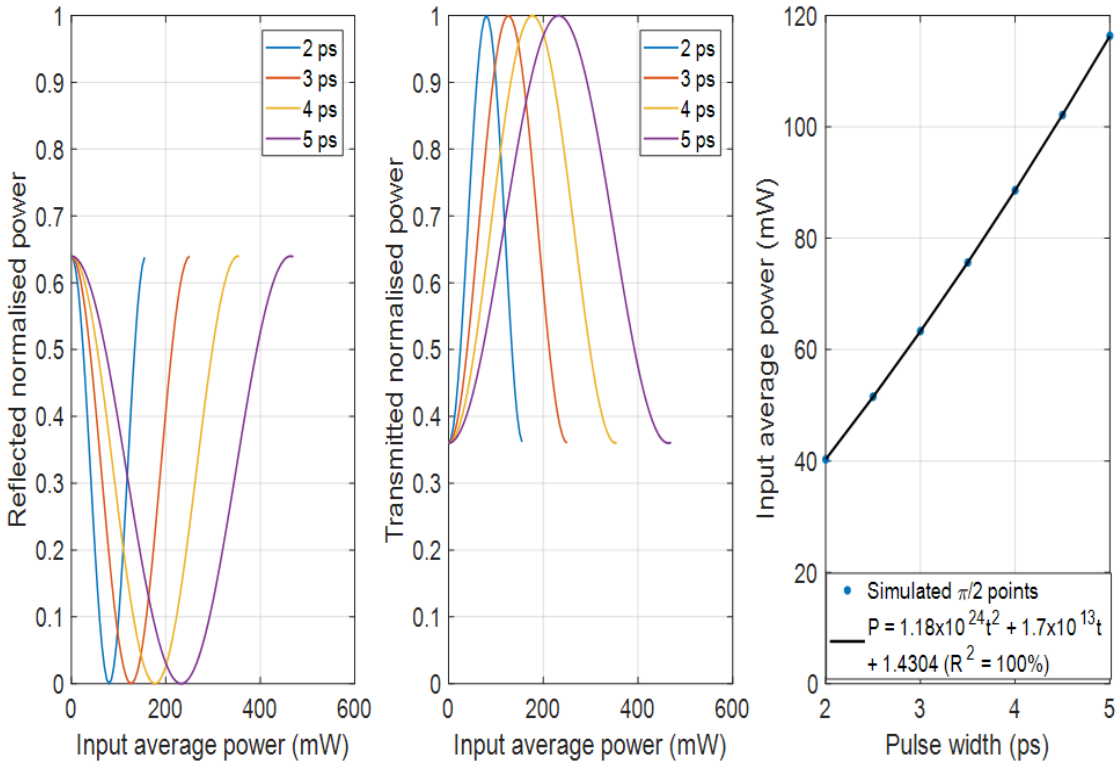

(a) (b) (c)

Figure 3.2: *Simulated NOLM output power at (a) reflected, (b) transmitted port as a function of input average power of the signal for different pulse widths using SPM. (c) The input average power at π/2 switching points as a function of pulse width*

The average output power at the port *T* and *R*, respectively can be calculated using equations (3.1), (3.2), and (3.3), where in this case the non-linear phase shift is directly proportional to the loop entering peak power (P_{signal}), with the signal pulse width as a parameter. As before, the reduced relative phase shift between clockwise and counter-clockwise signals is taken into account using equation (3.7). Figure 3.3

(a) and Figure 3.3 (b) show the normalized transmitted and reflected output powers of the probe as a function of input average power of the pulse train for different pulse widths. As expected, the $\pi/2$ switching points are reached at half the power in the XPM case as compared to the SPM. Figure 3.3 (c) shows the quadratic fit of the $\pi/2$ points for the XPM setup.

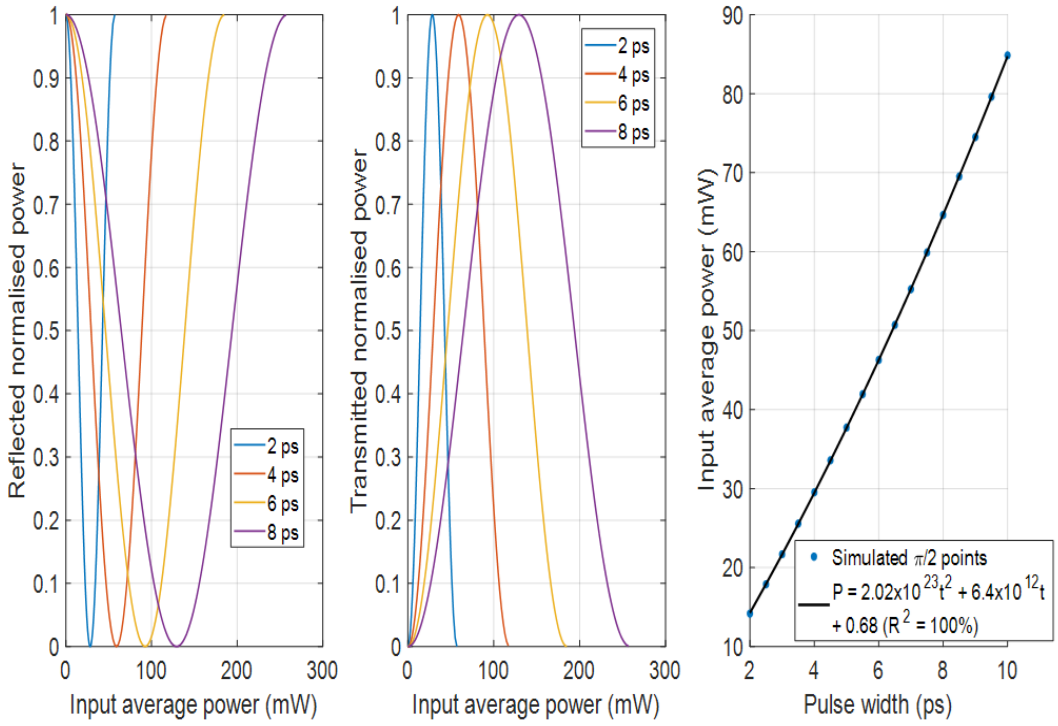

(a) (b) (c)

Figure 3.3: *Simulated NOLM output power at: (a) reflected, (b) transmitted port as a function of input average power of the signal for different pulse widths using XPM. (c) The input average power at π/2 points as a function of pulse width of the signal and their fitting*

3.2.3 Effect of Pulse Envelope Function:

The XPM simulations were then performed for a Gaussian pulse envelope, where the $\pi/2$ switching points as a function of the laser pulse width and are compared

with the previously obtained sech^2 case in Figure 3.4. There is not a noticeable difference between those two results, meaning that calibration of the experimental setup with either pulse shape would allow measurement of both envelope types with the same accuracy.

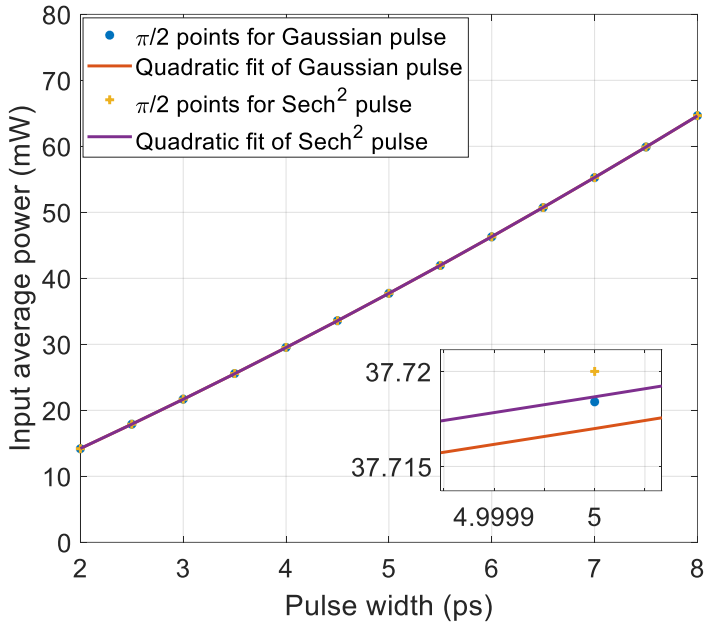

Figure 3.4: *Quadratic fitted π/2 points for both Gaussian and sech2 pulse shapes as a function of input pulse width*

3.3 Experimental Setup for Measurement of Pulse Width

Schematics of the experimental setups used for measurement of optical pulse widths using NOLM based on SPM and XPM are shown in Figure 3.5 (a) and Figure 3.5 (b), respectively. The PriTel, Inc. mode-locked fiber laser running at a 10 GHz repetition rate was used as a source of picosecond optical pulses, referred here as the signal. The central wavelength of the signal was 1550.7 nm with a spectral bandwidth of 1.4 nm. The signal was amplified using an EDFA limited to a saturated output power

of 50 mW (17 dBm). The input pulse width variation was achieved by using serially coupled lengths of SMF-28 patch cord cables (up until 500 m) to disperse the signal. For the XPM setup, a low power continuous wave (CW), referred to here as the probe, was generated using Agilent 81989A tunable laser at the wavelength of 1530 nm with a power of 5 mW. A 1% power tap was introduced before the NOLM for an input average power monitoring of the signal by a temperature stable Agilent 8153A Lightwave Multimeter. The probe was then injected into the NOLM via a 50:50 optical directional coupler and the signal via $CWDM_1$ coupler (see Figure 3.5(b)). The two polarization controllers (PC) used in the setup were set to maximize the power coupled to the reflected port in the linear regime. Once the state of PCs was set, it was not altered for any of the subsequent measurements. The passband of the $CWDM_1$ coupler is 1541 to 1559 nm. The signal after traveling HNLF of length (L_{HNLF}) was subsequently filtered out of the loop using $CWDM_2$ coupler with the passband of 1542 to 1558 nm. The transmitted and reflected average power of the probe were measured at *T* and *R* ports, respectively as indicated in Figure 3.5(b). The pulse width of the signal was measured using a FR-103XL optical auto-correlator before entering in to the NOLM.

3.4 Experimental Results

In this section, the experimental results for SPM and XPM are discussed.

3.4.1 NOLM based on self-phase modulation configuration

The experimental setup for optical pulse width measurements using the NOLM based on SPM is shown in Figure 3.5 (a). A varying length of SMF28 optical fiber was used to disperse nearly transform limited 2 ps FWHM laser pulses to 2.9 ps, 3.7 ps, and 4.5 ps, respectively.

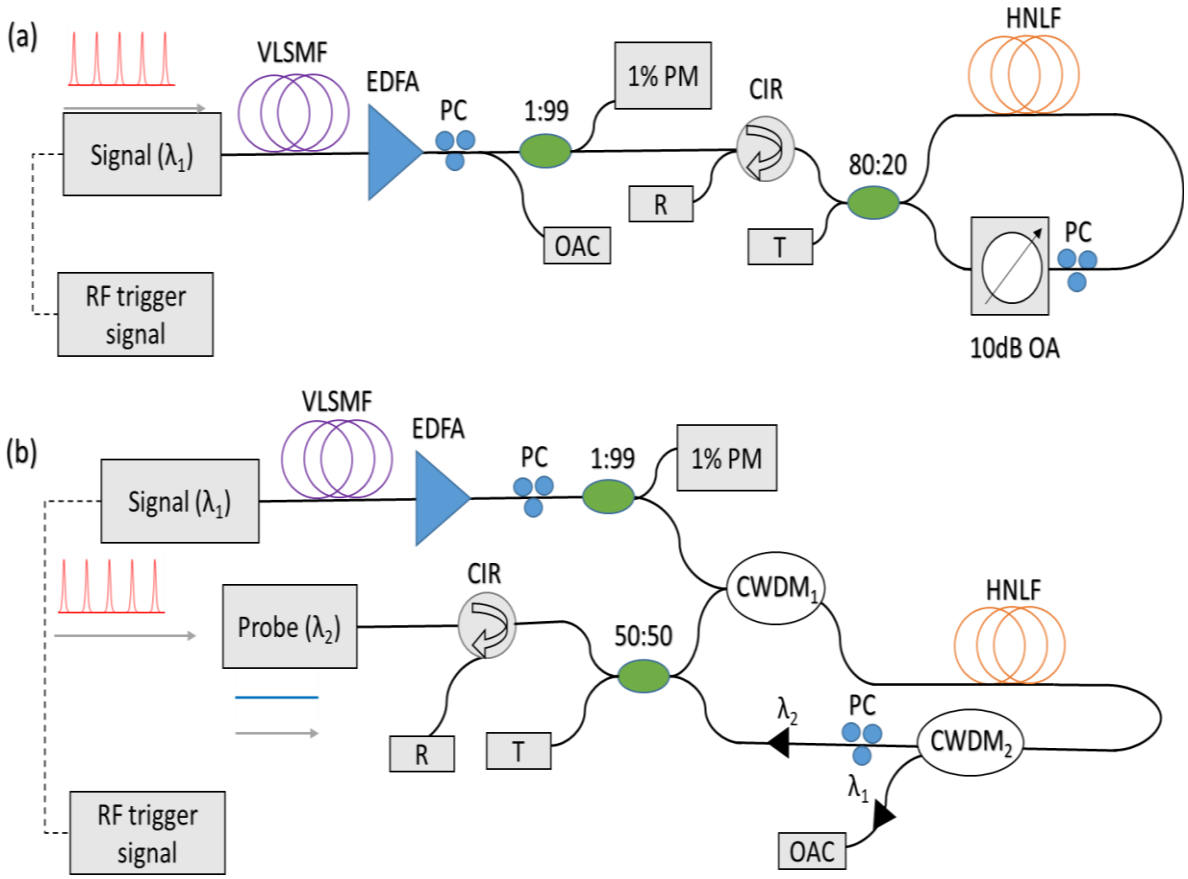

Figure 3.5: *Experimental setup for optical pulse width measurement using NOLM based on: (a) SPM and (b) XPM, respectively. Where, PM – power meter, CIR – optical circulator, OAC – optical auto-correlator, EDFA – erbium doped fiber amplifier, PC – polarization controller, CWDM – course wavelength division multiplexer/de-multiplexer, HNLF – highly non-linear fiber, OA – optical attenuator, VLSMF – variable length single mode fiber, R – reflected port, T – transmitted port*

Figure 3.6 shows the normalized optical power obtained from measurements at *R* and *T* ports as a function of the P_{in}, for the case of a 2 ps pulse. Since the simulated curves show sinusoidal dependence on the input average power, hence the measured transmitted and reflected data was fitted to equations (3.8) and (3.9), respectively, where *A*, *B*, *C*, and *D* are free parameters. This fitting then allows extraction of the $\pi/2$ point.

$$POTX = A.\sin(B.Pin + C) - D \tag{3.8}$$

$$PORX = 1 - POTX \tag{3.9}$$

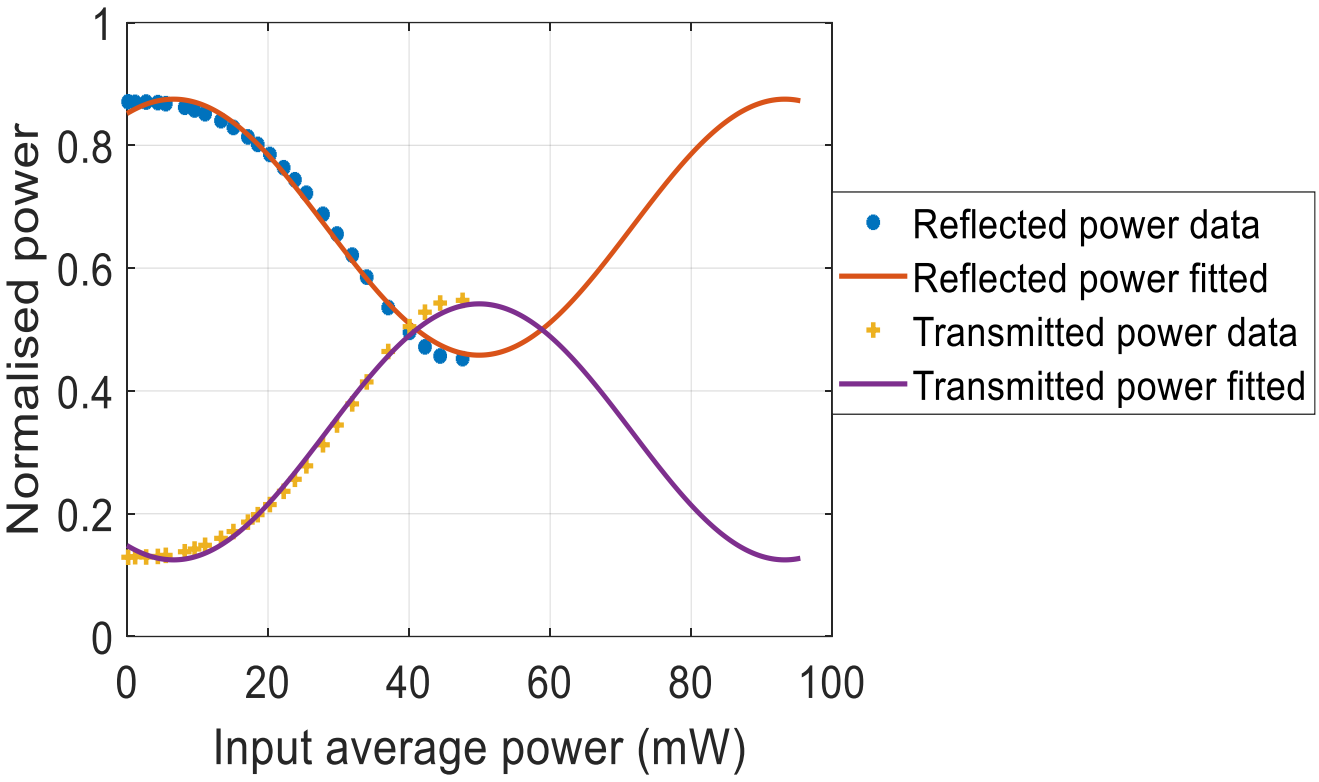

Figure 3.6: *The normalized reflected and transmitted NOLM output power based on SPM measurements showing a sinusoidal fit using (3.8) and (3.9) to extract the π/2 point*

The experimentally measured and fitted transmission and reflection powers of the NOLM obtained for up to a 50 mW of the input average optical power are shown in Figure 3.7 (a) and Figure 3.7 (b), respectively. A 10 dB optical attenuator is used in the counter clockwise direction in order to suppress the power of signal hence the signal power in the 20% arm is not enough to produce the non-linearity. For wider pulses, the $\pi/2$ points were not accessible experimentally due to limited available EDFA saturated power, hence the fitting curves based on equations (3.8) and (3.9) were used to obtain the $\pi/2$ points. Figure 3.7 (c) shows the input average power at $\pi/2$ points and the quadratic fitting. The measured curves show good agreement with the simulations and a clear dependence on the input pulse width.

3.4.2 NOLM based on cross phase modulation configuration

The experimental setup for optical pulse width measurements using the NOLM based on XPM configuration is shown in Figure 3.5 (b). Similarly, as before, five different pulse widths were generated from the initial 2 ps FWHM pulses. Again, the measured data were fitted to a sinusoidal function described by using equations (3.8) and (3.9). The 2ps pulse data were only fitted up to the $\pi/2$ point, as after this the switching exhibited some saturation.

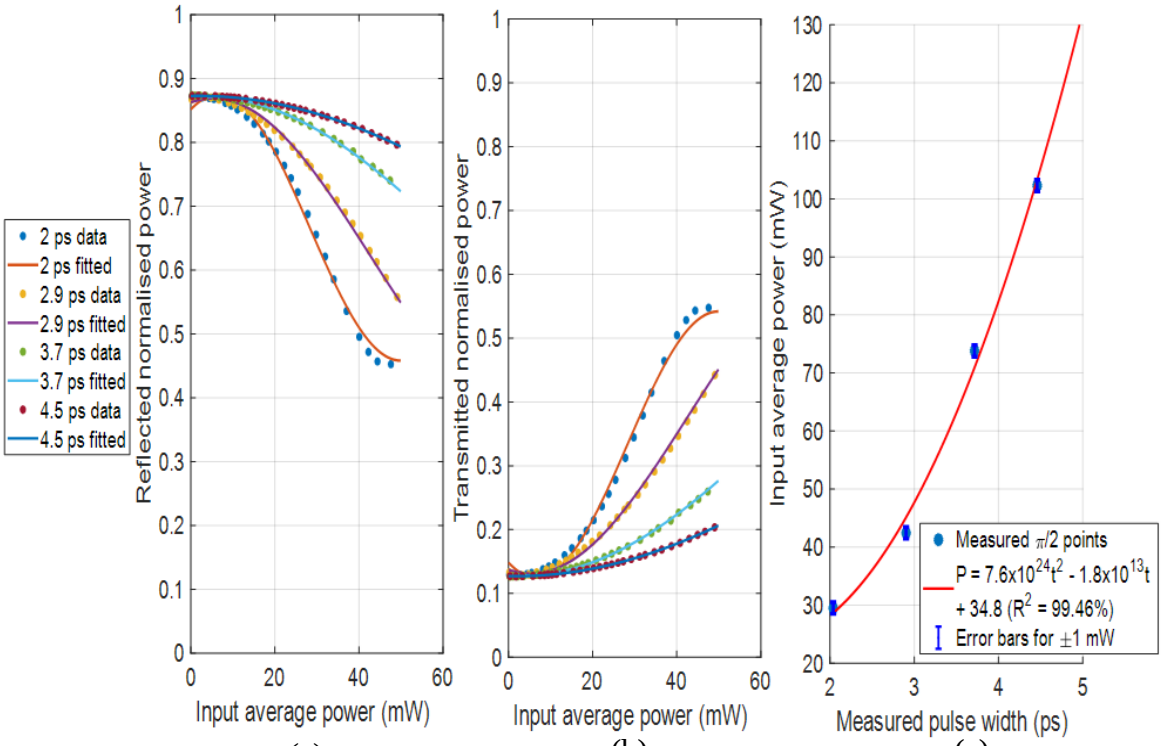

(a) (b) (c)

Figure 3.7: *Measured: (a) reflected, (b) transmitted output power of the NOLM in SPM configuration as a function of the input average power of the signal obtained for different pulse width values. (c) Input average power at π/2 points as a function of the signal pulse showing the quadratic fitting.*

The normalized transmission and reflection output powers of the XPM based NOLM are shown in Figure 3.8 (a) and Figure 3.8 (b), respectively. The input average power of the signal at $\pi/2$ points and the quadratic fitting is shown in Figure 3.8 (c). As predicted by the theory, the sensitivity of the XPM is doubled compared with the SPM case, thus allowing more efficient pulse width measurements. We measured the input average optical power of the signal with an accuracy of ± 1 mW, that together with the R^2 = 99.88% of the quadratic fit, gives a predicted pulse width resolution of ~ 0.25 ps.

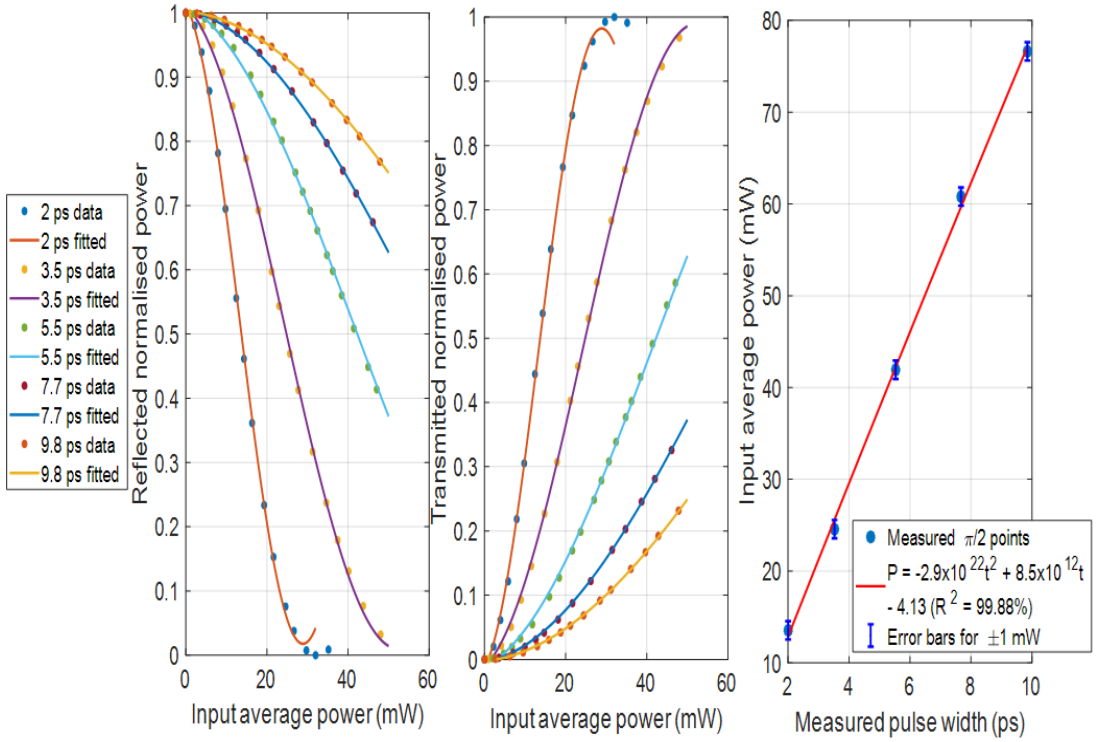

(a) (b) (c)

Figure 3.8: *Measured: (a) reflected, (b) transmitted output power of the NOLM on XPM configuration as a function of the input average power of the signal obtained for different pulse widths values. (c) Input average power at π/2 points as a function of the signal pulse showing quadratic fitting*

3.5 Discussion and Limitations of Device

In order to characterize the temporal width of an optical pulse, the setup described is required to define the $\pi/2$ switching point with respect to the average power of the signal. This therefore puts a limitation on the measurement range of the system that depends on the available saturation power of the EDFA and the length of non-linear fiber in the loop. As stated above, the accuracy of the measurement is limited by the accuracy of measuring the input average power from power meter and

the linearity of the fitted calibration curve. Assuming the dispersion length is higher than the non-linear length, the non-linear phase shift for XPM is given as:

$$\phi_{XPM} = \frac{2\gamma P_{av} T L_{eff}}{\tau} \tag{3.10}$$

where γ is the non-linear coefficient, P_{av} is the input average power, T is the laser repetition period, τ is the pulse width of the laser signal, and L_{eff} is the effective length of the HNLF fiber given as $L_{eff} = \frac{1-\exp(-\alpha L_{HNLF})}{\alpha}$ [41]. Considering equation (3.10), it is clear that the operation ranges for measuring an optical pulse width can be extended by maximizing any or all of listed parameters. By using XPM simulations the dynamic range of the measurement system was estimated for practically achievable lower and upper limits for the following parameters. HNLF lengths were considered with the lower limit as L_{HNLF} = 20 m and L_{HNLF} = 1 km as the upper limit. We also considered a maximum available EDFA saturated output power ~40 dBm. The results of these simulations are summarized in Figure 3.9.

From Figure 3.9(a) we can see that the minimum pulse width that could be measured with the hardware is 250 fs and can be achieved using L_{HNLF} = 50 m and 15 dBm EDFA. As mentioned above, the resolution of this method is 0.25 ps, hence by using this hardware, the minimum possible pulse width can be measured as 250 fs. However, the device range can be extended to measure optical pulse widths well beyond 10 ps FWHM. If using L_{HNLF} = 20 m and 38 dBm EDFA or L_{HNLF} = 1 km and 21 dBm EDFA the device can be used to measure an optical pulse within the region of 10 – 40 ps as shown in Figure 3.9(b) and Figure 3.9(c), respectively. For pulses longer than 40 ps, the accumulated non-linear phase on the counter-propagating signal is significant, limiting the measureable effective non-linear phase shift of the system,

highlighting the significant role of the repetition rate in this scheme. The device can be also easily reconfigured for pulse width measurements beyond a 40 ps range, by lowering the repetition rate, however for this regime, high speed electronics may be a more attractive option.

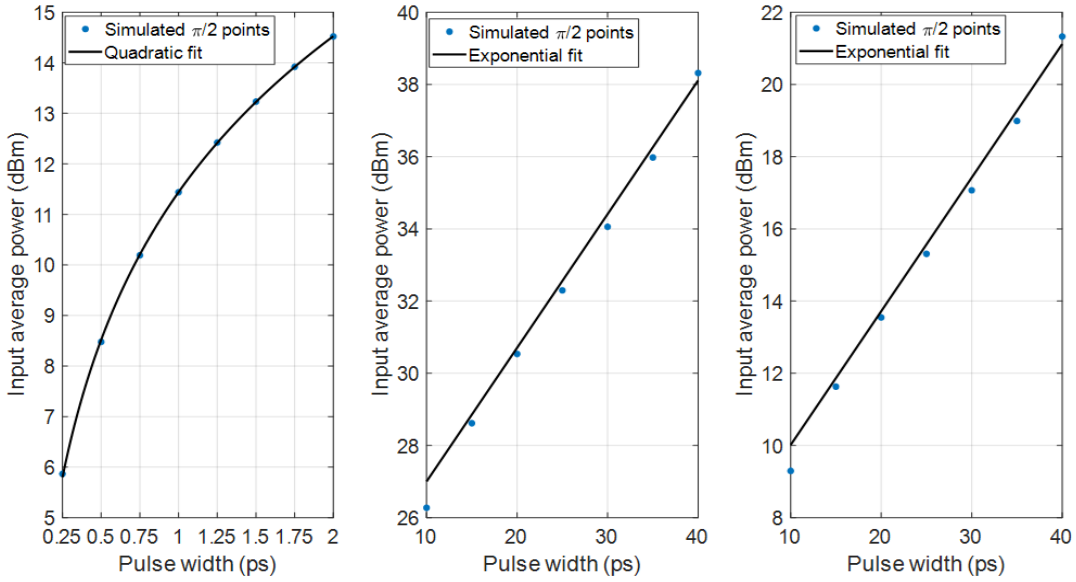

(a) (b) (c)

Figure 3.9: *Device parameters selection. (a) pulse width measurements below 2 ps: = 50m, EDFA saturated output 15 dBm; pulse width measurements below 100 ps: (b) = 20 m, EDFA saturated output 38 dBm or (c) = 1 km, EDFA saturated power 21 dBm*

3.6 Summary

We have presented an all-fiber non-linear interferometric method for determining optical pulse widths using measurements of average power using slow detectors. The approach is applicable where Gaussian or $sech^2$ pulse envelopes can be assumed and the internal phase structure is slowly varying (for example in dispersive communications links). Pulses in the range of 2–10ps were successfully characterized experimentally. The dynamic range of the proposed method is limited by available

hardware, with realistic limits of 250 fs to 40 ps. The method may find its use in distributed networks or as a bolt-on to optical systems using ultra-short pulse sources. This fiber device can be also implemented as an integrated non-linear Sagnac or Mach-Zehnder interferometer using integrated optical platforms, including SOI, where mode volumes can be small and non-linear coefficients can be very high, i.e. 307 $(Wm)^{-1}$, potentially leading to improvements in device miniaturization, stability and power [79].

Chapter 4

Silicon Photonics Technology

4.1 Introduction

There has been tremendous growth in the development of PIC. The reason is most of the requirement are based on micro-scale level (even starts from hundreds of nm). In the photonic integration, it is highly desirable to use a material which is compatible with the current electronic industry, i.e. CMOS, such that the photonic and

electronic circuits can run on the same chip and perform high speed signal processing functions. The photonic integrated circuits are currently used for many applications from quantum computing to medical sciences [80]–[84]. In this chapter, the common platforms are discussed which are compatible with CMOS and has high nonlinear coefficient for measuring the optical pulsewidth in pico-second regime. The brief overview of the SOI technology, its advantages and applications is discussed in Section 4.2 . The effective index and dispersion properties of the silicon on insulator waveguide are discussed in section 4.3 . Since this thesis is based on the nonlinear application so some of the integrated nonlinear devices which are used in the field of PIC for various nonlinear applications are discussed in section 4.4 which include directional coupler (DIC), microring resonator, Mach-Zehnder interferometer (MZI), and nonlinear optical loop mirror (NOLM). Finally, section 4.5 discusses the summary of this chapter.

4.2 Silicon on Insulator Technology

Silicon on insulator (SOI) is one of the highly used material in the field of the optoelectronics due to its inherent advantages. The most common advantages are:

1. This material can be used as a platform for both photonic integration circuits (PICs) and very large scale integration (VLSI).

2. It has very high nonlinear Kerr refractive index ($n_2 = 6\times10^{-18}$ m^2/W[85]), approximately 100 times stronger than silica and the Raman gain is 1000 times stronger than silica [86].

3. The CMOS technology can be scalable to offer low cost optical devices with the speed of gigabits per second speed with low loss [87].

4. Compatible with CMOS circuit fabrication to offer high speed operation at low power hence can produce number of PICs at low cost [88].

5. Silicon waveguide has strong optical guiding properties due to its high refractive index (n_{Si} = 3.47 at 1550 nm wavelength) as compared to air (n = 1) and glass cladding layer (n_{SiO_2} = 1.44) near infrared wavelength of 1550 nm [79].

6. Due to very strong optical confinement, SOI platform allows very compact device with band radii of few micrometers [45].

A typical cross section of strip waveguide based SOI wafer is shown in Figure 4.1 where the silicon waveguide is buried with upper and lower cladding layer of silica. Below the lower cladding silica, a layer of silicon is used as a substrate. The thickness of lower cladding and the silicon based substrate and crystalline silicon as per requirement of electronics industry for high performance circuits [45] is 2 µm and 725 µm, and 220 nm in 8-inch wafer.

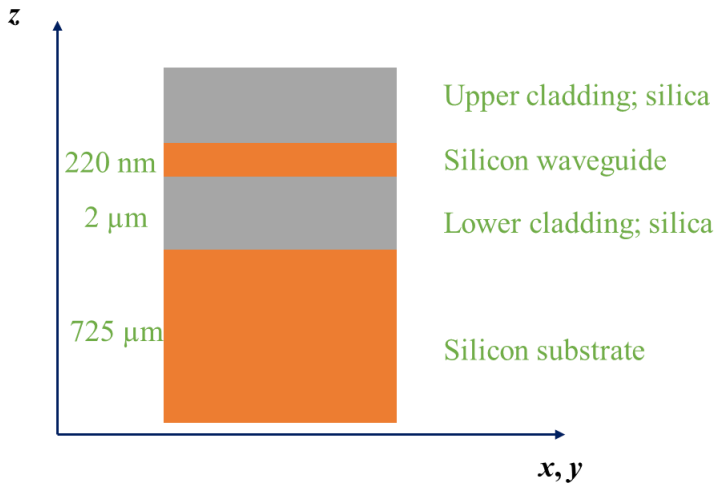

Figure 4.1: *Cross section of strip waveguide based SOI technology*

SOI platform can be used to design several passive as well as active devices. Some of the most common passive devices using SOI platform are: waveguide Bragg gratings [89], directional couplers [90], [91], Y-branches [92], [93], multimode interference (MMI) coupler [94], [95] and many others [96]–[100]. Modulator is one of the most common active devices in the field of PIC. The centrosymmetric structure of the silicon material prevents the electro-optic effects. This prevents the development of electro-optic or linear modulator using silicon material. The only way to achieve the modulation is to use the plasma dispersion effects [101] or by using a hybrid devices such as a device combining III-V and silicon material on insulator. Using the plasma dispersion effects, many researchers have designed modulators using SOI platform [102]–[105]. In this thesis, the main focus is based on passive SOI devices for nonlinear applications.

4.3 Effective Index and Dispersion Properties in SOI Waveguide

In this section, a method is described to calculate the effective refractive index and group refractive index using Lumerical mode solution [49]. The same devices have been simulated as shown in Figure 4.1. The 3-axis dimension of the SOI based waveguide is shown in Figure 4.2.

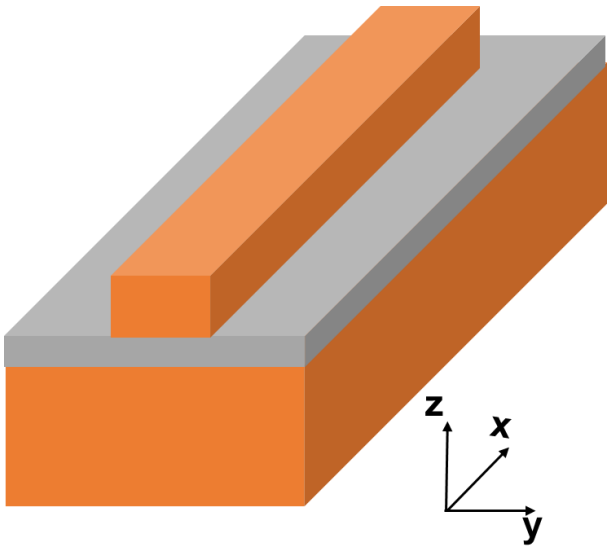

Figure 4.2: *A 3-axis strip waveguide dimension using silicon photonics platform.*

The width and height of the SOI waveguide is 500 nm and 220 nm, respectively. The effective index of silicon using TE mode using Lumerical mode solution is 2.445 at central wavelength of 1550 nm. The group index can be calculated using equation (4.1) [106].

$$n_g(\lambda) = n_{eff}(\lambda) - \lambda \frac{dn_{eff}}{d\lambda}, \tag{4.1}$$

where, n_{eff} is the effective index of the waveguide, λ is the central wavelength. The effective index of SOI waveguide with dimension of 500 nm × 220 nm from 1500 to 1600 nm is shown in Figure 4.3(a). Whereas, the group index is shown in Figure 4.3(b). The dispersion in the optical material is given as:

$$D(\lambda) = \frac{\lambda d^2 n(\lambda)}{c d\lambda^2} \tag{4.2}$$

Where, c is the speed of light in space. The dispersion parameter (D) is related to the β_2 in following relation as [107]:

$$D(\lambda) = -\frac{2\pi c}{\lambda^2}\beta_2(\lambda) \tag{4.3}$$

As mentioned in chapter 2, when $D < 0$ or $\beta_2 > 0$; the material has normal (positive) group velocity dispersion (GVD) and $D > 0$ or $\beta_2 < 0$; the material has anomalous (negative) GVD. The dispersion parameters calculated using equation (4.3); D and β_2 of SOI waveguide is shown in Figure 4.3(c) and Figure 4.3(d), respectively. It can be analyzed from Figure 4.3(c) and Figure 4.3(d) that the silicon has negative or anomalous GVD.

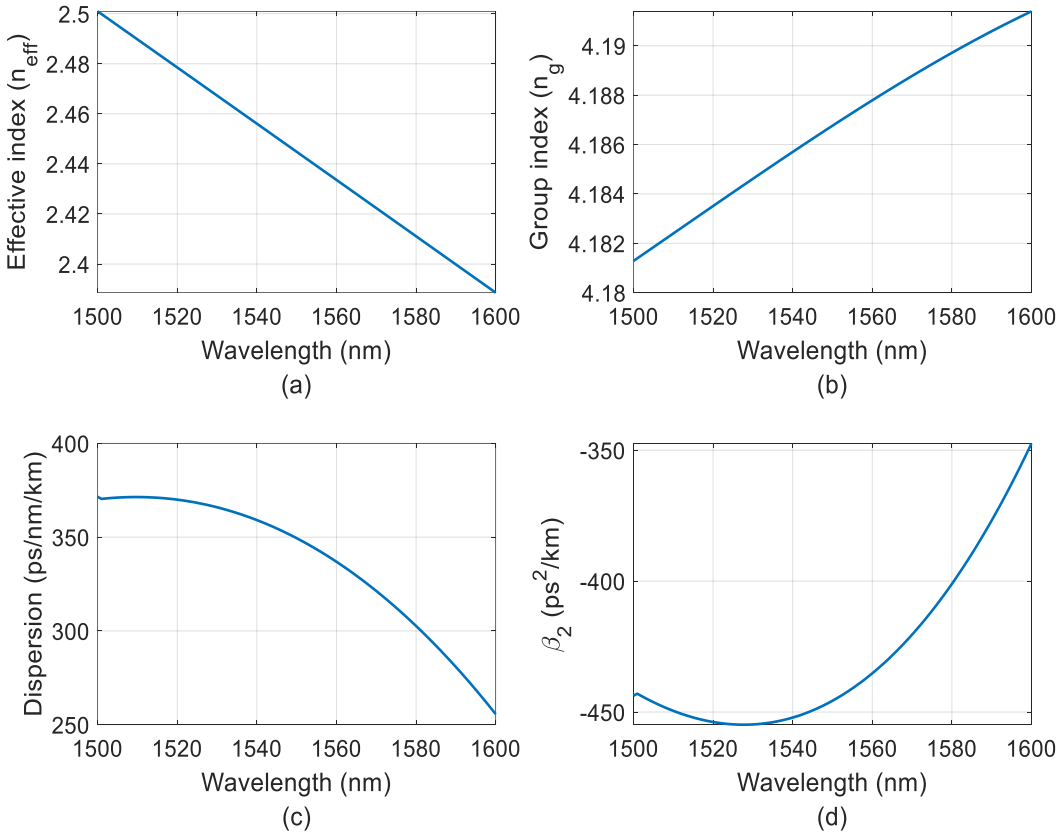

Figure 4.3: *Simulation of the strip SOI waveguide with dimension of 500 nm × 220 nm using Lumerical Mode solution. (a) Relationship between simulated effective refractive index and operating wavelength. (b) Relationship between simulated group refractive index and operating wavelength. (c) Dispersion (D) vs wavelength relation (d) Group velocity dispersion (β_2) with respect to the operating wavelength.*

4.4 Common Integrated SOI Based Devices for Nonlinear Application

In this section, the common passive devices used in SOI platform for nonlinear applications are discussed. This includes directional coupler, ring resonator, Mach-Zehnder interferometer (MZI) and nonlinear optical loop mirror (NOLM).

4.4.1 Directional Coupler

A waveguide directional coupler is a four port device which is used to split the power as per its splitting ratio. It has two inputs and two output ports and has many applications in fiber optics communication and SOI based devices [108]. The main function of DIC is to split the optical signal coherently and send it to the output ports. The 2×2 DIC is designing by using the two parallel waveguides, the splitting ratio (or coupling coefficient) depends on the length of the parallel waveguides (L_c) and the gap (g) between the waveguides.

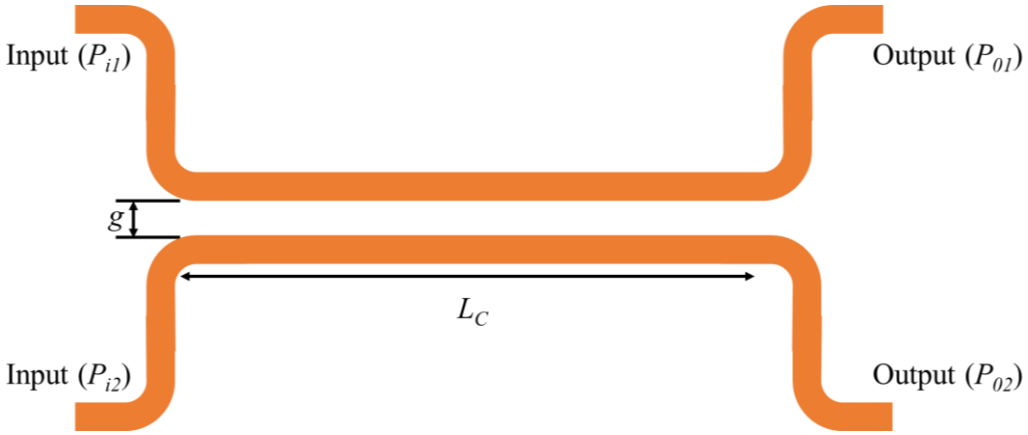

Figure 4.4: *A 2×2 waveguide directional coupler with coupling length as (L_c) and the gap between the two waveguides is g.*

A typical 2×2 DIC is shown in Figure 4.4 with input power inserted on port 1 (P_{i1}) and port 2 (P_{i2}). The output power splitting ratio depends on the *Lc* and *g*. If the coupler with splitting ratio of 90:10 is designed, hence on output port 1 (P_{o1}), 90% of P_{i1} and 10% of P_{i2} is transferred and vice versa is true for output port 2 (P_{o2}). Considering a simple approach by inputting the power at one port, i.e. $P_{i2} = 0$. Using the couple mode theory [108], the output power of a 2×2 directional coupler can be calculated using equations (4.4) and (4.5), i.e.,

$$P_{o1}(L) = P_{i1}cos^2(kL) \quad (4.4)$$

$$P_{o2}(L) = P_{i1}sin^2(kL) \quad (4.5),$$

where $P_{i1} \equiv |A_0|^2$, k is the coupling coefficient, L is the length of the waveguides. In order to calculate the super-mode, the Lumerical mode solution is used to calculate the effective index of both waveguides. Using the super-modes, the coupling coefficient, *k* can be calculated as:

$$k = \frac{\pi \Delta n}{\lambda} \quad (4.6)$$

where, Δn is the effective index difference, i.e. $n_1' - n_2'$. The difference between the refractive index and the effective index is following: refractive index is related to the properties of the material whereas, the effective index is related to the properties of the mode. Since two separate modes are propagating in the waveguides, therefore, in order to calculate the cross over length, the propagation constant of the modes propagating in the waveguides are used. The cross over length is the length at which the power is completely transferred from 1st (through) waveguide in to the 2nd (cross) waveguide. The propagation constants (β_1 and β_2) of the two modes with effective indices, n_1' and n_2', respectively, is given as:

$$\beta_1 = \frac{2\pi n_1}{\lambda} \tag{4.7}$$

$$\beta_2 = \frac{2\pi n_2}{\lambda} \tag{4.8}$$

The cross-over length (L_x) is a length at which the both modes are having π phase-shift apart from each other. Hence the L_x can be calculated as [45]:

$$L_x = \frac{\lambda}{2\Delta n} \tag{4.9}$$

The output of the directional coupler, consisting of two parallel strip waveguides based on SOI platform, is simulated using parameters shown in Table 4.1. The output power (P_{o1} and P_{o2}), calculated using equation (4.4) and (4.5), as a function of length of the waveguides (L) is shown in Figure 4.5.

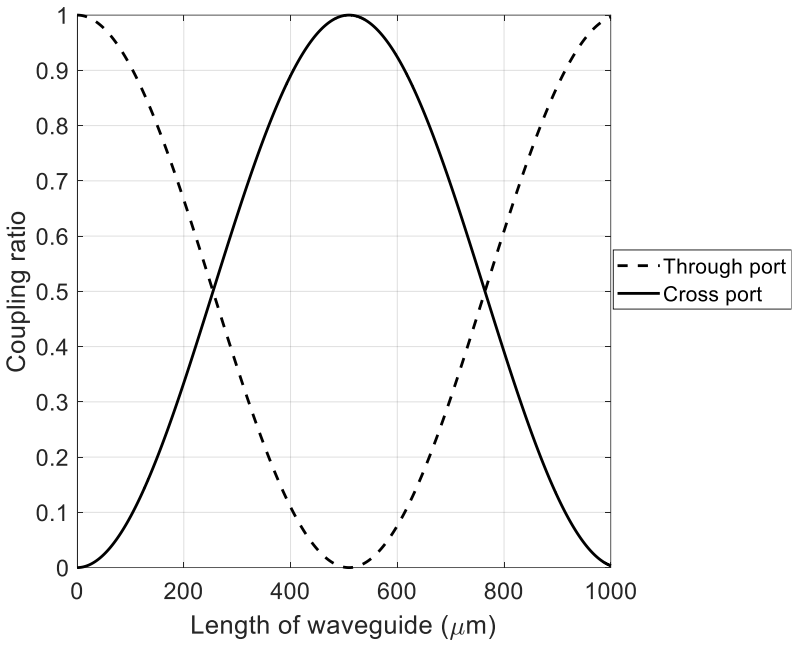

Figure 4.5: *Simulated output of a directional coupler calculated using equations (4.4) and (4.5).*

The cross over length for this coupler, which is calculated using equation (4.9), is 510 μm. This can be verified from Figure 4.5 as well. DIC can be used as a nonlinear

device for optical switching in optical fiber [109] and waveguides[110]–[112]. An optical Y-branch is similar to DIC as it also splits/combine the power. The only difference is; with directional coupler, one can design a coupler with any coupling ratio like 50:50, 60:40, 70:30 and so forth but with Y-branch, the optical power is divided equally among its two output ports, hence works as 50:50 beam-splitter[45].

Table 4.1: *Parameters used the direction coupler using Lumerical mode solution*

S. No.	Parameter	symbol	Value	Unit
1.	Gap	g	500	nm
2.	Width	W	500	nm
3.	Height	h	220	nm
4.	Effective index of waveguide 1 (even mode)	n_1'	2.445457	-
5.	Effective index of waveguide 2 (odd mode)	n_2'	2.443936	-
6.	Input power	P_{i1}	0	dBm
7.	Operating wavelength	λ	1550	nm

4.4.2 Micro-Ring Resonator

A micro ring resonator, can be simply written as ring resonator, is a passive device which consists of a ring coupled with either one or two straight waveguide. Due to coupling of ring with straight waveguide(s), the power is looped back on itself, therefore the multiple resonances are produces and the wavelength spacing between the two resonances is known as the free spectral range (FSR) of the ring resonator [113]. The FSR of the ring resonator depends on the diameter of the ring. Due to the small bending loss of silicon, a ring resonator can be designed as small as 1.5 um radius [114], that's why it is known as micro-ring resonator. A typical ring resonator coupled with single straight waveguide, also known as all pass filter or notch filter and can be seen in Figure 4.6(a). A ring resonator coupled with two straight waveguides is also known as add-drop ring resonator and is shown in Figure 4.6(b). The through output of the all pass filter is given as:

$$E_{thr} = E_{in}\, e^{i(\pi+\theta)} \left(\frac{a-te^{-i\theta}}{1-tae^{i\theta}}\right) \tag{4.10}$$

where, E_{thr} is the output of the ring resonator coupled with single straight waveguide, E_{in} is the input electric field, $\theta = \beta L$ is the phase shift of the ring resonator with β as the propagation constant and L as the round trip length of the ring, $a^2 = e(-\alpha L)$ is the single pass amplitude transmission with α as power attenuation coefficient (usually in cm^{-1}) and t is the self-coupling coefficient and k is the cross coupling coefficient such that $|t|^2 + |k|^2 = 1$. The transmission intensity of all pass filter is computed using equation (4.11)

$$T_{APF} = \left|\frac{E_{thr}}{E_{in}}\right|^2 = \left(\frac{a^2-2atcos\theta+t^2}{1-2atcos\theta+(ta)^2}\right) \tag{4.11},$$

where, T_{APF} is the transmission of all pass filter ring resonator. The transmission intensity of the add–drop ring resonator is given as:

$$T_t = \left|\frac{E_{thr}}{E_{in}}\right|^2 = \left(\frac{t_2^2 a^2 - 2t_1 t_2 a cos\theta + t_1^2}{1 - 2at_1 t_2 cos\theta + (t_1 t_2 a)^2}\right) \quad (4.12)$$

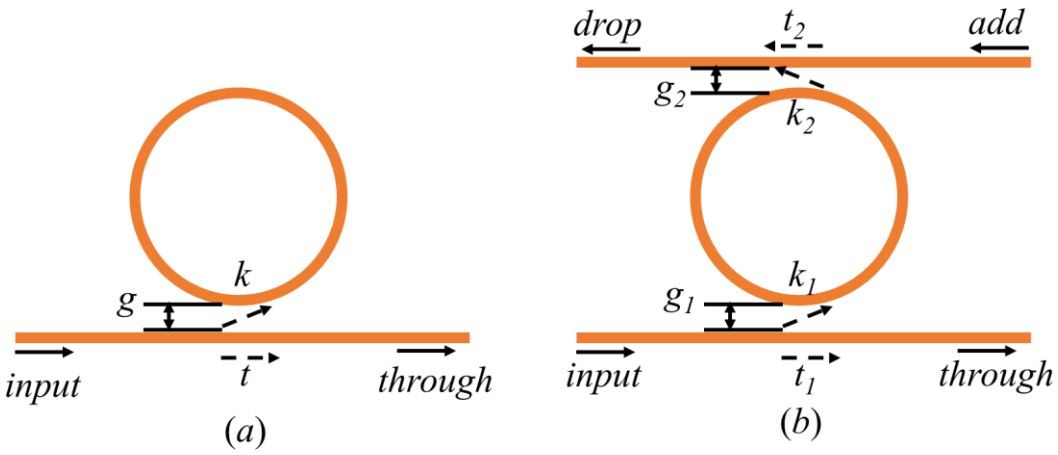

Figure 4.6: *Waveguide Micro-ring resonator (a) single bus waveguide based ring resonator, also known as all pass filter. (b) Micro-ring resonator based on two coupled bus waveguides, also known as add and drop ring resonator.*

where, T_t is the transmission of through port of add and drop ring resonator. The transmission of drop port (T_d) can be written as:

$$T_d = \left|\frac{E_{drop}}{E_{in}}\right|^2 = \left(\frac{(1-t_2^2)(1-t_1^2)a}{1 - 2at_1 t_2 cos\theta + (t_1 t_2 a)^2}\right) \quad (4.13)$$

The FSR of the ring resonator is given as:

$$FSR = \frac{\lambda^2}{n_g L}, \quad (4.14)$$

where, λ is the central wavelength, L is the round trip length, and n_g is the group effective index of the waveguide.

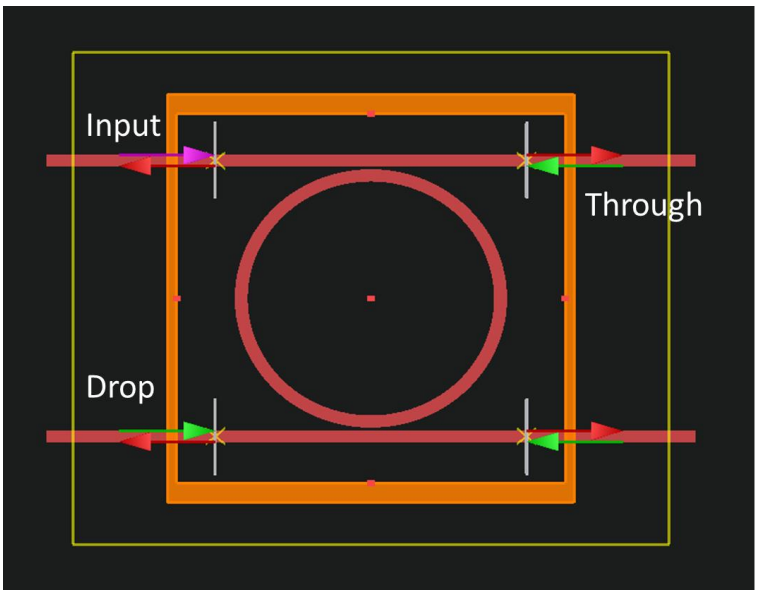

Figure 4.7: *A XY view of an add and drop ring resonator simulated using Lumerical FDTD solution. Where the width of all waveguides is 500 nm and height is 220 nm. The radius of the ring resonator is 5 µm.*

A double bus ring resonator, as shown in Figure 4.7, simulated using Lumerical FDTD solution. The parameters used to simulate the ring resonator using Lumerical FDTD solution are shown in Table 4.2.

The simulated double bus ring resonator using Lumerical FDTD solution is shown in Figure 4.7, whereas, the transmission spectrum of the drop channel and the through channel of the double bus ring resonator is shown in Figure 4.8. Since, the FDTD is the time domain solver hence for computing the spectrum, the software computes the Fourier transform of the signal with certain number of coefficients, which results the ripple in the spectrum, as can be observed in Figure 4.8. The micro-ring resonator based on SOI platform can be used as an effective device for various nonlinear applications [115]–[118].

.

Table 4.2: *Parameters used to calculate the transmission spectrum of ring resonator using Lumerical FDTD solution*

S. No.	Parameter	Value	SI unit
1.	Gap (g_1)	100	nm
2.	Gap (g_2)	100	nm
3.	Width	500	nm
4.	Height	220	nm
5.	Simulation time	10000	fs
6.	FDTD mesh size	3	-
7.	Operating wavelength range	1500 – 1600	nm
8.	Boundary condition layers	32	-

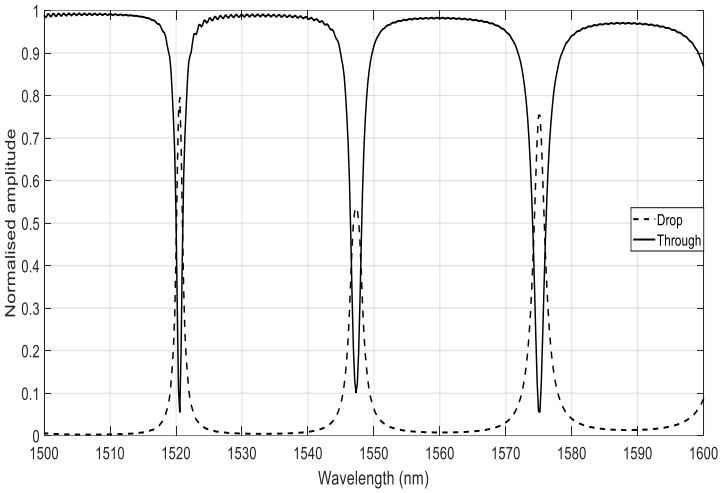

Figure 4.8: *FDTD simulated ring resonator output of through and drop port.*

4.4.3 Mach Zehnder Interferometer

The Mach-Zehnder interferometer (MZI) is one of the most important device used for various applications in the field of Lightwave communication. The MZI can be constructed using two splitters/combiners with either directional coupler or Y-branches (see section 4.4 .1). The first coupler splits the input signal in to two and the two signals acquire different phase shifts if the arm length is different. At the end, both signals are combined by means of another coupler. A schematic of the MZI using two 3 dB DIC is shown in Figure 4.9.

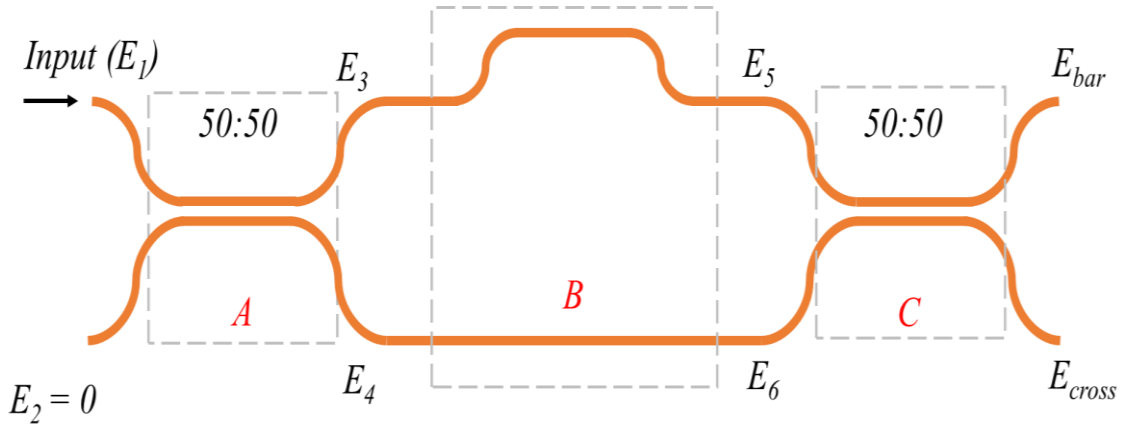

Figure 4.9: *Schematic diagram of silicon photonics technology based Mach-Zehnder interferometer.*

The amount of phase shift depends on the unbalance in the length of the arms of the MZI. As shown in Figure 4.9, the length of upper arm is greater than the length of lower arm hence the upper arm of the MZI will produce an imbalance which create the linear phase shift between the two arms of the MZI.

In order to calculate the transfer function of the MZI, only one input is injected in the MZI, hence $E_2 = 0$. The MZI is divided in to three section, i.e. *A*, *B* and *C* as shown in Figure 4.9. It is assumed that all the arms on SOI platform with waveguide dimension as 500 nm × 220 nm with the coupling ratio of both DIC is 3 dB. The calculations for each section can be found as:

Section A:

In this section, the output from first DIC is determined, i.e. E_3 and E_4, using input E_1; where $E_2 = 0$. The output of the coupler is given as:

$$E_3 = E_1 \frac{1}{\sqrt{2}} \tag{4.15}$$

$$E_4 = E_1 \frac{1}{\sqrt{2}} \exp(-j\frac{\pi}{2}) \tag{4.16}$$

Section B:

In this section, the overall phase shift is computed which is acquired by meaning of unbalancing the MZI arms. The input to second directional coupler can be computed as:

$$E_5 = E_3 \exp(-\alpha L_1 - i\beta L_1) \tag{4.17}$$

$$E_6 = E_4 \exp(-\alpha L_2 - i\beta L_2) \tag{4.18}$$

where, α is the attenuation coefficient, $\beta = \frac{2\pi n_{eff}}{\lambda}$ is the propagation constant of the waveguide with n_{eff} as an effective index of the waveguide and λ as an operating wavelength.

Section C:

In this section, the output of the MZI is determined, i.e. E_{bar} and E_{cross}, using second DIC. The output of the MZI is given as:

$$E_{bar} = E_5 \frac{1}{\sqrt{2}} + E_6 \frac{1}{\sqrt{2}} \exp(-j\frac{\pi}{2}) \tag{4.19}$$

$$E_{cross} = E_6 \frac{1}{\sqrt{2}} + E_5 \frac{1}{\sqrt{2}} \exp(-j\frac{\pi}{2}) \tag{4.20}$$

Finally, the transmission of the MZI is calculated by computing the absolute square of the output of second DIC, i.e.

$$T_{bar} = \left|\frac{E_{bar}}{E_1}\right|^2 \tag{4.21}$$

$$T_{cross} = \left|\frac{E_{cross}}{E_1}\right|^2 \tag{4.22}$$

Consider a broadband source, having a wavelength range of 1500 to 1600 nm, is injected on the SOI based MZI. The imbalance between the two SOI arms is 50

microns. The transmission characteristics of this MZI using equations (4.15) – (4.22) is shown in Figure 4.10.

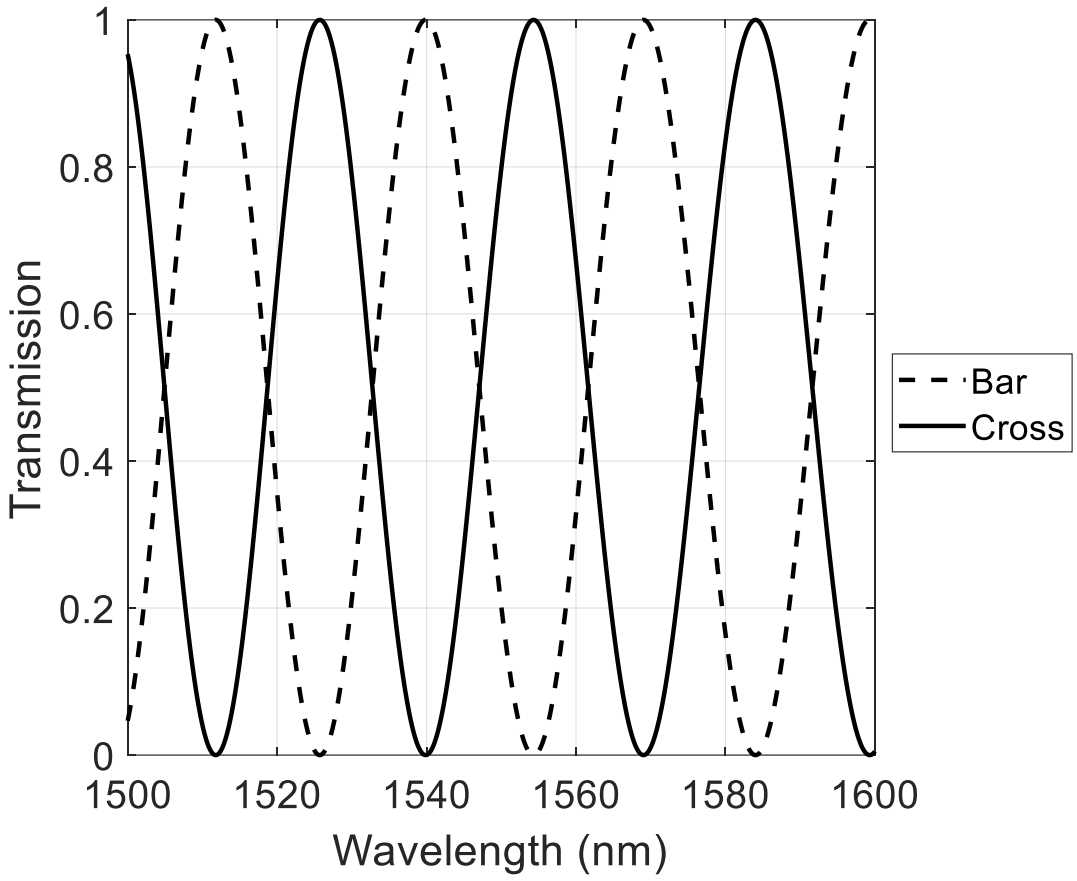

Figure 4.10: *The outputs of the Mach-Zehnder interferometer, i.e. bar and cross, calculated using equations (4.15) to (4.22)*

The MZI can be used as one of the important devices for various nonlinear applications, i.e. nonlinear switching [85], [119]–[121], wavelength conversion [122], [123] and for various other nonlinear applications [124], [125].

4.4.4 Nonlinear Optical Loop Mirror

The nonlinear optical loop mirror (NOLM), also known as the Sagnac interferometer, is an interferometer which consists of a directional coupler and a

fiber/waveguide for nonlinear applications for ultrafast switching [76]. In NOLM, a fiber/waveguide is connected with the two output ports of the DIC, hence this creates a loop. A schematic diagram of NOLM is shown in Figure 4.11.

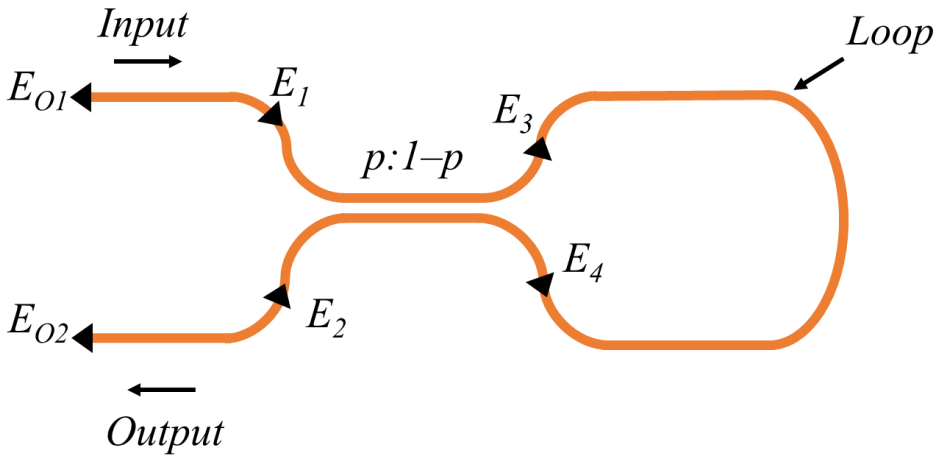

Figure 4.11: *Schematic diagram of silicon photonics based nonlinear optical loop mirror*

In NOLM, light enters in two opposite directions via a directional coupler, one pulse is in propagation direction and another pulse propagates in counter-propagation direction. The strength of the pulse in each direction depends on the coupling ratio of the DIC (i.e. *p*:1-*p*). The coupling ratio can be 40:60, 10:90, or 80:20 but it is not recommended to use the coupling ratio of 50:50 in NOLM for self-phase modulation because the pulse get cancelled with itself hence the overall nonlinear phase shift will be zero and all the power will be reflected back towards it's input port hence this is the reason it is known as loop mirror [76].

Nonlinear loop mirror can be used for nonlinear phenomenon using self-phase modulation and cross phase modulations for all optical switching and signal processing application [126]–[129]. In order to understand the physics behind the NOLM, a simple high power CW source is considered as single input E_1 for the NOLM, hence

E_2 = 0. Like MZI, the NOLM has been divided in to two sections, *A* and *B*, as shown in Figure 4.11. The calculations for each section can be found as:

Section A

In this section, the output of the DIC coupler, E_3 and E_4 are computed using input E_1. The output of the DIC coupler is given as:

$$E_3 = \sqrt{p}E_1 \exp\left(-jp\frac{2\pi n_2 L_{loop}}{A_{eff}\lambda}|E_1|^2\right) \quad (4.23)$$

$$E_4 = \sqrt{(1-p)}E_1 \exp(-j\frac{\pi}{2}) \exp\left(-j(1-p)\frac{2\pi n_2 L_{loop}}{A_{eff}\lambda}|E_1|^2\right) \quad (4.24)$$

where, p is the splitting ratio of the DIC coupler, n_2 is the Kerr refractive index of the nonlinear material, L_{loop} is the length of the waveguide/fiber in the loop, and λ is the operating wavelength of the CW signal.

Section B

In this section, the reflected field (E_{O1}) and transmitted field (E_{O2}) is computed and given as:

$$E_{01} = \sqrt{p}\, E_4 + \sqrt{1-p}\, E_3 \exp(-j\frac{\pi}{2}) \quad (4.25)$$

$$E_{02} = \sqrt{p}\, E_3 + \sqrt{1-p}\, E_4 \exp(-j\frac{\pi}{2}) \quad (4.26)$$

The transmitted power, $T_{nolm} = \left|\frac{E_{02}}{E_1}\right|^2$, and reflected power $R_{nolm} = \left|\frac{E_{01}}{E_1}\right|^2$ are the main ports of NOLM.

Now consider a standard SOI based NOLM, shown in Figure 4.11, with n_2 = 6 × 10^{-18} m^2/W at the wavelength, λ = 1550 nm with A_{eff} = 0.1 μm^2 [85]. The input to the NOLM is a continuous wave signal at the wavelength of 1550 nm and the length of the silicon waveguide in the loop, L_{loop}, is 100 cm. The nonlinear losses, i.e. two photon

absorption and free carrier generation, are considered as zero. Using all these parameters, the simulated SPM effect calculated equations (4.23) to (4.26) is shown in Figure 4.12.

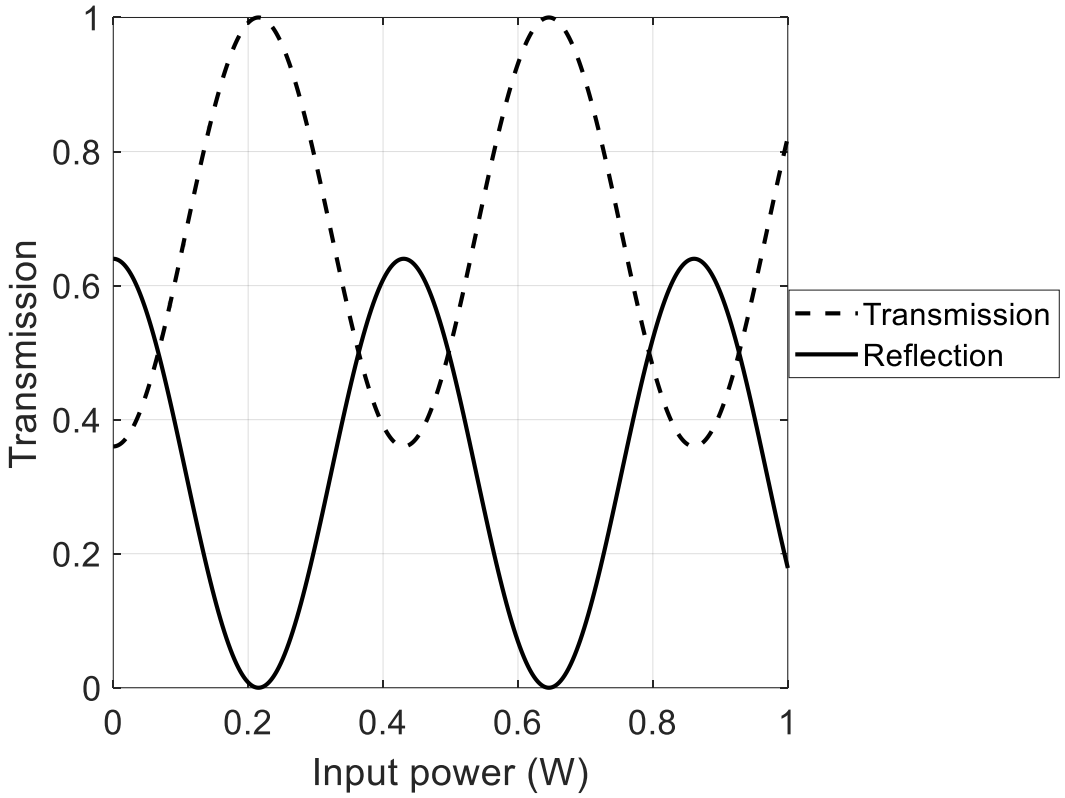

Figure 4.12: *The outputs of NOLM, i.e. transmission and reflection ports, using equations (4.23) to (4.26)*

4.5 Summary

In this chapter, the basics of silicon photonics is explained along with the method to calculate the mode using Lumerical Mode solution software. Also, the standard dimensions of the silicon waveguide, i.e. 500 nm x 220 nm, is discussed. Furthermore, this chapter also included the main devices, i.e. directional coupler, micro ring resonator, MZI and NOLM, used for the various nonlinear applications.

Chapter 5

On-Chip Picosecond Pulse Width Measurement

As discussed in Chapter 3, pulse width is one of the important parameter in the field of Lightwave communication. There are several ways which can measure the optical pulse width but the pulse width in picosecond regime or sub-picosecond regime is still one of the main tasks currently being investigated. The most common ways to measure the pulse width is using FROG and SPIDER. Moreover, there are some high-speed sampling oscilloscopes which can be useful to measure the optical pulse width

in picosecond regime but is too expensive solution. Whereas, optical auto-correlator can also be used to measure the optical pulse width as a laboratory instrument. In this chapter same analogous method has been used as introduced in Chapter 3 for the measurement of an optical pulse width using on chip nonlinear MZI. Unlike NOLM used in Chapter 3; in this chapter, we have used the integrated nonlinear MZI. Since silicon has a strong two photon absorption (TPA) at the telecom wavelength [44] hence the effects of TPA and TPA induced free carrier are considered in the modelling section of this chapter. Section 5.1 introduces the on-chip pulse width measurement techniques using optical waveguide based on silicon photonics and related technologies. The schematic of the device and its description is discussed in section 5.2 The modelling section of the silicon waveguide to calculate the nonlinear phase shift by analytically solving the NLSEs for XPM and SPM using split step method is described in section 5.3 . Section 5.4 listed the important simulated results of the on-chip pulse width measurement using optical power meter. Finally, section 5.5 summarizes this chapter.

5.1 Introduction

The picosecond pulse width has range of applications from biomedical [130] to hydrodynamics [131] and various others [132], [133]. Since the measurement of the picosecond pulse width requires very fast electronics hence the DCA can measure a pulse width up until certain accuracy. In our study, we found that the DCA can measure the pulsewidth up until 8 ps pulsewidth [134]. Below which one requires a high performance sampling oscilloscope or some other methods. The most common pulse

characterization techniques are FROG [61], SPIDER [64] and sonogram [67], but as mention in the Chapter 3, these techniques are used to characterize the amplitude and phase of the pulse. In order to measure the width of the optical pulse, optical auto-correlator is the best available tool. Optical auto-correlator can be used as in-laboratory tool for the pulse-width measurement whereas the method described in Chapter 3, can be used as a portable and handheld device to monitor the pulse width by assuming the shape of the pulse, i.e. Gaussian or $sech^2$ pulse [41]. In this chapter, method introduced in Chapter 3 is modified by replacing the NOLM using highly nonlinear optical fiber with nonlinear MZI using silicon photonics technology. Since crystal silicon has a bandgap energy of 1.12 eV, hence the material becomes transparent for the wavelength from 1.1 μm to onwards. Therefore, it can be used in various optical applications [135]. The high refractive index of the silicon material allows tight confinement of the optical signal and it also exhibits the Kerr refractive index greater than silica of about 100 times greater [136] hence these attractive properties of silicon proves that it can be a good material for various nonlinear applications. There are several methods used to measure/characterize an optical pulse width using SOI based on chip techniques [73], [74], [137]–[139]. Using these approaches, the authors characterize the pulse information such as phase and amplitude whereas, we have shown that the same method introduced in Chapter 3 can also be used for on-chip pulse width measurement of the optical pulse only hence this miniaturize the device size by assuming an envelope of the pulse. Thus the portable device can be more scalable and from the simulation results, it can be seen that this method can be used to monitor the optical pulse width by assuming an envelope of the pulse. The nonlinear Schrodinger equation(s) for the silicon waveguide is modelled using split step method. The

operational wavelength in this work is considered as 1550 nm. Since the effect of TPA in silicon at C-band is significant, therefore, all the nonlinear losses including TPA, and TPA induced free carriers, i.e. free carrier absorption (FCA) and free carrier dispersion (FCD) are taken in to account while performing the nonlinear modelling of the silicon waveguide. The further explained of the simulations is described in section 5.3 of this chapter.

5.2 Device Schematic diagram

In this section, the nonlinear Schrodinger equation(s) for silicon waveguide has been shown for the SPM and XPM. As silicon exhibits certain nonlinear losses, including TPA, and TPA generated carriers, i.e. FCA and FCD, hence all these losses are included in this regards. The schematic diagram of the nonlinear MZI device which is used to measure the pico-second pulsewidth is shown in Figure 5.1. The nonlinear MZI consists of two directional couplers (see section 4.4 for directional couplers) with splitting ratio of 50:50. The output of the first directional coupler is connected to two different types of the waveguides. This is known as the arms of the MZI. The upper arm is consisting of SU-8 (polymer waveguide) with cross section of 2×2 μm^2 and lower arm consisting of silicon waveguide with cross section of 500×220 nm^2. Since the cross section of the SU-8 waveguide is quite large compared to the silicon waveguide hence the properties of SU-8 waveguide does not vary with the input power. Therefore, the upper arm is considered as the linear arm and has no nonlinear effects. As discussed in section 5.1 that silicon has a strong Kerr effect, about 100 times greater than silica, therefore, the properties of the silicon waveguide vary as the

input power is increased. As silicon is used in the lower arm of the MZI, hence this behaves as a nonlinear arm. Both of these waveguides are then connected with another 50:50 directional coupler, similar to the first one. The output of the second coupler, or the output of the MZI is known as bar and cross port (see Figure 5.1). It can be seen that the SU-8 tapers are used at the input and the output side of the MZI and the reason of using these tapers is that the size of the SU-8 waveguide used at the input and output side of the MZI is 2 µm, and the size of the lased fiber is also near 2 µm hence the coupling losses are minimized using the SU-8 waveguide at the input and output end. The mode is further propagated in to the silicon waveguide by tapering the SU-8 waveguide and same applies at the output side of the MZI, shown in Figure 5.1.

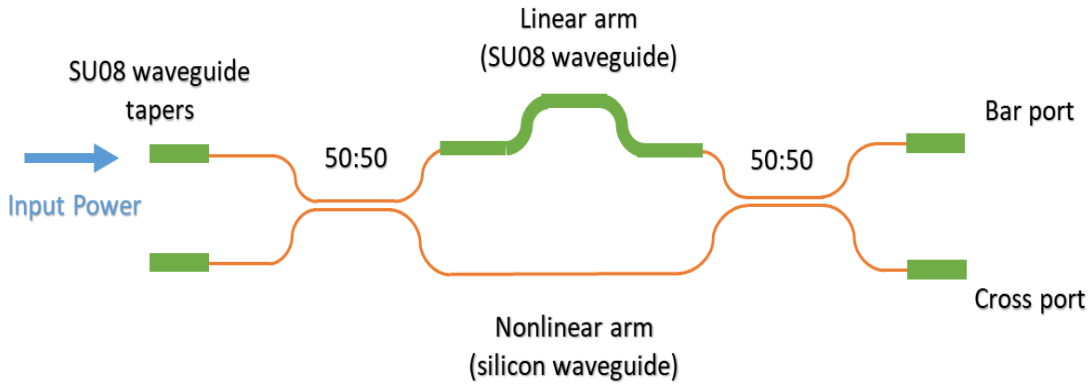

Figure 5.1: *Schematic diagram of the nonlinear MZI comprises of SU8 waveguide in the upper arm and silicon waveguide in the lower arm for picosecond pulse width measurement.*

The length of the linear arm comprises of SU-8 waveguide is L_{SU8} = 12.437 mm and the length of the nonlinear arm comprises of silicon waveguide is L_{si} = 7.87 mm. Since the cross section of SU-8 waveguide is higher than the silicon waveguide hence the optical mode of the linear arm is almost 15 time larger than the nonlinear arm. As can be seen from Figure 5.1 that the upper arm of the MZI is designed longer

than the lower arm; this is because SU-8 waveguide has lower effective refractive index (n_{SU8} = 1.57 at wavelength of 1550 nm) compared to the effective refractive index of the silicon waveguide (n_{Si} = 2.47 at the wavelength of 1550 nm). Therefore, in order to compensate the difference between the effective refractive indices between the two arms, such that the MZI will behave as a balanced device, the upper arm is designed longer than the lower arm.

The nonlinear MZI device shown in Figure 5.1 was fabricated on a CMOS-compatible SOI wafer in the James Watt Nanofabrication Center at Glasgow University. Electron beam lithography was used to define the waveguide layout in high contrast hydrogen silsesquioxane resist. After this step, an inductively coupled plasma reactive ion etching was used to transfer the pattern onto the silicon wafer, and the SU-8 waveguide pattern were then defined by using direct ebeam lithography and development. The sample was finally coated by a 2 μm thick Poly Methyl Methacrylate protective layer. Straight waveguides were also fabricated on the same chip to test linear and nonlinear characteristics of the silicon waveguide.

5.3 Modeling for Silicon Waveguide

As discussed in section 5.2 of this chapter, the nonlinear MZI has two arms with of different materials. The upper arm comprises of SU-8 waveguide hence behaves as linear arm and the lower arm comprises of silicon waveguide hence behaves as nonlinear arm. The nonlinear arm will produce a nonlinear phase shift which is directly proportional to the input peak power. In this section, the nonlinear phase shift produced in the nonlinear arm, i.e. in silicon waveguide, using NLSE is

calculated. In Chapter 3, the phase shift is calculated using NLSE as well but since highly nonlinear fiber HNLF doesn't exhibits the TPA and losses due to TPA generated free carriers therefore the two photon absorption coefficient is zero. But as silicon waveguide do exhibit these losses [44], hence by including these losses, the NLSE for silicon waveguide for SPM is given in equation (5.1) and NLSEs for silicon waveguide for XPM is given in equations (5.2) and (5.3) [44], [85], [140], i.e.:

$$\frac{\partial A}{\partial z}+\frac{i\beta_2}{2}\frac{\partial^2 A}{\partial T^2}=i\gamma|A|^2A-\frac{1}{2A_{eff}}(\beta_{TPA}|A|^2)A-\frac{\sigma}{2}N_dA-i\frac{2\pi k_d}{\lambda}N_dA-\frac{\alpha}{2}A \quad (5.1)$$

$$\frac{\partial A_a}{\partial z}+\frac{\alpha}{2}A_a+\frac{i\beta_{2a}}{2}\frac{\partial^2 A_a}{\partial T^2}=i(\gamma|A_a|^2+2\gamma|A_b|^2)A_a-\frac{1}{2A_{eff}}(\beta_{TPA}|A_a|^2+$$

$$2\beta_{TPA}|A_b|^2)A_a-\frac{\sigma_a}{2}N_dA_a-i\frac{2\pi k_{d_a}}{\lambda}N_dA_a \quad (5.2)$$

$$\frac{\partial A_b}{\partial z}+\frac{\alpha}{2}A_b+\frac{i\beta_{2b}}{2}\frac{\partial^2 A_b}{\partial T^2}=i(\gamma|A_b|^2+2\gamma|A_a|^2)A_b-\frac{1}{2A_{eff}}(\beta_{TPA}|A_b|^2+$$

$$2\beta_{TPA}|A_a|^2)A_b-\frac{\sigma_b}{2}N_dA_b-i\frac{2\pi k_{d_b}}{\lambda}N_dA_b \quad (5.3)$$

where, β_2 is the dispersion parameter (see section 2.3.2), γ is the nonlinear coefficient (see section 2.3.3), A_{eff} is the effective area of the waveguide, β_{TPA} is the two photon absorption coefficient, σ is the FCA coefficient, N_d is the free carrier density, k_d is the FCD and α is the linear absorption coefficient, with the subscript 'a' as pump signal and 'b' as a probe signal. The free carrier density is given as [44], [140], [141]:

$$\frac{dN_d}{dt}=\frac{\beta_{TPA}}{2h\nu}|A|^2-\frac{N_d}{t_c} \quad (5.4)$$

where, h is the Plank's constant and ν is the frequency of the signal. All the values using in this chapter for the simulation for equations (5.1) – (5.3) are shown in Table 5.1. The main difference between the equations (3.4) to (3.6) is the nonlinear losses and carrier generation due to nonlinear losses. Since silica doesn't exhibit any

nonlinear loss (such as TPA) at the telecommunication wavelength, therefore, β_{TPA} = 0 [41]. In silicon waveguide, the power-dependent losses introduced by TPA and FCA reduce the nonlinear interaction length, whereas, FCD introduces a phase-term of opposite sign to that of SPM and XPM.

When the nonlinear losses are zero, the phase shift calculated using NLSEs is equivalent to the Kerr-induced phase shift. The Kerr-induced phase shift for XPM is given by:

$$\emptyset_{Kerr} = 2\gamma L_{eff} P_{peak}, \tag{5.5}$$

where, $L_{eff} = \frac{1-\exp(\alpha L)}{\alpha}$ is the effective length of the waveguide.

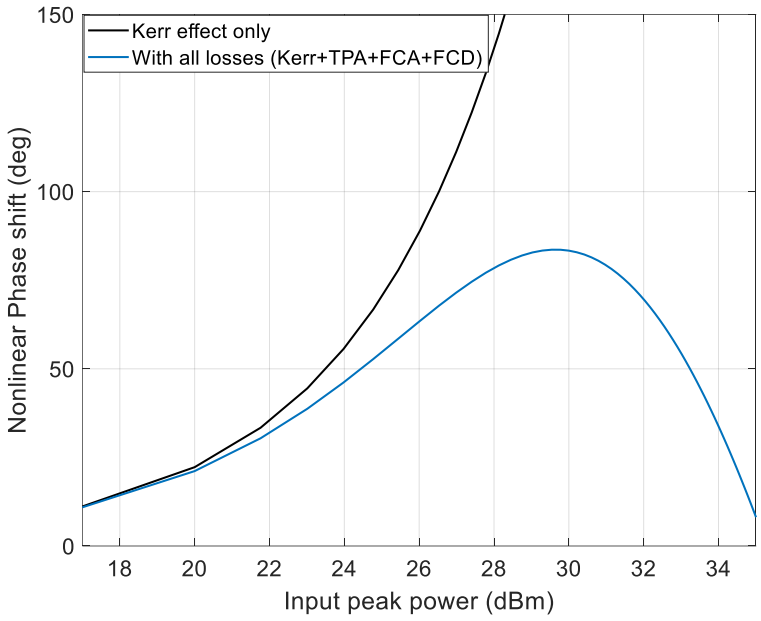

Figure 5.2: *Nonlinear phase shift calculated using split step method for Kerr effect only and Kerr effect along with some nonlinear losses, i.e. TPA and carrier generated though TPA (FCA and FCD).*

Since the same device is considered for the modelling as was considered in [85], therefore, in order to verify the simulation results we calculated the nonlinear

phase shift including all the linear and non-linear losses using split step method. The nonlinear phase shift calculated for XPM using equations (5.2) and (5.3) and the parameters listed in Table 5.1 is shown in Figure 5.2. It can be analyzed that the simulation results shown in Figure 5.2 are in good agreement with those in [85]. Therefore, based on the verification of our simulation results, we repeated the simulations for the pulse-width measurement using optical power meter for the range from 1 ps to 9 ps.

5.4 Picosecond Pulsewidth Measurement Using Nonlinear MZI Based on SOI Platform

In this section, the modelling of the pico-second pulse width measurement is shown using nonlinear MZI device based on the SOI platform. The modelling of the ratio of P_{bar}/P_{cross} as a function of optical switching induced by either by SPM or XPM as a function of input average power is shown. The NLSE for SPM, i.e. equation (5.1), and NLSEs for XPM, i.e. equations (5.2) and (5.3), are numerically solved using split step method [41].

The input parameters used in the simulations are listed in Table 5.1. The repetition rate of the laser is considered to be 10 GHz with the maximum average power limit of 27 dBm as we have considered in our highly nonlinear fiber based experiment (see Chapter 3).

Table 5.1 : *Parameters used for the split step simulations which corresponds the real device.*

S. No.	Parameter	Value	SI unit
1	σ	1.45×10^{-21}	m^2
2	k_d	1.35×10^{-27}	m^3
3	β_{TPA}	5×10^{-12}	m/W
4	n_2	6×10^{-18}	m^2/W
5	L	7.87×10^{-3}	m
6	γ	320	1/(Wm)
7	α	2.4×10^{2}	dB/m
8	A_{eff}	0.1×10^{-12}	m^2
9	h	6.64×10^{-34}	Js
10	c	3×10^{8}	m/s

5.4.1 Nonlinear MZI Simulations for Self Phase Modulation

Figure 5.3 shows the schematic diagram of the SPM scheme. The black box shows the nonlinear MZI which is similar to the one shown in Figure 5.1. In this scheme, only a pulse signal, named as pump signal, is launched at the input port 1 of the MZI, as shown in Figure 5.3. As per [85], the device is perfectly balance in the C-

band (1530 – 1565 nm) that's why the wavelength for mode locked laser, i.e. pump signal, is considered as 1550 nm in the split step simulation. The pump signal is amplified by using high power EDFA and launched in to the input port 1 of the nonlinear MZI. The saturated power of the EDFA in the simulations is considered as 27 dBm; as per availability of our lab. The high power signal after passing through the first directional coupler of the MZI will behaves as linear in the upper arm of the MZI hence no nonlinear effects will be observed whereas since the lower arm comprises of silicon waveguide which introduces the nonlinear effects and modulates the phase shift of the signal which is known as nonlinear phase shift. The nonlinear phase shift is proportional to the peak power of the pump signal; therefore, the overall phase shift will change with respect to the input power.

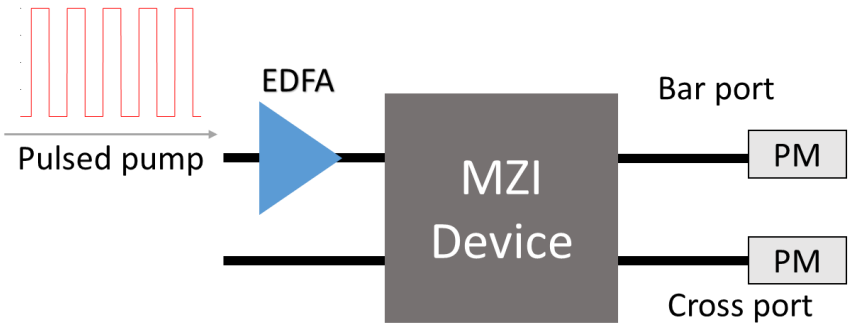

Figure 5.3: *Schematic diagram of the pulse width measurement using SPM scheme, where the MZI device is the device shown in Figure 5.1 and EDFA: erbium doped fiber amplifies.*

As discussed above, the nonlinear phase shift depends on the peak power of the signal itself as per equation (5.5). In order to calculate the output of the MZI, the equations (4.15) to (4.22) are considered. Since the upper arm of the MZI is linear hence the equation (4.17) will be the same whereas since the lower arm of the MZI is nonlinear; thus, the equation (4.18) can be re-written as:

$$E_6 = E_4 \exp(-\alpha L_2 - i\beta L_2 - i\emptyset_{NL\_SPM}) \quad (5.6)$$

where, $\emptyset_{NL\_SPM}$ is the nonlinear phase shift calculated by solving equation (5.1) using split step method. By solving the MZI equations discussed in Chapter 4 and replacing equation (4.18) with equation (5.6), the simulated normalized power measure at bar and cross port of the MZI using slow photo-detector, i.e. optical power meter, is shown in Figure 5.4 (a) and Figure 5.4 (b) respectively. Since the silicon exhibits high nonlinear losses, i.e. TPA, FCA and FCD, therefore, with SPM effect only a certain amount of switching is possible (15% with 1 ps pulsewidth). As the pulse width increases, the carrier accumulation is also increased hence this limits the switching between the two ports of the MZI as observed by Figure 5.4 (a) and Figure 5.4 (b). In order to find the pulse-width, the ratio of normalized power of one output port with other output port is considered at some specific input average power value. From Figure 5.4 (a) and Figure 5.4 (b), it can be observed that the saturation power of the SPM configuration is 10 dBm. Therefore, the ratio of bar power with cross power at the input power of 10 dBm has been considered. This power is named as 'saturated power'. The ratio of saturated bar power and saturated cross power for the SPM setup for the pulse widths ranges 1 to 9 ps, is plotted in Figure 5.4 (c).

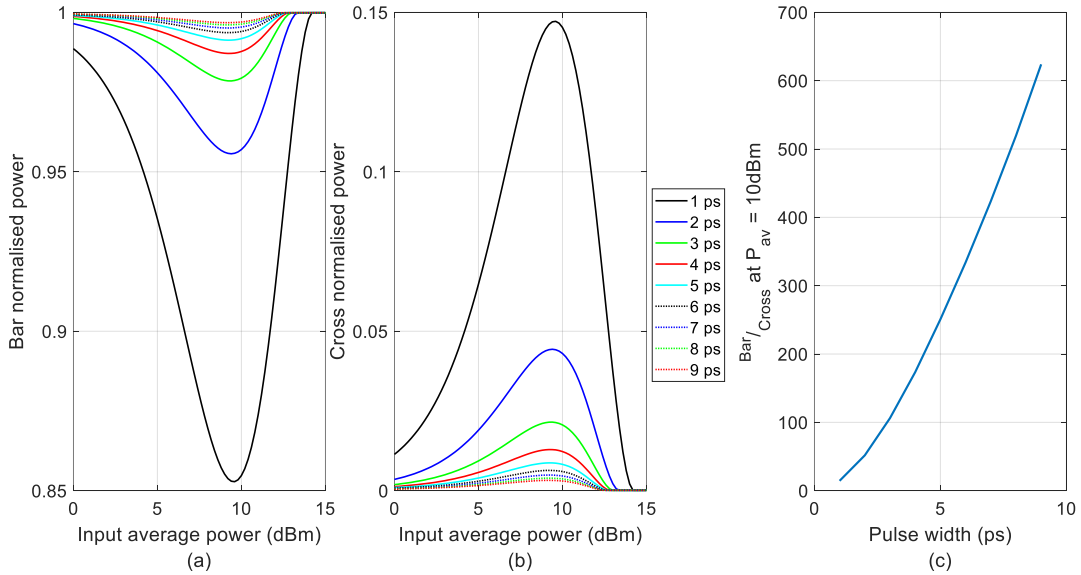

Figure 5.4: *Simulated pulse width measurement using MZI output ports for SPM setup (a) Normalized power at bar port as a function of input average power, (b) Normalized power at cross port as a function of input average power (c) The ratio of bar and cross power at some specific input average power (10 dBm) as a function of input pulsewidth.*

5.4.2 MZI Simulations for Cross Phase Modulation

By doing a minor modification in the SPM setup shown in Figure 5.3, the sensitivity of the device can significantly be enhanced. The modified SPM scheme is shown in Figure 5.5 in which a secondary low power CW laser, known as probe signal, is included; this modified scheme is known as XPM. As explain in section 5.4.1, the MZI is balance in C-band therefore, for simulations the wavelength for a pump signal is considered as same as was considered for the SPM setup, i.e. 1550 nm, whereas the wavelength of a probe signal is considered as 1535 nm.

The XPM scheme is pretty much similar to the SPM one except the additional CW signal. The pump signal is amplified using 27 dBm high power EDFA. Both

signals, high power pump and probe signal, are coupled using a wavelength division multiplexing (WDM) coupler and then launched at the input port 1 of the MZI. One can also use the DIC of 80:20 or 90:10 but the advantage of WDM over the DIC is that the WDM doesn't divides the power hence the power of both signals will remain same at the output port. Since the probe signal is low power signal hence it doesn't introduce any phaseshift but due to presence of the high power pump signal, the phase shift of probe signal is modulated as discussed in Chapter 2. Thus introduces the nonlinear phase shift which is proportional to the input peak power of the pump signal. In order to measure the power of only probe signal at the output of the MZI, i.e. bar port and cross port, another WDM coupler is introduced in order to filter out the high power pump signal, as shown in Figure 5.5.

The same calculations are considered as were used for the SPM setup except the nonlinear phase shift. As mentioned in Chapter 2, the nonlinear phase shift in XPM is approximately twice than the nonlinear phaseshift in SPM [41]. Same set of equations are considered as were considered for the SPM, i.e. equation (4.15) to equation (4.22). Since the upper arm of the MZI is linear that's why the equation (4.17) will be the same. However, as the lower arm of the MZI is nonlinear hence the equation (4.18) can be re-written as:

$$E_6 = E_4 \exp(-\alpha L_2 - i\beta L_2 - i\emptyset_{NL\_XPM}) \qquad (5.6)$$

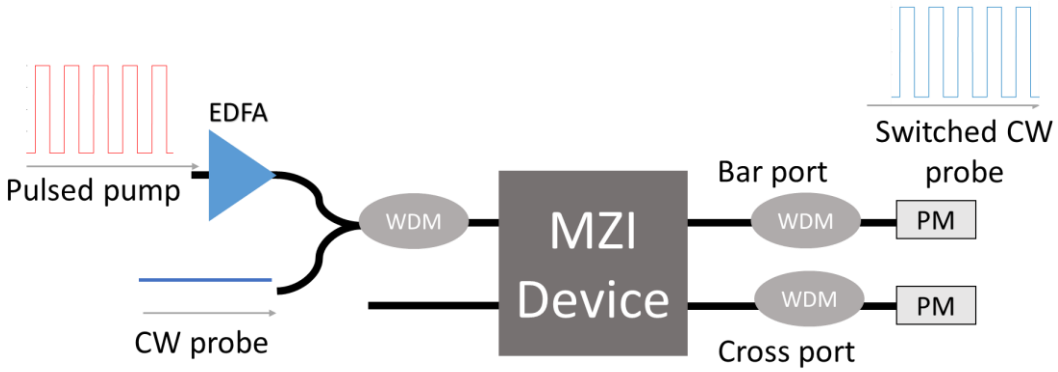

Figure 5.5: *Schematic diagram of the pulse width measurement using XPM scheme, where the MZI device is the device shown in Figure 5.1, EDFA: erbium doped fiber amplifies, WDM: wavelength division multiplexer*

where, $\emptyset_{NL\_XPM}$ is the nonlinear phase shift calculated by solving equation (5.2) and equation (5.3) numerically using the split step method. By solving the MZI equations discussed in section 4.4.3 and replacing equation (4.18) with equation (5.6), the simulated normalized power at bar output port and cross output port of the nonlinear MZI for XPM scheme using slow photo-detector, i.e. optical power meter, is shown in Figure 5.6 (a) and Figure 5.6 (b), respectively. From the both Figure 5.6 (a) and Figure 5.6 (b), it can be observed that by using the XPM scheme, the power sensitivity of the device is increased significantly which makes it useful and easy to measure more pulsewidth range compared to the SPM scheme.

The concept of saturated power is also introduced for XPM as was considered for SPM. But the saturated power of the XPM is approximately double that of SPM hence the average power at 12 dBm is considered to be the saturated power for the XPM setup. Figure 5.6 (c) shows the ratio of saturated bar power and saturated cross power for the XPM setup for the pulse widths ranges 1 to 9 ps. Hence, using the curve

shown in Figure 5.6 (c), the pulse width of an optical signal can be measured using small range of input power, up to 12 dBm, with more accuracy.

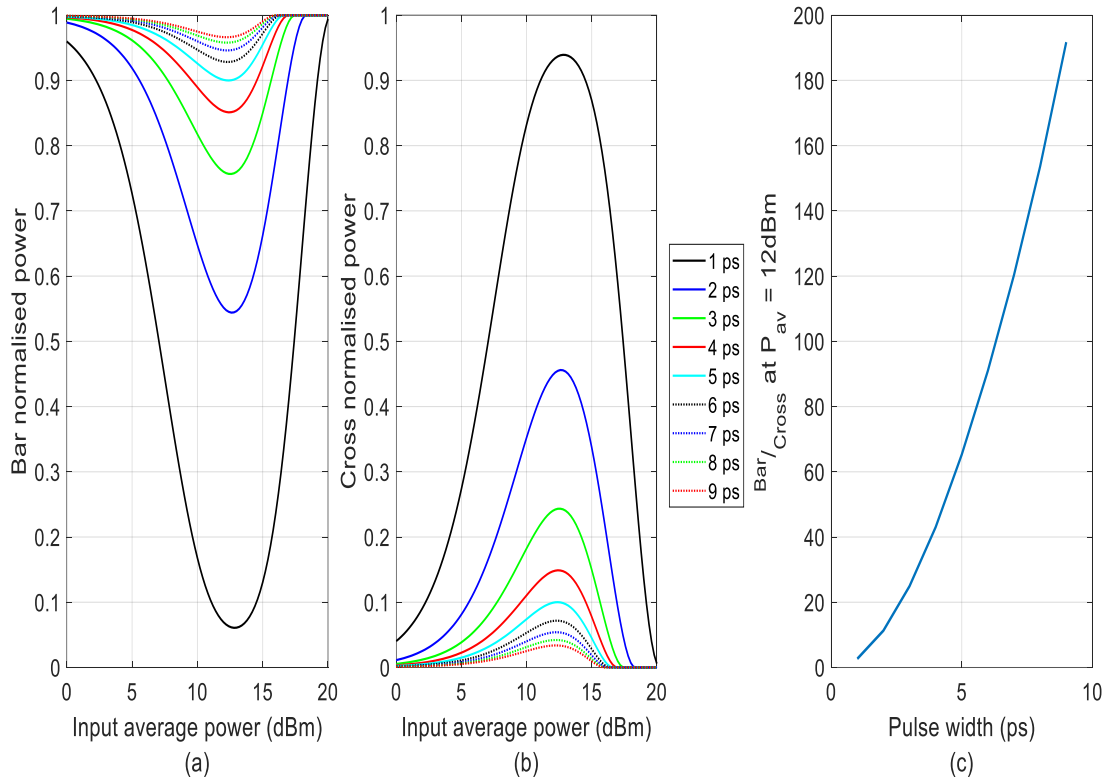

Figure 5.6: *Simulated pulse width measurement using MZI output ports for XPM setup (a) Normalized power at bar port as a function of input average power, (b) Normalized power at cross port as a function of input average power (c) The ratio of bar and cross power at some specific input average power (12 dBm) as a function of input pulsewidth.*

5.5 Summary

In this chapter, we have presented on-chip nonlinear Mach-Zehnder interferometric design for determining optical pulse widths using measurement of average power using slow detectors hence miniaturization the device. Pulses in the range of 1–9ps were simulated using SPM and XPM setup with a maximum required input average power as 15 dBm. This method may find its use in distributed networks

or as a bolt-on to optical systems using ultra-short pulse sources. In order to minimize the nonlinear losses introduced by the silicon waveguide, i.e. TPA, and TPA generated free carriers (FCA and FCD), the nearest option can be to use the silicon rich nitride waveguide as the TPA is not reported in these waveguide up until the peak power of 50 W [142] and it has a good nonlinear coefficient (i.e. 6.1 $(Wm)^{-1}$ [143]), hence solves the issue of TPA which can increase the range of this device significantly.

Chapter 6

Athermal Interferometer Based on Tailored Subwavelength Metamaterials

Temperature sensitivity is an important parameter that has to be considered while working with any PIC device. The properties of the material vary as the temperature is varied (depending on the thermo-optic coefficient of the material), hence temperature alters the behavior of the device. In this chapter, a novel method

has been introduced which can compensate the effect of temperature for SOI technology using state of the art subwavelength grating metamaterials. The temperature compensation is introduced by tailoring the subwavelength structure in the MZI. This device can be used for the application on the nonlinear optical devices [41] and also, the proposed device can be useful for on-chip microspectrometer [144] devices. The other useful literature to design the compensated thermo-optic effect is also listed in this chapter. The breakthrough of this chapter is as follow: Section 6.1 introduces the main temperature constraints of the devices based on silicon photonics technology. This section also listed the most common methods available in the literature for the compensation of thermo-optic response. Furthermore, it also includes the targeted applications of the proposed device. Section 6.2 shows the operation principle of the proposed thermo-optic compensated MZI device using subwavelength gratings, and its modelling parameters. The athermal design of the MZI is listed in section 6.3 in which the results are swept for various ranges of lengths, widths and duty cycle (*DC*) to get the best and optimum parameters for an athermal MZI device. Since there are some errors while fabricating any device, therefore, a discussion on how much the main results are deviated when considering the fabrication errors is listed in section 6.4. Since most of the devices are limited to certain wavelengths, hence, a broadband response is more demanded. In section 6.5, the bandwidth enhancement of the proposed device is discussed, the scalability of the proposed athermal MZI for various FSR is also discussed in this section. Finally, section 6.6 describes the summary of this chapter.

6.1 Introduction

Silicon photonic technology has tremendously been growing since last decade due to its various advantages. The few key advantages are: the compatibility with the CMOS, the high optical confinement between silicon and SiO_2 to form a SOI wafer, strong Kerr effect and many more [86], [145]. Apart from all these exciting advantages, one of the main issue in the silicon photonic technology is high thermo-optic coefficient. The thermo-optic coefficient of silicon is $1.8 \times 10^{-4}\ K^{-1}$ and $1.2 \times 10^{-4}\ K^{-1}$ at 1.55 μm for the TE and TM polarization, respectively [36]. The temperature sensitive devices including broadband switching, high-speed modulator and WDM filters are very sensitive to change temperature hence slight variation in the temperature can affect the performance significantly. Any change in material properties (i.e. due to temperature, pressure or any other effect) can vary the device performance. The temperature dependency on nonlinear optical application and micro spectrometer is discussed in section 6.1.1 and 6.1.2 respectively. Due to the high thermal dependence of silicon waveguides even small temperature variations will produce phase errors. This imposes very demanding thermal stability requirements and limits the device applicability and performance. Several methods have been proposed for a design of a temperature insensitive MZIs and ring resonators [38], [39], [146]–[150]. The most common approach is to use a polymer as the cladding material due to its negative thermo-optic coefficient [38], [146]. This solution is limited by the polymer dependence on changing environment conditions such as the moisture or mechanical pressure. Titanium oxide (TiO_2) [147], [148] or a combination of TiO_2 and silicon nitrite (Si_3N_4) [149] have been also proposed as cladding alternatives.

However, for any given material platform, the thermal independence can be also achieved by combining segments having different geometries and thermal responses. In particular, by introducing temperature compensating segments as wider or narrower waveguides than those forming the MZI (thus introducing a different thermos-optic response) and/or adequately designing their relative lengths, the overall MZI thermal response can be controlled [39], [150]. This opens a promising path for a nonlinear optical athermalization. Enhancements of the MZI operational bandwidth and resilience to fabrication deviations from a nominal design are also possible and will be discussed.

Subwavelength gratings with a polymer cladding have already been proposed for use in athermal waveguide designs [151], [152]. SWG [153] are alternating dispositions of core and cladding materials periodically arranged with a period much smaller than the wavelength of the propagating light. Diffractive and Bragg effects are therefore suppressed and the approach effectively generates a homogeneously behaving optical metamaterial. The effective refractive index and dispersive properties of SWG structures can be tailored by modifying the grating period (Λ) and its duty cycle (DC) [40]. This enabled a design of broadband [154] or MMIs [155] couplers including mode multiplexers [156], just to give a few examples. Because the thermo-optic response of the SWG waveguide (compare to conventional wire waveguides) strongly depends on the thermo-optic coefficient of the cladding material, it is the basis for polymer-based athermal solutions [151], [152] in the aforementioned compensation of the thermo-optic effect in passive silicon photonics platforms.

In this chapter, an athermal MZI with a tailored SWG waveguide is presented. The use of SWG circumvents the need for polymer claddings. It also adds an extra

degree of ‘design freedom’ for controlling the SWG effective refractive index and dispersion through adjusting the SWG duty cycle and dimensions. This approach also enables the optimization of the MZI athermalization bandwidth, sensitivity to fabrication errors, and is a good alternative to the established waveguide manipulation techniques [39], [150]. Our athermal MZI design achieved the minimal overall temperature sensitivity reported to date, i.e. ± 4 pm/K. This was obtained for a 75 mm long MZI in a 100 nm wavelength rage around 1550 nm. Performance simulations show that the MZI is insensitive to waveguide length variations up to ± 0.355 mm.

6.1.1 Temperature Dependency on Nonlinear Optical Communication

Suppose a MZI device is design for a 50% optical switching between the two output ports of the MZI (i.e. bar and cross) due to nonlinear effects (XPM or SPM) at certain power levels. Due to change in the room temperature, the refractive index is changed which can additionally contribute in the phase change of the device, thus, the switching ratio between the two output ports of the MZI will not be same as it was on room temperature. There is a possibility that one can increase or decrease the power level to keep the switching ratio constant but in devices like silicon which has very high TPA and carrier effect [79] and they both are proportional to the input power of the optical signal hence in such situation one cannot increase the power beyond a certain limit. In [157], the authors have experimentally found that the Raman scattering in SOI waveguides is strongly dependent on the temperature. The authors have observed that the Raman gain at the temperature of 77 ^{0}K is greater than the free

carriers absorption loss which is generated through TPA. In [158], the authors have found that when the room temperature is down up until 150 K, the free carrier absorption is reduced by one order of the magnitude from its value at the room temperature. Hence it can be said that as the temperature is increased, the free carrier absorption loss is also increased therefore one need more power to achieve the targeted nonlinear phase shift than at room temperature. Therefore, a fully temperature compensated device is required for proper nonlinear application.

6.1.2 Temperature Dependency on Microspectrometer

On-chip Fourier-transform (FT) microspectrometers can also be the possible application for the proposed athermal MZI device. The on chip FT microspectrometers have shown remarkable potential in the field of integrated spectroscopy [144], [159]. They offer an improved signal-to-noise ratio (SNR) and optical throughput (*étendue*) over traditional FT systems [160], while circumventing the need for moving or active elements [161]. Unlike other types of microspectrometers [162]–[165], on-chip FT microspectrometers offer multiple-aperture schemes and an independent channel calibration. The integrated FT spectrometer can be implemented through an array of waveguide based MZI with linearly increasing optical path differences (OPD). The response of all MZIs generates a stationary interferogram that is instantly ‘measured’ by an array of photodetectors for ensuring the measured spectrum retrieval [166]. In addition, the SOI high mode confinement, thanks to the silicon high refractive index (3.47) at 1550 nm, [45] and the ability of different implementations of optical delays,

had enabled achieving high resolutions and compact footprints. The most common approaches to delay designs are microphotonic spirals [144] or subwavelength metamaterials [167]. Although these techniques were originally developed for a fiber C-band (1.529 - 1.56 μm), the versatility and offered advantages promoted their extension also into other wavelength ranges, namely the mid-infrared (3 - 8 μm) [168]. Here, the important application is an absorption sensing. The spectral resolution ($\delta\lambda$) and FSR of an FT spectrometer (FSR_{FT}) based on *N* MZIs is given as:

$$\delta\lambda = \frac{\lambda_0^2}{|\Delta L_{max} n_{g_2} + L(n_{g_3} - n_{g_2})|} \tag{6.1}$$

$$FSR_{FT} = \delta\lambda \frac{N}{2}, \tag{6.2}$$

N = 32 was used in [144]. ΔL_{max} is a maximum path length difference for the MZI, n_{g_2} is a group index of the wire waveguide, and n_{g_3} is a group index of the SWG waveguide.

However, the operation of the FT microspectrometer implies some technological challenges. Fabrication errors, especially deviations from waveguides nominal width, will produce arbitrary variations in the effective refractive index of silicon waveguides and therefore the OPD and transfer function of each MZI would be affected. Resulted phase errors degrade the interferogram and limit the spectral resolution of these devices. These type of errors can be avoided by implementing heaters [169] or fully passive spectral retrieval techniques [144], [170]. Both methods require maintaining stable environmental conditions between the time of calibration and operation. Due to the high thermal dependence of silicon waveguides, even small temperature variations will produce phase errors. This imposes very demanding thermal stability requirements and limits the device applicability and performance.

Software techniques relying on a temperature-sensitive calibration [171] have been developed to improve the resolution down to 17 pm. However, hardware athermalization of Mach-Zehnder interferometers can also be used for further resolution enhancements. Therefore, a fully temperature compensated device is required.

6.2 Operation Principle

A schematic structure of the proposed athermal MZI is shown in Figure 6.7, where two differently structured MZI arms based on wire and SWG waveguides are coupled using two 50:50 directional couplers. In the upper arm, only a wire waveguide is used, whereas in the lower arm a combination of both, the wire waveguide and SWG waveguide is implemented. Modes propagating in each arm of the MZI will experience a corresponding change of the effective refractive index ($\frac{dn_{eff}}{dT}$) due to temperature fluctuations. Since the effective index of a waveguide also depends on its width and height [45] (in our design the height is kept constant and equal to 220 nm), if appropriately choosing the width and length of both arms, the total change $\frac{dn_{eff}}{dT}$ in the upper arm can be cancelled by the total change in the lower arm. Thus, the overall temperature sensitivity of the MZI (at the targeted operational wavelength) can be brought to a zero. In order to understand the above concept, we decompose MZI arms into two sections:

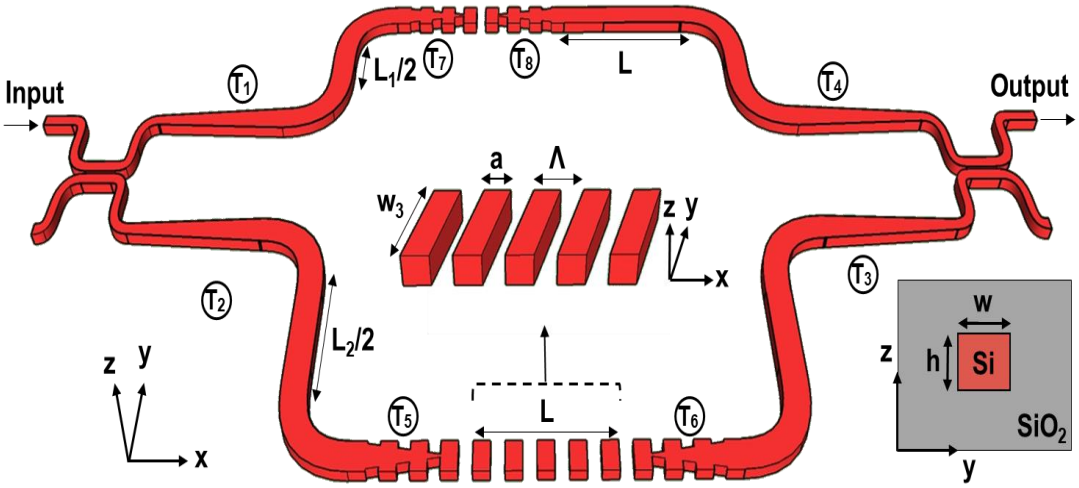

Figure 6.7: *Schematic diagram of the proposed athermal interferometer based on tailored subwavelength metamaterials. The central inset shows in detail the schematic of the subwavelength waveguide (lower arm), whereas the corner inset presents the geometry of the wire waveguide (upper arm).*

1. Section called a *delay section* is used in both arms and uses the same waveguide geometry (therefore has the same effective refractive index and thermo-optic response) but has a different length L_1 in the upper arm and L_2 in the lower arm.

2. *Thermal compensating section*. This section has the same length L in both arms but different structures: the wire waveguide is used in the upper arm and SWG in the lower arm.

In order to optimize the MZI's athermal design, we have considered different waveguides and their widths (see Figure 6.7). MZI input and output waveguides have a fixed width (W_1). The wire and SWG waveguides are forming MZI arms. Their width is W_2 and W_3, respectively and will be optimized as is described in section 6.3. Four trapezoidal tapers (T_1 – T_4) [172] (two per each arm), each having a length of 120 μm [173], are used to adiabatically adapt the mode size from the narrower input/output

waveguide (width W_1) into the MZI wire waveguide (width W_2). Since dimensions of tapers are the same in both arms thus, as per the property of the MZI, the overall temperature sensitivity due to the presence of T_1 and T_4 in the upper arm is cancelled with the same overall temperature sensitivity of T_2 and T_3 in the lower arm. SWG tapers ($T_5 – T_6$), each having a length of 50 µm [153], are included in the lower arm of the MZI to minimize the transitions loss between wire and SWG waveguides. In order to remove the effect of tapers $T_5 – T_6$ from OPD and thermal calculations, two identical back-to-back tapers ($T_7 – T_8$) were included in the upper arm.

The response of the described athermal MZI is then given as:

$$m\lambda_0 = n_{eff_2}.\Delta L + \Delta n_{eff}.L \tag{6.1}$$

where n_{eff_2} is an effective index of the MZI wire waveguide; $\Delta L = L_2 - L_1$ is a physical length difference between both MZI arms; $\Delta n_{eff} = n_{eff_3} - n_{eff_2}$ is an effective index difference between SWG and wire waveguides; m (if an integer) indicates the order of a constructive interference at the wavelength λ_0; m (if chosen a half integer) will result in a destructive interference. When considering the waveguides dispersion, the interference order (M) of the MZI can be written as [39], [150]:

$$M = m - \Delta L \frac{dn_{eff_2}}{d\lambda} - L \frac{d(\Delta n_{eff})}{d\lambda} \tag{6.2}$$

The FSR of an athermal MZI is defined by [39], [150]:

$$\lambda_{\mathrm{FSR}} = \frac{\lambda_0}{\mathrm{M}} \tag{6.3}$$

and the overall temperature sensitivity (S) of this athermal MZI at any specified wavelength (λ_0) is given as [39], [150]:

$$S = \frac{\Delta\lambda 0}{\Delta T} = \frac{\Delta L \frac{dn_{eff_2}}{dT} + L\frac{d\Delta n_{eff}}{dT}}{M}. \quad (6.4)$$

Because silicon has a positive thermo-optic coefficient, the first term of equation (6.4) is always positive. The term $\frac{d\Delta n_{eff}}{dT}$ in equation (6.4) can be made negative by choosing parameters of the wire and SWG waveguide such that the effective index of the SWG waveguide (n_{eff_3}) is lower than the effective index of the wire waveguide (n_{eff_2}). Therefore, by appropriately choosing the width and duty cycle of the SWG waveguide, then adequately selecting the length of each waveguide section, the temperature sensitivity at any specific wavelength of the MZI can be annulled.

In order to evaluate the performance of such athermal MZI, two parameters were defined: a relative optical path difference (r_{OPD}) and total temperature sensitivity (S_{total}). r_{OPD} is given by equation (6.5). It relates a physical length of the MZI longest arm to the optical path difference attained when the athermal condition is met. That is, higher r_{OPD} values will result in the more compact device with the target *OPD* value. In other words, for a fixed OPD value, the shorter the total length of a device, the higher its r_{OPD} value will be. This means, more compact spectrometers with a desired resolution can be designed and build:

$$r_{OPD} = \frac{OPD}{L_1 + L_2 + 2L} \quad (6.5)$$

S_{total} is given by equation (6.6). It helps to evaluate the MZI athermalization bandwidth by determining variations of *S* for a given wavelength range (λ_{min}, λ_{max}):

$$S_{total} = S_{max} - S_{min} \quad (6.6)$$

where S_{max} and S_{min} is the maximum and minimum temperature sensitivity within the aforementioned wavelength range.

Finally, to ensure we can compare obtained results with those in [39], we define a length variation (δL) as a maximum allowed deviation from a 'common' length L (see Figure 6.7) that preserves the value of S within a ± 1 pm/K range (at the central wavelength).

6.3 MZI Athermal Design

In this section, we present the optimization of the MZI and its SWG geometrical parameters in order to achieve the best device performance in terms of r_{OPD} and S_{total} for a standard SOI platform with a silicon cladding. All effective index computations of the SWG waveguide Bloch modes were done using a commercial Lumerical FDTD solution by considering a TE polarization and the central wavelength 1550 nm for all studied cases. Effects of temperature changes on the effective index of the SWG and wire waveguide were calculated by considering a thermo-optic coefficient of Si as $1.86 \times 10^{-4} K^{-1}$ and of oxide cladding as $1 \times 10^{-5} K^{-1}$ [36].

A standard core thickness of h = 220 nm (see Figure 6.7) and a fixed input/output waveguide width of W_1 = 450 nm was considered for all our designs. Also using Λ = 220 nm in the SWG region avoids Bragg effects while guarantee a feature size that can be 'straightforwardly' fabricated by conventional e-beam techniques. In order to ensure the mono-mode operation, we limited 'optimization boundaries' of W_2

and W_3 to 350 - 600 nm and 400 - 600 nm, respectively. Likewise, we defined the minimum *DC* as 40% and maximum *DC* as 60%.

To enable comparing of our results with [39], the first step was to find a path length difference ΔL at which the target δL is achieved (i.e., δL = 0.711 mm and S ±1 pm/K at the central wavelength).

In order to find the targeted δL, we have plotted the relationship between ΔL and δL by solving the equations (6.1) to (6.4) and the results are shown in Figure 6.8 (a) for parameters W_2 = 500 nm, W_3 = 500 nm, DC = 50%. Once the targeted δL was achieved, the next step was to calculate the 'common length' L of the waveguide at that particular value of ΔL. The found relationship between ΔL and L is shown in Figure 6.8 (b). Both relations were found using equations (6.1), (6.2) and (6.4). It can be seen that the relationship between δL and ΔL and between ΔL and L (see Figure 6.8 (a) and Figure 6.8 (b), respectively) are linear. Therefore, in order to ease the calculations, first gradients ($m_{\delta L \Delta L}$) between δL and ΔL and second gradient ($m_{\Delta L L}$) between ΔL and L, were considered for further calculations.

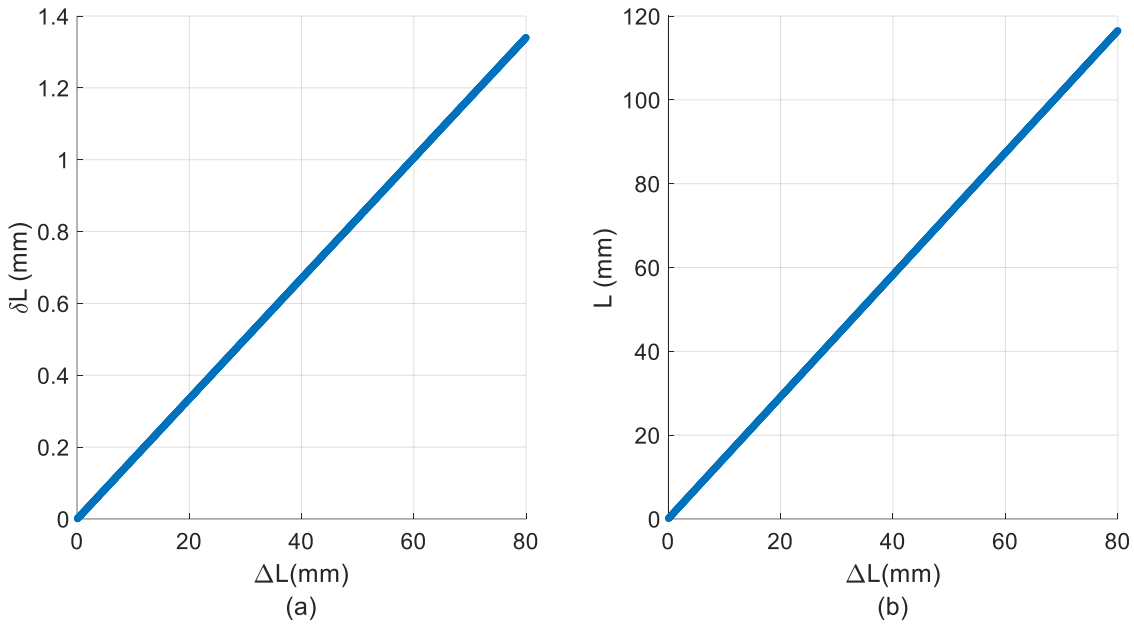

Figure 6.8: *(a) Relation between the total variation in common waveguides (δL) at which the S is within ±1 pm/K, and the path length difference between the two arms (ΔL) of the MZI. (b) Relation between the common waveguides length (L) and the path length difference (ΔL). The parameters for SWG and wire waveguides are W_2 = 500 nm, W_3 = 500 nm and DC = 50%.*

Both gradients are computed for scenarios discussed earlier by sweeping DC between 40% and 60%, W_2 between 350 - 600 nm, and W_3 between 400 - 600 nm. Gradient values $m_{\delta L \Delta L}$ are shown in Figure 6.9 (a) – (c), whereas gradient values $m_{\Delta LL}$ are shown in Figure 6.9 (d) – (e). In order to optimize r_{OPD}, we need high $m_{\delta L \Delta L}$ and low $m_{\Delta LL}$ values. Although parameters $m_{\delta L \Delta L}$ and $m_{\Delta LL}$ show similar tendencies, an optimal ratio can be found for larger widths and duty cycles. Given the aforementioned constraints, we have chosen W_3 = 600 nm, W_2 = 600 nm, and DC = 60%. This leads to the length L = 50.62 mm and ΔL = 23.56 mm while still maintaining the value of δL = 0.711 mm a constant.

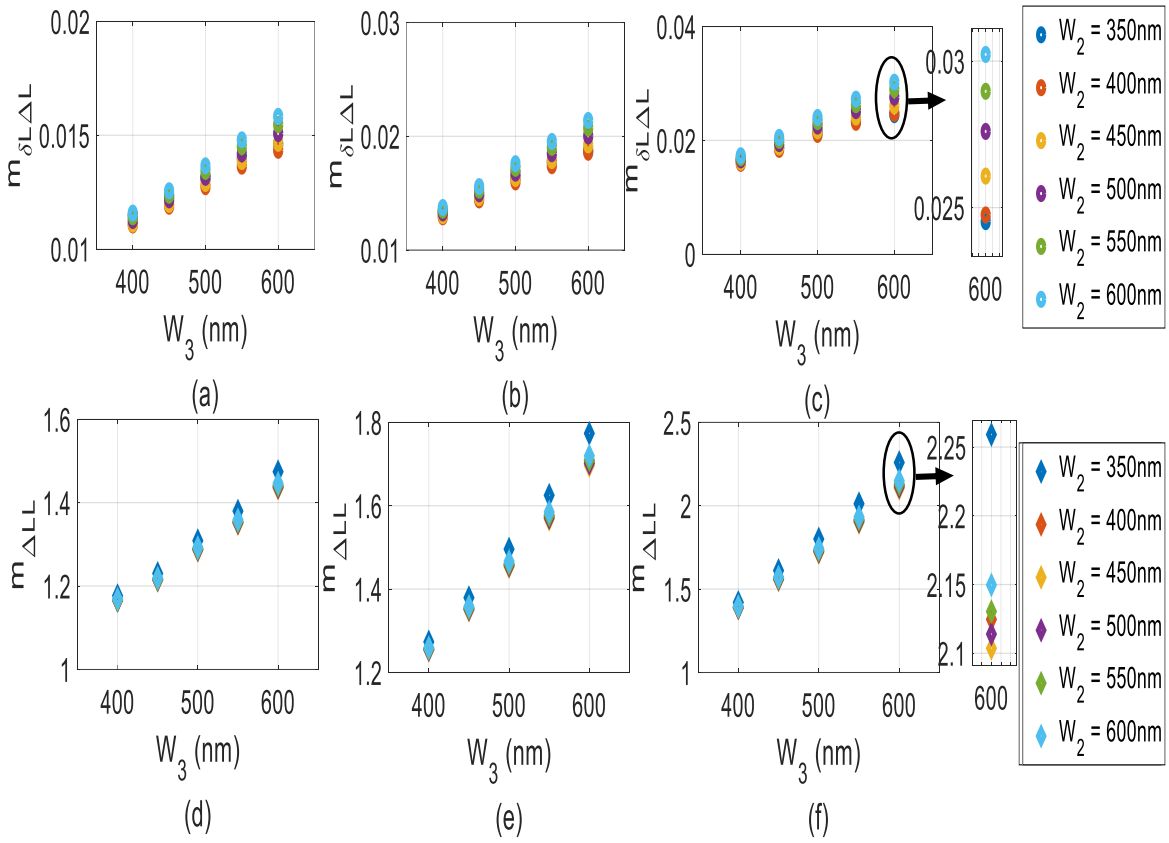

Figure 6.9: *(a)–(c) Gradient between δL and ΔL for DC = 40%, DC = 50% and DC = 60%. (d) – (f) Gradient between L and ΔL for subwavelength duty cycles DC = 40%, DC = 50% and DC = 60%. The inset shows the zoomed version of the data.*

Now, by numerically solving equations (6.1), (6.2), and (6.4) for each wavelength separately, the spectral response of the athermal MZI based on the proposed design is shown in Figure 6.10 by a blue-solid line for a 100 nm wavelength range when using an optimal r_{OPD} (W_3 = 600 nm, W_2 = 600 nm, DC = 60%, L = 50.62 mm and ΔL = 23.56 mm). The temperature sensitivity for L + 0.355 mm and L - 0.355 mm is shown as black-dashed and red-dotted lines, respectively. Our evaluation of the broadband operation of the MZI around the targeted central wavelength λ_0 = 1550 nm for the maximum allowed deviation of -10 pm/K was found to be from 1500 to 1600

nm. Note, in this particular case, achieving the MZI footprint through r_{OPD} was prioritized over its spectral response flatness (S_{total}). The spectral response flatness can be further optimized and will be discussed section 6.5. Note, also spiral waveguides could be used to further reduce the overall device footprint if desired.

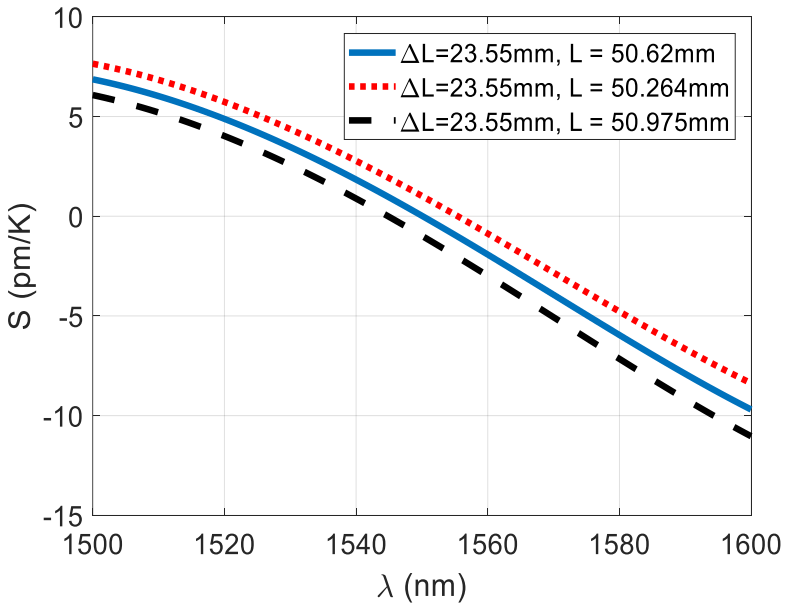

Figure 6.10: *Temperature insensitivity S of athermal MZI as function of wavelength for W_2 = 600 nm, W_3 = 600 nm, DC = 60%, L = 50.62 mm and ΔL = 23.56 mm is shown in blue solid line. Black dashed and red dotted line shows S for L + 0.355 mm and L – 0.355 mm, respectively.*

6.4 Resilience to Fabrication Errors

In order to analyze how fabrication deviations from nominal values may affect the performance of a proposed athermal MZI, we simulated the width variations of its wire and SWG waveguides and duty cycle errors in the SWG region. These effects were first considered independently and then jointly. In particular, we considered variations of ± 20 nm of the width in both waveguides (i.e. W_2 and W_3), and ± 2%

variations of the DC. Figure 6.11 shows the degradation of the temperature sensitivity (S) for W_2 and W_3 ranging between 580 to 620 nm and DC ranging between 58 to 62 %. One can see, that variations in W_2 and W_3 values have a significant impact on S (up to - 16 pm/K), however this impact can be mitigated by properly selecting the corresponding DC value to generate an opposite effect. Also notice, that the intrinsic high dependence of the SOI platform on fabrication errors is improved by mode delocalization in the SWG region.

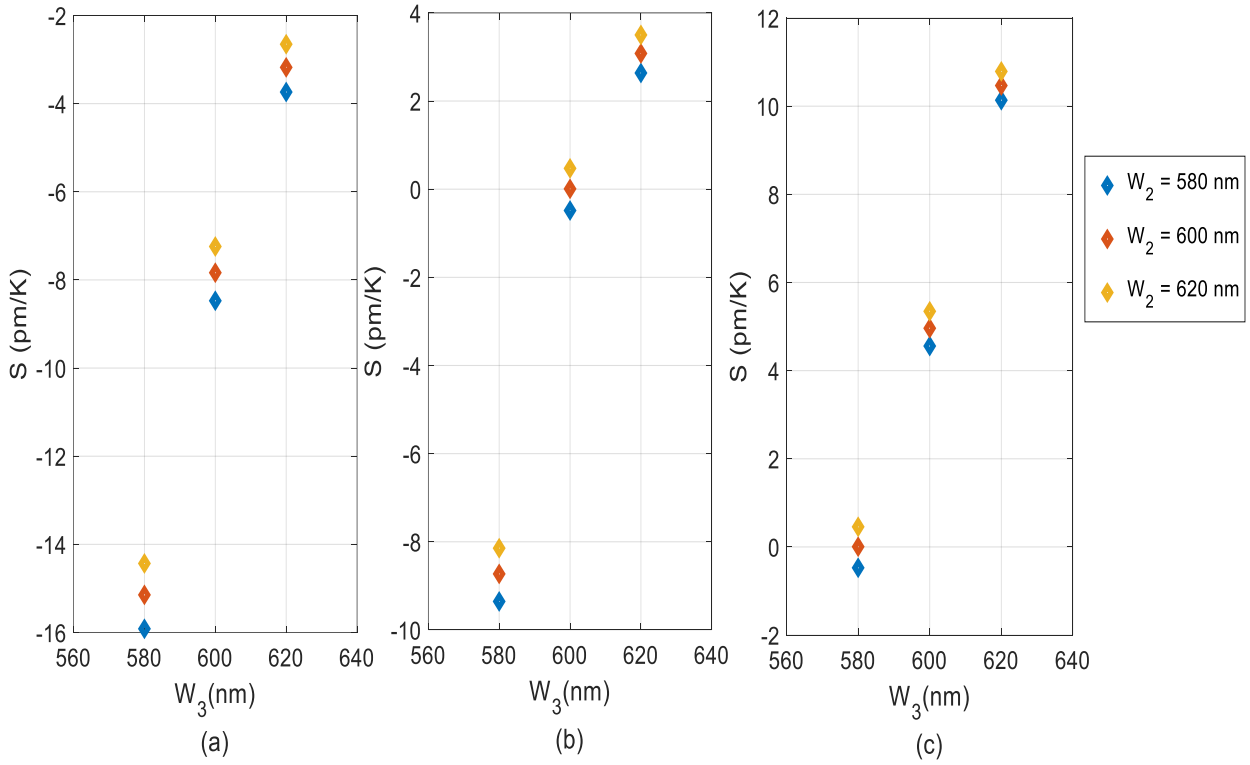

Figure 6.11: *Temperature sensitivity of the MZI at the central wavelength of 1550 nm as the function of the wire and SWG waveguide width and the SWG duty cycle: (a) 58%, (b) 60%, and (c) 62%.*

6.5 Bandwidth Enhancement Analyses and Discussion

As mentioned in section 6.3, the athermal MZI design was initially optimized for its footprint. However, if more stringent temperature insensitivity limits are required, for example to support applications in a bandwidth region (say, 1500 to 1600 nm), a tradeoff is required between r_{OPD} and S_{total}. Unlike solutions based on wire waveguides of different widths [39], [150], this tradeoff can be achieved by taking advantage of additional 'degrees of freedom' provided by SWG unique properties. This is illustrated in Figure 6.12, where the resulting S_{total} over a 100 nm range around 1550 nm is shown as a function of different waveguide parameters: the duty cycle DC between 40% and 60%, W_2 between 350 - 600 nm, and W_3 between 400 - 600 nm. By analyzing Figure 6.12, we found that a smaller waveguide width gives a lower temperature sensitivity of the MZI in the 1500 to 1600 nm wavelength range.

Figure 6.13 summarizes results related to the MZI temperature sensitivity (S_{total}) in the same 1500 to 1600 nm wavelength region when taking into account different waveguide dimensions and r_{OPD} values:

1. W_2 = 400 nm, W_3 = 400 nm, DC = 40%, L = 75.1 mm, and ΔL = 64.4 mm
2. W_2 = 600 nm, W_3 = 600 nm, DC = 60%, L = 50.6 mm, and ΔL = 23.5 mm
3. W_2 = 500 nm, W_3 = 500 nm, DC = 50%, L = 62 mm, and ΔL = 42.5 mm

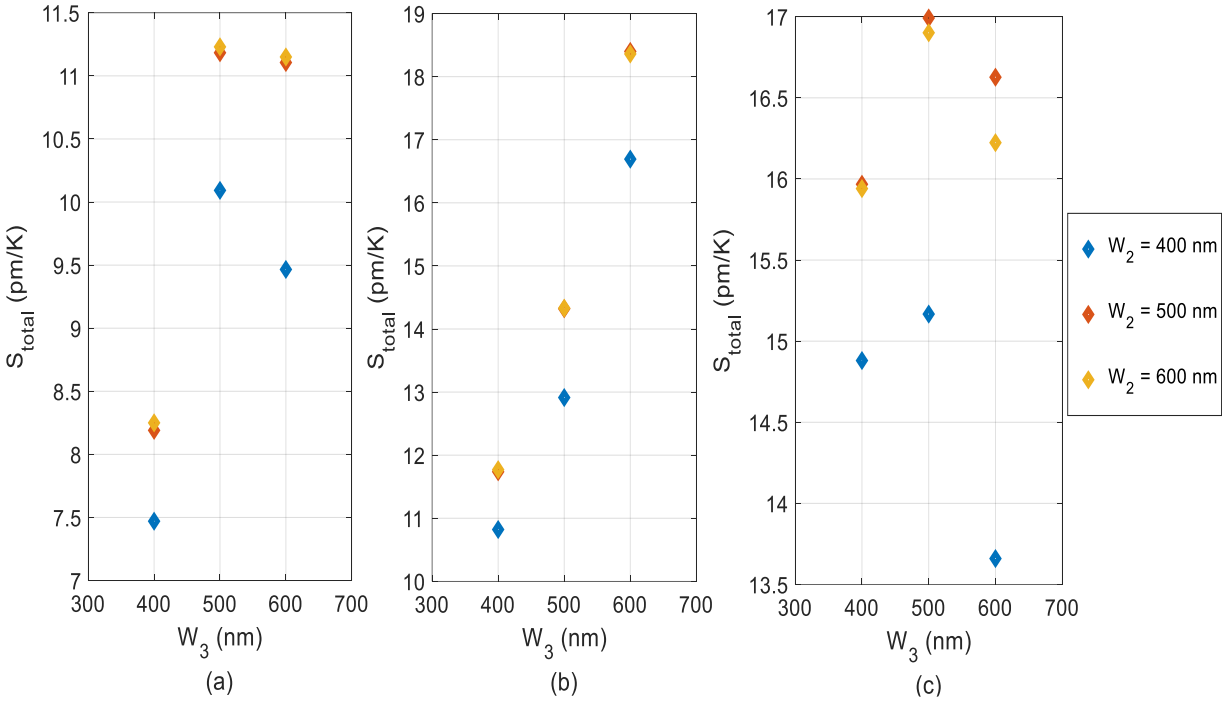

Figure 6.12: *Overall temperature sensitivity of the athermal MZI in the wavelength range of 1500 to 1600 nm when considering the wire waveguide and SWG waveguide width variations represented by duty cycle: (a) 40%, (b) 50%, and (c) 60%.*

We found that in order to achieve an athermal operation over the range of 100 nm around 1550 nm, one has to select a smaller width of the wire waveguide, and smaller width and DC of the SWG. For this reason, for the proposed athermal MZI design, we selected W_2 = 400 nm, W_3 = 400 nm, DC = 40%, L = 75.1 mm, and ΔL = 64.4 mm. By choosing these values, the S_{total} was found to be 7.5 pm/K. Just for a comparison, this value is less than a one-half of 16.4 pm/K found for the athermal MZI with parameters W_2 = 600 nm, W_3 = 600 nm, DC = 60%, L = 50.6 mm, ΔL = 23.5 mm.

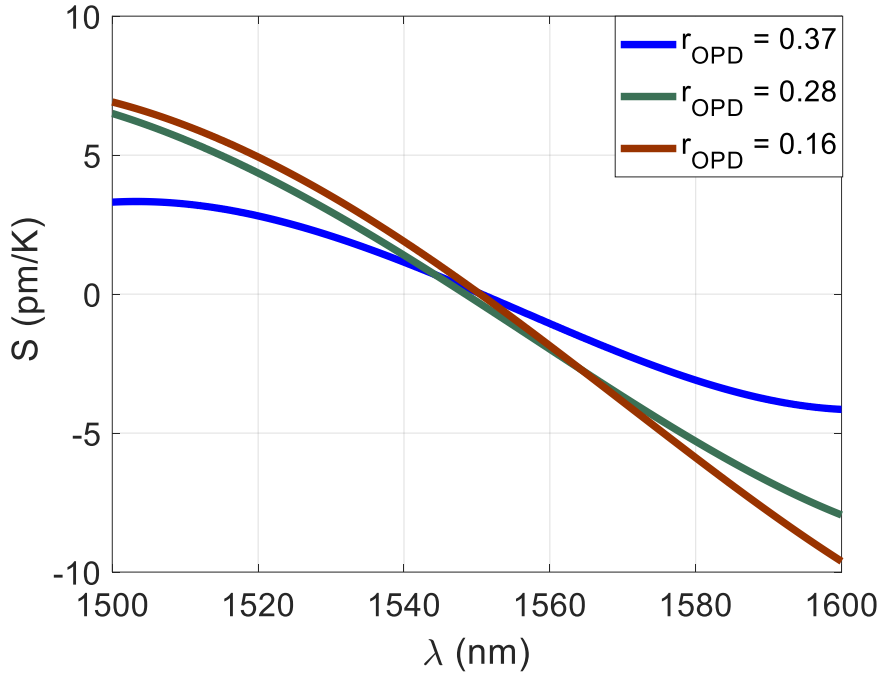

Figure 6.13: *Illustration of MZI temperature sensitivity in 1500 to 1600 nm wavelength region for relative optical path differences: r_{OPD} = 0.37 blue, r_{OPD} = 0.28 green and r_{OPD} = 0.16 brown.*

Figure 6.14 shows the required total length of the MZI ($L_{total} = L_1 + L_2 + 2 \times L$) in order to achieve its athermal operation modified interference order. The FSR of the MZI can be computed using equation (6.3). Calculations are based on equations (6.1), (6.2), (6.4), and waveguides dimensions considered earlier in this section i.e.:

1. W_2 = 400 nm, W_3 = 400 nm, DC = 40%
2. W_2 = 600 nm, W_3 = 600 nm, DC = 60%
3. W_2 = 500 nm, W_3 = 500 nm, DC = 50%

The study shows that the temperature insensitive MZI can be designing through a combination of SWG and wire waveguides with carefully tailored dimensions. Using the SWG waveguide adds an additional degree of freedom for controlling the SWG effective refractive index and dispersion through varying the SWG DC We found, that

the proposed athermal MZI design is insensitive to changes of the wire and SWG length L up to ± 0.355 mm and the design can be scaled for any targeted FSR.

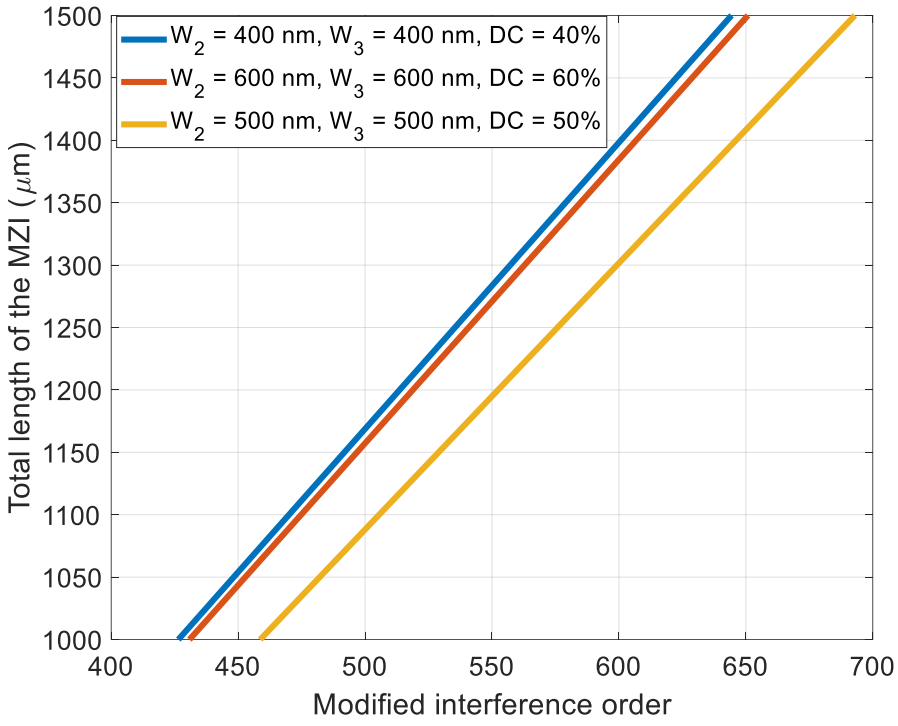

Figure 6.14: *Illustration of MZI length (L_{total}) as function of modified interference order (M) for different sets of waveguides dimensions: W_2 = 400 nm, W_3 = 400 nm, DC = 40% -blue line; W_2 = 600 nm, W_3 = 600 nm, DC = 60% -red line, and W_2 = 500 nm, W_3 = 500 nm, DC = 50% -yellow line.*

6.6 Summary

We have proposed and analyzed a silicon-on-insulator MZI with the minimal temperature sensitivity reported to date. The temperature compensation is achieved by tailoring SWG properties. Performance simulations show that by engineering waveguide dimensions, an overall temperature insensitivity below 7.5 pm/K can be attained in a 100 nm range around 1550 nm. The device is insensitive to changes of

the wire and SWG length L up to ± 0.355 mm. Errors due to optical path imbalance, their mitigation and the resilience of the athermal design to fabrication errors were then analyzed. We found that trade-offs could be made between the temperature sensitivity, optical path imbalance and fabrication errors by 'properly' selecting the SWG length, width, and duty cycle. The proposed athermal MZI design can be applied to part of interferometer arrays of on-chip Fourier-transform microspectrometers or for the application of nonlinear optical communication. This will enable a better scalability, wider FSR range and device ability to mitigate the challenging environmental influence. This approach sets a new milestone for achieving a better resolution stability in the field of integrated spectroscopy or nonlinear optical devices. A spiral waveguide design and reduction of δL will further help with minimizing the device footprint.

Chapter 7

Conclusion

A summary of all the theoretical evaluations, experiments and results given in this doctoral dissertation are herein described with links to future work.

7.1 Summary of key findings

This doctoral dissertation listed three major contributions in the field of Lightwave communication which are described below:

1. Picosecond pulsewidth measurement using highly nonlinear fiber and optical power meter:

A method has been presented for optical data carrier pulsewidth measurement which comprises a NOLM using highly nonlinear optical fiber, high power EDFA, and an optical power meter. This method is based on the assumption of the envelope of an optical pulse being of the form $sech^2$ or Gaussian and the internal structure of the method is slowly varying. The experimental results are verified by theoretical evaluation of the nonlinear Schrodinger equation for the self-phase and cross-phase modulation. The effect of counter propagation is also considered in the theoretical evaluation. Optical pulses in the range of 2 to 10 ps were successfully measured experimentally with a resolution of 0.25 ps. It has further been shown that the dynamic range of this method can be extended from 0.25 ps to 40 ps. Also, if the counter propagation effect is compensated using the compensation schemes [78], the dynamic range can be extended up to 100 ps using the same available hardware. The method may find its use in distributed networks or as a bolt-on to optical systems using ultra-short pulse sources.

2. On chip picosecond pulsewidth measurement using Nonlinear MZI and optical power meter:

The concept introduced in the first method described above has been applied to PIC. In this description, an on-chip method is presented for picosecond pulse width measurement which comprises a nonlinear MZI using an SOI platform, high power

EDFA and an optical power meter. The simulations for the pulse width measurement of optical pulses is shown separately for the self-phase and cross-phase modulation schemes by analytically solving the NLSE using the split step method. In contrary to highly nonlinear fiber (investigated in method 1), silicon has a strong TPA effect in C-band (1530 to 1560 nm), and therefore all the nonlinear losses - including TPA and TPA generated free carriers (i.e. FCA and FCD) are considered in the nonlinear simulations. The simulation results show that using this method, pulses from 01 to 09 ps can be measured. Due to strong TPA effects, the dynamic range of this method is limited. The dynamic range can be increased by using a material which has lower or negligible TPA effect in C band and is compatible to CMOS as well, such as silicon rich nitrite.

3. Athermal MZI based on SOI platform:

Since silicon has a strong thermo-optic coefficient, even a small change in the temperature can cause large deviations in the properties of the device including the nonlinear properties. In this finding, a novel design of temperature insensitive MZI device using SOI platform is presented. The MZI consists of the combination of an SWG and wire waveguide. The effective refractive index of the SWG waveguide has been computed by using band-structure computations in Lumerical FDTD solution. By modifying the properties of the SWG waveguide, i.e. duty cycle and width, the overall effect of temperature has been minimized. Simulations of the device show that the overall temperature sensitivity can be reduced by up to 7.5 pm/K over a bandwidth of 100 nm near 1550 nm. As such, the novel athermal device is insensitive to variations

in the length of both the SWG and wire waveguides, up to ± 0.355 mm. Device fabrication errors have also been considered in the simulation model. Furthermore, it has also been shown that this athermal device can be designed for the desired FSR.

7.2 Future research

The main focus of this dissertation is towards the usage of nonlinear property of Lightwave communication for measuring an optical data carrier pulsewidth in picosecond regime.

The possible extension of work can be to use the schemes in which the effect of counter-propagation can be mitigated, such as using polarization maintained-NOLM (PM-NOLM) proposed by [78]. The device dynamic range of all-fiber based NOLM setup is severely affected by the counter-propagation effects due to usage of very high repetition rate mode-locked laser. Therefore, if the effect of counter-propagation in NOLM is dynamically compensated, the range of the device can be improved significantly.

For the PIC, we have presented the simulations results of the nonlinear MZI based on SOI platform. The future task would be to perform the experiments for measuring the picosecond optical data carrier pulsewidth using the same nonlinear MZI based on SOI platform to validate the simulations results.

It can be analyzed from the simulations results that the dynamic range of the SOI based nonlinear MZI is limited by the nonlinear losses (i.e. TPA and free carriers). The range of this method can significantly be increased by using a material which has

lower nonlinear loss and is compatible to CMOS industry. Recently, it has been found that the silicon rich nitrite (SRN) can be used as a nonlinear medium due to its high nonlinear gain and negligible nonlinear losses at telecommunication wavelengths (i.e. 1550 nm). The nonlinear Kerr coefficient n_2 of SRN is 1.4×10^{-18} m^2/W [142], which is approximately three times lower than the silicon waveguide. It has also been found that the SNR has negligible nonlinear losses (i.e. $\beta_{TPA} = 0$) at the peak power level up to 55 W [143]. Hence by using this material, the range of the optical data carrier pulsewidth measurement device using SRN platform can be significantly increased.

In addition to the nonlinear investigation, the future task will be to fabricate the temperature insensitive MZI device using SWG waveguide (which is also based on SOI platform) and perform the experiments to validate the simulations results. The device footprint can be reduced by using spiral approach and compromising in the length insensitive parameter, i.e. δL.

References

[1] 'Cisco Visual Networking Index: Forecast and Trends, 2017–2022', *White Paper*, 2019.

[2] A. Amari, O. A. Dobre, R. Venkatesan, O. S. S. Kumar, P. Ciblat, and Y. Jaouen, 'A Survey on Fiber Nonlinearity Compensation for 400 Gb/s and Beyond Optical Communication Systems', *IEEE Commun. Surv. Tutorials*, vol. 19, no. 4, pp. 3097–3113, 2017.

[3] 'Cisco visual networking index: Forecast and methodology, 2015–2020', *White Paper*, 2015.

[4] G. P. Agrawal, *Fiber-Optic Communication Systems*. Wiley, 2010.

[5] H. Elgala, R. Mesleh, and H. Haas, 'Indoor optical wireless communication: potential and state-of-the-art', *IEEE Commun. Mag.*, vol. 49, no. 9, pp. 56–62, Sep. 2011.

[6] H. Lee, S. H. Lee, T. Q. S. Quek, and I. Lee, 'Deep Learning Framework for Wireless Systems: Applications to Optical Wireless Communications', *IEEE Commun. Mag.*, vol. 57, no. 3, pp. 35–41, Mar. 2019.

[7] F. Nadeem, V. Kvicera, M. Awan, E. Leitgeb, S. Muhammad, and G. Kandus, 'Weather effects on hybrid FSO/RF communication link', *IEEE J. Sel. Areas Commun.*, vol. 27, no. 9, pp. 1687–1697, Dec. 2009.

[8] D. R. Kolev, K. Wakamori, and M. Matsumoto, 'Transmission Analysis of OFDM-Based Services Over Line-of-Sight Indoor Infrared Laser Wireless Links', *J. Light. Technol.*, vol. 30, no. 23, pp. 3727–3735, Dec. 2012.

[9] M. B. Rahaim and T. D. C. Little, 'Toward practical integration of dual-use VLC within 5G networks', *IEEE Wirel. Commun.*, vol. 22, no. 4, pp. 97–103, Aug. 2015.

[10] L. Feng, R. Q. Hu, J. Wang, P. Xu, and Y. Qian, 'Applying VLC in 5G Networks: Architectures and Key Technologies', *IEEE Netw.*, vol. 30, no. 6, pp. 77–83, Nov. 2016.

[11] H. Haas, L. Yin, Y. Wang, and C. Chen, 'What is LiFi?', *J. Light. Technol.*, vol. 34, no. 6, pp. 1533–1544, Mar. 2016.

[12] H. Burchardt, N. Serafimovski, D. Tsonev, S. Videv, and H. Haas, 'VLC: Beyond point-to-point communication', *IEEE Commun. Mag.*, vol. 52, no. 7, pp. 98–105, Jul. 2014.

[13] M. A. Khalighi and M. Uysal, 'Survey on Free Space Optical Communication: A Communication Theory Perspective', *IEEE Commun. Surv. Tutorials*, vol. 16, no. 4, pp. 2231–2258, 2014.

[14] U. A. Korai, L. Luini, R. Nebuloni, and I. Glesk, 'Statistics of attenuation due to rain affecting hybrid FSO/RF link: Application for 5G networks', in *2017 11th European Conference on Antennas and Propagation (EUCAP)*, 2017, pp. 1789–1792.

[15] S. Bloom, E. Korevaar, J. Schuster, and H. Willebrand, 'Understanding the performance of free-space optics [Invited]', *J. Opt. Netw.*, vol. 2, no. 6, p. 178, Jun. 2003.

[16] J. P. da Silva, D. S. Bezerra, V. F. Rodriguez-Esquerre, I. E. da Fonseca, and H. E. Hernandez-Figueroa, 'Ge-Doped Defect-Core Microstructured Fiber Design by Genetic Algorithm for Residual Dispersion Compensation', *IEEE Photonics Technol. Lett.*, vol. 22, no. 18, pp. 1337–1339, Sep. 2010.

[17] M. F. Ferreira, *Nonlinear Effects in Optical Fibers*. Wiley, 2011.

[18] G. P. Agrawal, 'Nonlinear fiber optics: its history and recent progress [Invited]', *J. Opt. Soc. Am. B*, vol. 28, no. 12, p. A1, Dec. 2011.

[19] A. Barrias, J. Casas, and S. Villalba, 'A Review of Distributed Optical Fiber Sensors for Civil Engineering Applications', *Sensors*, vol. 16, no. 5, p. 748, May 2016.

[20] K. Kurosawa, 'Development of fiber-optic current sensing technique and its applications in electric power systems', *Photonic Sensors*, vol. 4, no. 1, pp. 12–20, Mar. 2014.

[21] J. Bland-Hawthorn *et al.*, 'Hexabundles: imaging fiber arrays for low-light astronomical applications', *Opt. Express*, vol. 19, no. 3, p. 2649, Jan. 2011.

[22] D. Marpaung, J. Yao, and J. Capmany, 'Integrated microwave photonics', *Nat. Photonics*, vol. 13, no. 2, pp. 80–90, Feb. 2019.

[23] P. Dong, 'Silicon Photonic Integrated Circuits for Wavelength-Division Multiplexing Applications', *IEEE J. Sel. Top. Quantum Electron.*, vol. 22, no. 6, pp. 370–378, Nov. 2016.

[24] L. Chang, Y. Li, N. Volet, L. Wang, J. Peters, and J. E. Bowers, 'Thin film wavelength converters for photonic integrated circuits', *Optica*, vol. 3, no. 5, p. 531, May 2016.

[25] A. D. Neira, G. A. Wurtz, and A. V. Zayats, 'All-optical switching in silicon photonic waveguides with an epsilon-near-zero resonant cavity [Invited]', *Photonics Res.*, vol. 6, no. 5, p. B1, May 2018.

[26] P. Dong *et al.*, 'Four-Channel 100-Gb/s Per Channel Discrete Multitone Modulation Using Silicon Photonic Integrated Circuits', *J. Light. Technol.*, vol. 34, no. 1, pp. 79–84, Jan. 2016.

[27] Po Dong, Xiang Liu, S. Chandrasekhar, L. L. Buhl, R. Aroca, and Young-Kai Chen, 'Monolithic Silicon Photonic Integrated Circuits for Compact 100<formula formulatype="inline"><tex Notation="TeX"> $^{+}$</tex></formula>Gb/s Coherent Optical Receivers and Transmitters', *IEEE J. Sel. Top. Quantum Electron.*, vol. 20, no. 4, pp. 150–157, Jul. 2014.

[28] G. Kim *et al.*, 'Low-voltage high-performance silicon photonic devices and photonic integrated circuits operating up to 30 Gb/s', *Opt. Express*, vol. 19, no. 27, p. 26936, Dec. 2011.

[29] G. Carpintero *et al.*, 'Microwave Photonic Integrated Circuits for Millimeter-Wave Wireless Communications', *J. Light. Technol.*, vol. 32, no. 20, pp. 3495–3501, Oct. 2014.

[30] A. Biberman, S. Manipatruni, N. Ophir, L. Chen, M. Lipson, and K. Bergman, 'First demonstration of long-haul transmission using silicon microring modulators', *Opt. Express*, vol. 18, no. 15, p. 15544, Jul. 2010.

[31] S. Xiao, M. H. Khan, H. Shen, and M. Qi, 'Compact silicon microring resonators with ultra-low propagation loss in the C band', *Opt. Express*, vol. 15, no. 22, p. 14467, 2007.

[32] K. M. De Vos, I. Bartolozzi, P. Bienstman, R. Baets, and E. Schacht, 'Optical biosensor based on silicon-on-insulator microring cavities for specific protein binding detection', 2007, p. 64470K.

[33] J. L. O'Brien, G. J. Pryde, A. G. White, T. C. Ralph, and D. Branning, 'Demonstration of an all-optical quantum controlled-NOT gate', *Nature*, vol. 426, no. 6964, pp. 264–267, Nov. 2003.

[34] J. W. Silverstone *et al.*, 'On-chip quantum interference between silicon photon-pair sources', *Nat. Photonics*, vol. 8, no. 2, pp. 104–108, Feb. 2014.

[35] A. Politi, J. Matthews, M. G. Thompson, and J. L. O'Brien, 'Integrated Quantum Photonics', *IEEE J. Sel. Top. Quantum Electron.*, vol. 15, no. 6, pp. 1673–1684, 2009.

[36] G. Cocorullo and I. Rendina, 'Thermo-optical modulation at 1.5μm in silicon etalon', *Electron. Lett.*, vol. 28, no. 1, pp. 83–85, Jan. 1992.

[37] S. Manipatruni *et al.*, 'Wide temperature range operation of micrometer-scale silicon electro-optic modulators', *Opt. Lett.*, vol. 33, no. 19, p. 2185, Oct. 2008.

[38] J. Teng *et al.*, 'Athermal Silicon-on-insulator ring resonators by overlaying a polymer cladding on narrowed waveguides', *Opt. Express*, vol. 17, no. 17, p. 14627, Aug. 2009.

[39] B. Guha, A. Gondarenko, and M. Lipson, 'Minimizing temperature sensitivity of silicon Mach-Zehnder interferometers', *Opt. Express*, vol. 18, no. 3, p. 1879, Feb. 2010.

[40] P. Cheben, R. Halir, J. H. Schmid, H. A. Atwater, and D. R. Smith, 'Subwavelength integrated photonics', *Nature*, vol. 560, no. 7720, pp. 565–572, Aug. 2018.

[41] G. P. Agrawal, *Nonlinear Fiber Optics*. 2007.

[42] P Diament, *Wave Transmission and Fiber Optics*. 1990.

[43] M. M. Fejer, G. A. Magel, D. H. Jundt, and R. L. Byer, 'Quasi-phase-matched second harmonic generation: tuning and tolerances', *IEEE J. Quantum Electron.*, vol. 28, no. 11, pp. 2631–2654, 1992.

[44] Q. Lin, O. J. Painter, and G. P. Agrawal, 'Nonlinear optical phenomena in silicon waveguides: modeling and applications', *Opt. Express*, vol. 15, no. 25, p. 16604, 2007.

[45] L. Chrostowski and M. Hochberg, *Silicon Photonics Design*. Cambridge: Cambridge University Press, 2015.

[46] O. V. Sinkin, R. Holzlohner, J. Zweck, and C. R. Menyuk, 'Optimization of the split-step fourier method in modeling optical-fiber communications systems', *J. Light. Technol.*, vol. 21, no. 1, pp. 61–68, Jan. 2003.

[47] C. Antonelli, M. Shtaif, and A. Mecozzi, 'Modeling of Nonlinear Propagation in Space-Division Multiplexed Fiber-Optic Transmission', *J. Light. Technol.*, vol. 34, no. 1, pp. 36–54, Jan. 2016.

[48] S. Shaklan and F. Roddier, 'Coupling starlight into single-mode fiber optics', *Appl. Opt.*, vol. 27, no. 11, p. 2334, Jun. 1988.

[49] 'http://www.lumerical.com/mode.php.' .

[50] G. Keiser, 'Optical Fiber Communications', in *Wiley Encyclopedia of Telecommunications*, Hoboken, NJ, USA: John Wiley & Sons, Inc., 2003.

[51] G. P. Agrawal, *Fiber-Optic Communication Systems*. Hoboken, NJ, USA: John Wiley & Sons, Inc., 2010.

[52] A. Blanco-Redondo, C. M. de Sterke, J. E. Sipe, T. F. Krauss, B. J. Eggleton, and C. Husko, 'Pure-quartic solitons', *Nat. Commun.*, vol. 7, no. 1, p. 10427, Apr. 2016.

[53] 'https://www.corning.com/media/worldwide/coc/documents/Fiber/SMF-28%20Ultra.pdf'. .

[54] G. P. Agrawal and N. A. Olsson, 'Self-phase modulation and spectral broadening of optical pulses in semiconductor laser amplifiers', *IEEE J. Quantum Electron.*, vol. 25, no. 11, pp. 2297–2306, 1989.

[55] E. C. Mägi, L. B. Fu, H. C. Nguyen, M. R. Lamont, D. I. Yeom, and B. J. Eggleton, 'Enhanced Kerr nonlinearity in sub-wavelength diameter As_2Se_3 chalcogenide fiber tapers', *Opt. Express*, vol. 15, no. 16, p. 10324, 2007.

[56] F. M. Knox, W. Forysiak, and N. J. Doran, '10-Gbt/s soliton communication systems over standard fiber at 1.55 μm and the use of dispersion compensation', *J. Light. Technol.*, vol. 13, no. 10, pp. 1955–1962, 1995.

[57] M. Suzuki, N. Edagawa, H. Taga, H. Tanaka, S. Yamamoto, and S. Akiba, '10 Gb/s, over 12200 km soliton data transmission with alternating-amplitude solitons', *IEEE Photonics Technol. Lett.*, vol. 6, no. 6, pp. 757–759, Jun. 1994.

[58] S. Watanabe *et al.*, 'Wavelength conversion using fiber cross-phase modulation driven by two pump waves', *Opt. Express*, vol. 27, no. 12, p. 16767, Jun. 2019.

[59] G. Roelkens *et al.*, 'Silicon-Based Photonic Integration Beyond the Telecommunication Wavelength Range', *IEEE J. Sel. Top. Quantum Electron.*, vol. 20, no. 4, pp. 394–404, Jul. 2014.

[60] W. Zhong, M. Wu, C.-W. Chang, K. A. Merrick, S. D. Merajver, and M.-A. Mycek, 'Picosecond-resolution fluorescence lifetime imaging microscopy: a useful tool for sensing molecular interactions in vivo via FRET', *Opt. Express*, vol. 15, no. 26, p. 18220, 2007.

[61] R. Trebino and D. J. Kane, 'Using phase retrieval to measure the intensity and phase of ultrashort pulses: frequency-resolved optical gating', *J. Opt. Soc. Am. A*, vol. 10, no. 5, p. 1101, May 1993.

[62] R. Trebino, *Frequency-Resolved Optical Gating: The Measurement of Ultrashort Laser Pulses*. Boston, MA: Springer US, 2000.

[63] D. J. Kane, 'Real-time measurement of ultrashort laser pulses using principal component generalized projections', *IEEE J. Sel. Top. Quantum Electron.*, vol. 4, no. 2, pp. 278–284, 1998.

[64] C. Iaconis and I. A. Walmsley, 'Spectral phase interferometry for direct electric-field reconstruction of ultrashort optical pulses', *Opt. Lett.*, vol. 23, no. 10, p. 792, May 1998.

[65] S. P. Gorza, P. Wasylczyk, and I. A. Walmsley, 'Spectral shearing interferometry with spatially chirped replicas for measuring ultrashort pulses', *Opt. Express*, vol. 15, no. 23, p. 15168, 2007.

[66] T. Hori, N. Nishizawa, T. Goto, and M. Yoshida, 'Experimental and numerical analysis of widely broadened supercontinuum generation in highly nonlinear dispersion-shifted fiber with a femtosecond pulse', *J. Opt. Soc. Am. B*, vol. 21, no. 11, p. 1969, Nov. 2004.

[67] I. G. Cormack, W. Sibbett, and D. T. Reid, 'Rapid measurement of ultrashort-pulse amplitude and phase from a two-photon absorption sonogram trace', *J. Opt. Soc. Am. B*, vol. 18, no. 9, p. 1377, Sep. 2001.

[68] M. D. Thomson, J. M. Dudley, L. P. Barry, and J. D. Harvey, 'Complete pulse characterization at 15 μm by cross-phase modulation in optical fibers', *Opt. Lett.*, vol. 23, no. 20, p. 1582, Oct. 1998.

[69] P.-A. Lacourt, M. Hanna, and J. M. Dudley, 'Broad-band and ultrasensitive pulse characterization using frequency-resolved optical gating via four-wave mixing in a semiconductor optical amplifier', *IEEE Photonics Technol. Lett.*, vol. 17, no. 1, pp. 157–159, Jan. 2005.

[70] L. Lepetit, G. Chériaux, and M. Joffre, 'Linear techniques of phase measurement by femtosecond spectral interferometry for applications in spectroscopy', *J. Opt. Soc. Am. B*, vol. 12, no. 12, p. 2467, Dec. 1995.

[71] C. Dorrer and I. Kang, ‘Linear self-referencing techniques for short-optical-pulse characterization [Invited]’, *J. Opt. Soc. Am. B*, vol. 25, no. 6, p. A1, Jun. 2008.

[72] F. Li, Y. Park, and J. Azana, ‘Linear Characterization of Optical Pulses With Durations Ranging From the Picosecond to the Nanosecond Regime Using Ultrafast Photonic Differentiation’, *J. Light. Technol.*, vol. 27, no. 21, pp. 4623–4633, Nov. 2009.

[73] M. A. Foster, R. Salem, D. F. Geraghty, A. C. Turner-Foster, M. Lipson, and A. L. Gaeta, ‘Silicon-chip-based ultrafast optical oscilloscope’, *Nature*, vol. 456, no. 7218, pp. 81–84, Nov. 2008.

[74] A. Pasquazi *et al.*, ‘Sub-picosecond phase-sensitive optical pulse characterization on a chip’, *Nat. Photonics*, vol. 5, no. 10, pp. 618–623, Oct. 2011.

[75] J.-Y. Yang, L. Zhang, X. Wu, O. F. Yilmaz, B. Zhang, and A. E. Willner, ‘All-Optical Chromatic Dispersion Monitoring for Phase-Modulated Signals Utilizing Cross-Phase Modulation in a Highly Nonlinear Fiber’, *IEEE Photonics Technol. Lett.*, vol. 20, no. 19, pp. 1642–1644, Oct. 2008.

[76] N. J. Doran and D. Wood, ‘Nonlinear-optical loop mirror’, *Opt. Lett.*, vol. 13, no. 1, p. 56, Jan. 1988.

[77] L. Poti, E. Lazzeri, G. Meloni, A. Bogoni, and G. Prati, ‘All-Optical Processing by Means of Cross-Phase-Modulation-Based PM-NOLM Interconnected Structures’, *IEEE J. Sel. Top. Quantum Electron.*, vol. 14, no. 3, pp. 580–586, 2008.

[78] Y. Miyoshi, S. Takagi, S. Namiki, and K.-I. Kitayama, ‘Multiperiod PM-NOLM With Dynamic Counter-Propagating Effects Compensation for 5-Bit All-Optical Analog-to-Digital Conversion and Its Performance Evaluations’, *J. Light. Technol.*, vol. 28, no. 4, pp. 415–422, Feb. 2010.

[79] J. Leuthold, C. Koos, and W. Freude, ‘Nonlinear silicon photonics’, *Nat. Photonics*, vol. 4, no. 8, pp. 535–544, Aug. 2010.

[80] T. D. Ladd, F. Jelezko, R. Laflamme, Y. Nakamura, C. Monroe, and J. L. O’Brien, ‘Quantum computers’, *Nature*, vol. 464, no. 7285, pp. 45–53, Mar. 2010.

[81] M. A. Broome *et al.*, ‘Photonic Boson Sampling in a Tunable Circuit’, *Science (80-.).*, vol. 339, no. 6121, pp. 794–798, Feb. 2013.

[82] G. D. Marshall *et al.*, ‘Laser written waveguide photonic quantum circuits’, *Opt. Express*, vol. 17, no. 15, p. 12546, Jul. 2009.

[83] R. Soref, ‘Mid-infrared photonics in silicon and germanium’, *Nat. Photonics*, vol. 4, no. 8, pp. 495–497, Aug. 2010.

[84] B. Jalali, ‘Nonlinear optics in the mid-infrared’, *Nat. Photonics*, vol. 4, no. 8, pp. 506–508, Aug. 2010.

[85] C. Lacava, M. J. Strain, P. Minzioni, I. Cristiani, and M. Sorel, ‘Integrated nonlinear Mach Zehnder for 40 Gbit/s all-optical switching’, *Opt. Express*, vol. 21, no. 18, p. 21587, Sep. 2013.

[86] B. Jalali and S. Fathpour, ‘Silicon Photonics’, *J. Light. Technol.*, vol. 24, no. 12, pp. 4600–4615, Dec. 2006.

[87] B. Jalali, S. Yegnanarayanan, T. Yoon, T. Yoshimoto, I. Rendina, and F. Coppinger, ‘Advances in silicon-on-insulator optoelectronics’, *IEEE J. Sel. Top. Quantum Electron.*, vol. 4, no. 6, pp. 938–947, 1998.

[88] B. Jalali, S. Yegnanarayanan, T. Yoon, T. Yoshimoto, I. Rendina, and F. Coppinger, ‘Advances in silicon-on-insulator optoelectronics’, *IEEE J. Sel. Top. Quantum Electron.*, vol. 4, no. 6, pp. 938–947, 1998.

[89] M. Burla, L. R. Cortés, M. Li, X. Wang, L. Chrostowski, and J. Azaña, 'Integrated waveguide Bragg gratings for microwave photonics signal processing', *Opt. Express*, vol. 21, no. 21, p. 25120, Oct. 2013.

[90] W. Shi *et al.*, 'Silicon photonic grating-assisted, contra-directional couplers', *Opt. Express*, vol. 21, no. 3, p. 3633, Feb. 2013.

[91] B. Jalali, S. Yegnanarayanan, and P. D. Trinh, 'Integrated optical directional couplers in silicon-on-insulator', *Electron. Lett.*, vol. 31, no. 24, pp. 2097–2098, Nov. 1995.

[92] K. Yamada, 'Silicon Photonic Wire Waveguides: Fundamentals and Applications', 2011, pp. 1–29.

[93] Y. Zhang *et al.*, 'A compact and low loss Y-junction for submicron silicon waveguide', *Opt. Express*, vol. 21, no. 1, p. 1310, Jan. 2013.

[94] H. Chen and A. W. Poon, 'Low-Loss Multimode-Interference-Based Crossings for Silicon Wire Waveguides', *IEEE Photonics Technol. Lett.*, vol. 18, no. 21, pp. 2260–2262, Nov. 2006.

[95] Y. Zhang, Z. Li, and B. Li, 'Multimode interference effect and self-imaging principle in two-dimensional silicon photonic crystal waveguides for terahertz waves', *Opt. Express*, vol. 14, no. 7, p. 2679, 2006.

[96] P. D. Trinh, S. Yegnanarayanan, F. Coppinger, and B. Jalali, 'Silicon-on-insulator (SOI) phased-array wavelength multi/demultiplexer with extremely low-polarization sensitivity', *IEEE Photonics Technol. Lett.*, vol. 9, no. 7, pp. 940–942, Jul. 1997.

[97] P. D. Trinh, S. Yegnanarayanan, and B. Jalali, '5 x 9 integrated optical star coupler in silicon-on-insulator technology', *IEEE Photonics Technol. Lett.*, vol. 8, no. 6, pp. 794–796, Jun. 1996.

[98] F. Horst, W. M. J. Green, S. Assefa, S. M. Shank, Y. A. Vlasov, and B. J. Offrein, 'Cascaded Mach-Zehnder wavelength filters in silicon photonics for low loss and flat pass-band WDM (de-)multiplexing', *Opt. Express*, vol. 21, no. 10, p. 11652, May 2013.

[99] S. Cheung, Tiehui Su, K. Okamoto, and S. J. B. Yoo, 'Ultra-Compact Silicon Photonic 512 × 512 25 GHz Arrayed Waveguide Grating Router', *IEEE J. Sel. Top. Quantum Electron.*, vol. 20, no. 4, pp. 310–316, Jul. 2014.

[100] K. Yamada *et al.*, 'High-performance silicon photonics technology for telecommunications applications', *Sci. Technol. Adv. Mater.*, vol. 15, no. 2, p. 024603, Apr. 2014.

[101] R. Soref and B. Bennett, 'Electrooptical effects in silicon', *IEEE J. Quantum Electron.*, vol. 23, no. 1, pp. 123–129, Jan. 1987.

[102] C. K. Tang and G. T. Reed, 'Highly efficient optical phase modulator in SOI waveguides', *Electron. Lett.*, vol. 31, no. 6, pp. 451–452, Mar. 1995.

[103] Q. Xu, B. Schmidt, S. Pradhan, and M. Lipson, 'Micrometre-scale silicon electro-optic modulator', *Nature*, vol. 435, no. 7040, pp. 325–327, May 2005.

[104] A. Liu *et al.*, 'A high-speed silicon optical modulator based on a metal–oxide–semiconductor capacitor', *Nature*, vol. 427, no. 6975, pp. 615–618, Feb. 2004.

[105] G. T. Reed, G. Mashanovich, F. Y. Gardes, and D. J. Thomson, 'Silicon optical modulators', *Nat. Photonics*, vol. 4, no. 8, pp. 518–526, Aug. 2010.

[106] E. Dulkeith, F. Xia, L. Schares, W. M. J. Green, and Y. A. Vlasov, 'Group index and group velocity dispersion in silicon-on-insulator photonic wires', *Opt. Express*, vol. 14, no. 9, p. 3853, 2006.

[107] W. H. Reeves *et al.*, 'Transformation and control of ultra-short pulses in dispersion-engineered photonic crystal fibres', *Nature*, vol. 424, no. 6948, pp. 511–515, Jul. 2003.

[108] G. P. Agrawal, *Lightwave Technology: Components and Devices*. Wiley, 2004.

[109] S. Trillo, E. M. Wright, G. I. Stegeman, and S. Wabnitz, 'Soliton switching in fiber nonlinear directional couplers', *Opt. Lett.*, vol. 13, no. 8, p. 672, Aug. 1988.

[110] J. S. Aitchison, G. I. Stegeman, and J. U. Kang, 'All-optical multiplexing of femtosecond signals using an AlGaAs nonlinear directional coupler', *Electron. Lett.*, vol. 31, no. 2, pp. 118–119, Jan. 1995.

[111] J. S. Aitchison, A. Villeneuve, and G. I. Stegeman, 'All-optical switching in two cascaded nonlinear directional couplers', *Opt. Lett.*, vol. 20, no. 7, p. 698, Apr. 1995.

[112] A. K. Sarma, 'Silicon waveguide based nonlinear directional coupler as a soliton switch', *Opt. Eng.*, vol. 47, no. 12, p. 120503, Dec. 2008.

[113] W. Bogaerts *et al.*, 'Silicon microring resonators', *Laser Photon. Rev.*, vol. 6, no. 1, pp. 47–73, Jan. 2012.

[114] Q. Xu, D. Fattal, and R. G. Beausoleil, 'Silicon microring resonators with 1.5-μm radius', *Opt. Express*, vol. 16, no. 6, p. 4309, Mar. 2008.

[115] A. C. Turner, M. A. Foster, A. L. Gaeta, and M. Lipson, 'Ultra-low power parametric frequency conversion in a silicon microring resonator', *Opt. Express*, vol. 16, no. 7, p. 4881, Mar. 2008.

[116] M. Ferrera *et al.*, 'Low-power continuous-wave nonlinear optics in doped silica glass integrated waveguide structures', *Nat. Photonics*, vol. 2, no. 12, pp. 737–740, Dec. 2008.

[117] C.-H. Yeh, H.-Y. Cheng, Y.-C. Chang, C.-W. Chow, and J.-H. Chen, 'Silicon-Micro-Ring Resonator-Based Erbium Fiber Laser With Single-Longitudinal-Mode Oscillation', *IEEE Photonics J.*, vol. 10, no. 3, pp. 1–7, Jun. 2018.

[118] T. Nurmohammadi, K. Abbasian, and R. Yadipour, 'Ultra-fast all-optical plasmonic switching in near infra-red spectrum using a Kerr nonlinear ring resonator', *Opt. Commun.*, vol. 410, pp. 142–147, Mar. 2018.

[119] I. Glesk, P. J. Bock, P. Cheben, J. H. Schmid, J. Lapointe, and S. Janz, 'All-optical switching using nonlinear subwavelength Mach-Zehnder on silicon', *Opt. Express*, vol. 19, no. 15, p. 14031, Jul. 2011.

[120] A. Bahrami, A. Rostami, and F. Nazari, 'MZ-MMI-based all-optical switch using nonlinear coupled waveguides', *Optik (Stuttg).*, vol. 122, no. 20, pp. 1787–1790, Oct. 2011.

[121] I. Glesk, P. J. Bock, P. Cheben, J. H. Schmid, J. Lapointe, and S. Janz, 'Picosecond all-optical switching using nonlinear Mach–Zehnder with silicon subwavelength grating and photonic wire arms', *Opt. Quantum Electron.*, vol. 44, no. 12–13, pp. 613–621, Oct. 2012.

[122] J.-W. Wu, H.-S. Lee, and E.-H. Lee, 'All-optical 40Gb/s wavelength conversion using hybrid SOI-based MZI and SOAs configuration', *Opt. Commun.*, vol. 284, no. 16–17, pp. 4000–4006, Aug. 2011.

[123] F. Gomez-Agis *et al.*, 'All-optical wavelength conversion at 160 Gbit/s using SOA and silicon-on-insulator photonic circuit', *Electron. Lett.*, vol. 45, no. 22, p. 1132, 2009.

[124] V. J. Urick, J. F. Diehl, J. D. McKinney, J. M. Singley, and C. E. Sunderman, 'Nonlinear Optical Angle Modulation for Suppression of RF Interference', *IEEE Trans. Microw. Theory Tech.*, vol. 64, no. 7, pp. 2198–2204, Jul. 2016.

[125] E. Timurdogan, C. V. Poulton, M. J. Byrd, and M. R. Watts, 'Electric field-induced second-order nonlinear optical effects in silicon waveguides', *Nat. Photonics*, vol. 11, no. 3, pp. 200–206, Mar. 2017.

[126] B. P. Nelson *et al.*, 'All-optical Gbit/s switching using nonlinear optical loop mirror', *Electron. Lett.*, vol. 27, no. 9, p. 704, 1991.

[127] Q. Hao, Q. Zhang, F. Chen, K. Yang, and H. Zeng, 'All-Optical 20-μHz-Level Repetition Rate Stabilization of Mode Locking With a Nonlinear Amplifying Loop Mirror', *J. Light. Technol.*, vol. 34, no. 11, pp. 2833–2837, Jun. 2016.

[128] U. A. Korai, Z. Wang, C. Lacava, L. R. Chen, I. Glesk, and M. J. Strain, 'Technique for the measurement of picosecond optical pulses using a non-linear fiber loop mirror and an optical power meter', *Opt. Express*, vol. 27, no. 5, p. 6377, Mar. 2019.

[129] Z. Wang, I. Glesk, and L. R. Chen, 'An integrated nonlinear optical loop mirror in silicon photonics for all-optical signal processing', *APL Photonics*, vol. 3, no. 2, p. 026102, Feb. 2018.

[130] T. Gottschall, T. Meyer, M. Schmitt, J. Popp, J. Limpert, and A. Tünnermann, 'Four-wave-mixing-based optical parametric oscillator delivering energetic, tunable, chirped femtosecond pulses for non-linear biomedical applications', *Opt. Express*, vol. 23, no. 18, p. 23968, Sep. 2015.

[131] A. Mena-Contla *et al.*, 'Extreme nonlinear waves in external gravitational-like potentials: Possible applications for the optical soliton supercontinuum generation and the ocean coast line protection', *Optik (Stuttg).*, vol. 161, pp. 187–195, May 2018.

[132] P. Jaworski, F. Yu, R. M. Carter, J. C. Knight, J. D. Shephard, and D. P. Hand, 'High energy green nanosecond and picosecond pulse delivery through a negative curvature fiber for precision micro-machining', *Opt. Express*, vol. 23, no. 7, p. 8498, Apr. 2015.

[133] H. Aggrawal, P. Chen, M. M. Assefzadeh, B. Jamali, and A. Babakhani, 'Gone in a Picosecond: Techniques for the Generation and Detection of Picosecond Pulses and Their Applications', *IEEE Microw. Mag.*, vol. 17, no. 12, pp. 24–38, Dec. 2016.

[134] M. S. Ahmed, M. S. K. Abuhelala, and I. Glesk, 'Managing Dispersion-Affected OCDMA Auto-Correlation Based on PS Multiwavelength Code Carriers Using SOA', *J. Opt. Commun. Netw.*, vol. 9, no. 8, p. 693, Aug. 2017.

[135] R. A. Soref, S. J. Emelett, and W. R. Buchwald, 'Silicon waveguided components for the long-wave infrared region', *J. Opt. A Pure Appl. Opt.*, vol. 8, no. 10, pp. 840–848, Oct. 2006.

[136] M. Dinu, F. Quochi, and H. Garcia, 'Third-order nonlinearities in silicon at telecom wavelengths', *Appl. Phys. Lett.*, vol. 82, no. 18, pp. 2954–2956, May 2003.

[137] I. A. Walmsley and C. Dorrer, 'Characterization of ultrashort electromagnetic pulses', *Adv. Opt. Photonics*, vol. 1, no. 2, p. 308, Apr. 2009.

[138] C. Monat *et al.*, 'Integrated optical auto-correlator based on third-harmonic generation in a silicon photonic crystal waveguide', *Nat. Commun.*, vol. 5, no. 1, p. 3246, May 2014.

[139] S. Kinugasa, N. Ishikura, H. Ito, N. Yazawa, and T. Baba, 'One-chip integration of optical correlator based on slow-light devices', *Opt. Express*, vol. 23, no. 16, p. 20767, Aug. 2015.

[140] I. D. Rukhlenko, M. Premaratne, and G. P. Agrawal, 'Nonlinear Silicon Photonics: Analytical Tools', *IEEE J. Sel. Top. Quantum Electron.*, vol. 16, no. 1, pp. 200–215, 2010.

[141] C. Dorrer and D. N. Maywar, 'RF Spectrum Analysis of Optical Signals Using Nonlinear Optics', *J. Light. Technol.*, vol. 22, no. 1, pp. 266–274, Jan. 2004.

[142] M. R. Dizaji, C. J. Krückel, A. Fülöp, P. A. Andrekson, V. Torres-Company, and L. R. Chen, ‘Silicon-rich nitride waveguides for ultra-broadband nonlinear signal processing’, *Opt. Express*, vol. 25, no. 11, p. 12100, May 2017.

[143] C. J. Krückel, A. Fülöp, T. Klintberg, J. Bengtsson, P. A. Andrekson, and V. Torres-Company, ‘Linear and nonlinear characterization of low-stress high-confinement silicon-rich nitride waveguides’, *Opt. Express*, vol. 23, no. 20, p. 25827, Oct. 2015.

[144] A. V. Velasco *et al.*, ‘High-resolution Fourier-transform spectrometer chip with microphotonic silicon spiral waveguides’, *Opt. Lett.*, vol. 38, no. 5, p. 706, Mar. 2013.

[145] R. Soref, ‘The Past, Present, and Future of Silicon Photonics’, *IEEE J. Sel. Top. Quantum Electron.*, vol. 12, no. 6, pp. 1678–1687, Nov. 2006.

[146] M. M. Milošević, N. G. Emerson, F. Y. Gardes, X. Chen, A. A. D. T. Adikaari, and G. Z. Mashanovich, ‘Athermal waveguides for optical communication wavelengths’, *Opt. Lett.*, vol. 36, no. 23, p. 4659, Dec. 2011.

[147] B. Guha, J. Cardenas, and M. Lipson, ‘Athermal silicon microring resonators with titanium oxide cladding’, *Opt. Express*, vol. 21, no. 22, p. 26557, Nov. 2013.

[148] T. Lipka, L. Moldenhauer, J. Müller, and H. K. Trieu, ‘Athermal and wavelength-trimmable photonic filters based on TiO_2-cladded amorphous-SOI’, *Opt. Express*, vol. 23, no. 15, p. 20075, Jul. 2015.

[149] L. He *et al.*, ‘Broadband athermal waveguides and resonators for datacom and telecom applications’, *Photonics Res.*, vol. 6, no. 11, p. 987, Nov. 2018.

[150] M. Uenuma and T. Motooka, ‘Temperature-independent silicon waveguide optical filter’, *Opt. Lett.*, vol. 34, no. 5, p. 599, Mar. 2009.

[151] J. H. Schmid *et al.*, ‘Temperature-independent silicon subwavelength grating waveguides’, *Opt. Lett.*, vol. 36, no. 11, p. 2110, Jun. 2011.

[152] M. Ibrahim *et al.*, ‘Athermal silicon waveguides with bridged subwavelength gratings for TE and TM polarizations’, *Opt. Express*, vol. 20, no. 16, p. 18356, Jul. 2012.

[153] P. J. Bock *et al.*, ‘Subwavelength grating periodic structures in silicon-on-insulator: a new type of microphotonic waveguide’, *Opt. Express*, vol. 18, no. 19, p. 20251, Sep. 2010.

[154] R. Halir *et al.*, ‘Colorless directional coupler with dispersion engineered sub-wavelength structure’, *Opt. Express*, vol. 20, no. 12, p. 13470, Jun. 2012.

[155] A. Maese-Novo *et al.*, ‘Wavelength independent multimode interference coupler’, *Opt. Express*, vol. 21, no. 6, p. 7033, Mar. 2013.

[156] D. Gonzalez-Andrade *et al.*, ‘Ultra-Broadband Mode Converter and Multiplexer Based on Sub-Wavelength Structures’, *IEEE Photonics J.*, vol. 10, no. 2, pp. 1–10, Apr. 2018.

[157] T. K. Liang and H. K. Tsang, ‘Nonlinear Absorption and Raman Scattering in Silicon-on-Insulator Optical Waveguides’, *IEEE J. Sel. Top. Quantum Electron.*, vol. 10, no. 5, pp. 1149–1153, Sep. 2004.

[158] T. . Mnatsakanov, A. . Schlögl, L. . Pomortseva, and D. Schröder, ‘Investigation of the optical, temperature dependent free-carrier absorption of a bipolar electron-hole plasma in silicon’, *Solid. State. Electron.*, vol. 43, no. 9, pp. 1703–1708, Sep. 1999.

[159] H. Podmore *et al.*, ‘Demonstration of a compressive-sensing Fourier-transform on-chip spectrometer’, *Opt. Lett.*, vol. 42, no. 7, p. 1440, Apr. 2017.

[160] P. R. Griffiths, ‘The Early Days of Commercial FT-IR Spectrometry: A Personal Perspective’, *Appl. Spectrosc.*, vol. 71, no. 3, pp. 329–340, Mar. 2017.

[161] M. C. M. M. Souza, A. Grieco, N. C. Frateschi, and Y. Fainman, ‘Fourier transform spectrometer on silicon with thermo-optic non-linearity and dispersion correction’, *Nat. Commun.*, vol. 9, no. 1, p. 665, Dec. 2018.

[162] Jeong Hwan Song *et al.*, ‘Bragg grating-assisted WDM filter for integrated optical triplexer transceivers’, *IEEE Photonics Technol. Lett.*, vol. 17, no. 12, pp. 2607–2609, Dec. 2005.

[163] A. Malik, M. Muneeb, Y. Shimura, J. Van Campenhout, R. Loo, and G. Roelkens, ‘Germanium-on-silicon planar concave grating wavelength (de)multiplexers in the mid-infrared’, *Appl. Phys. Lett.*, vol. 103, no. 16, p. 161119, Oct. 2013.

[164] P. Cheben *et al.*, ‘A high-resolution silicon-on-insulator arrayed waveguide grating microspectrometer with sub-micrometer aperture waveguides’, *Opt. Express*, vol. 15, no. 5, p. 2299, 2007.

[165] J. Huang, J. Yang, H. Zhang, J. Zhang, W. Wu, and S. Chang, ‘Analysis of Tunable Flat-Top Bandpass Filters Based on Graphene’, *IEEE Photonics Technol. Lett.*, vol. 28, no. 23, pp. 2677–2680, Dec. 2016.

[166] A. V. Velasco, P. Cheben, M. Florjańczyk, and M. L. Calvo, ‘Spatial Heterodyne Fourier-Transform Waveguide Spectrometers’, 2014, pp. 159–208.

[167] P. J. Bock *et al.*, ‘Subwavelength grating Fourier-transform interferometer array in silicon-on-insulator’, *Laser Photon. Rev.*, vol. 7, no. 6, pp. L67–L70, Nov. 2013.

[168] M. Nedeljkovic, A. V. Velasco, A. Z. Khokhar, A. Delage, P. Cheben, and G. Z. Mashanovich, ‘Mid-Infrared Silicon-on-Insulator Fourier-Transform Spectrometer Chip’, *IEEE Photonics Technol. Lett.*, vol. 28, no. 4, pp. 528–531, Feb. 2016.

[169] K. Okamoto, H. Aoyagi, and K. Takada, ‘Fabrication of Fourier-transform, integrated-optic spatial heterodyne spectrometer on silica-based planar waveguide’, *Opt. Lett.*, vol. 35, no. 12, p. 2103, Jun. 2010.

[170] D. M. Kita *et al.*, ‘High-performance and scalable on-chip digital Fourier transform spectroscopy’, *Nat. Commun.*, vol. 9, no. 1, p. 4405, Dec. 2018.

[171] A. Herrero-Bermello *et al.*, ‘Temperature dependence mitigation in stationary Fourier-transform on-chip spectrometers’, *Opt. Lett.*, vol. 42, no. 11, p. 2239, Jun. 2017.

[172] T. Shoji, T. Tsuchizawa, T. Watanabe, K. Yamada, and H. Morita, ‘Low loss mode size converter from 0.3 [micro sign]m square Si wire waveguides to singlemode fibres’, *Electron. Lett.*, vol. 38, no. 25, p. 1669, 2002.

[173] Y. Fu, T. Ye, W. Tang, and T. Chu, ‘Efficient adiabatic silicon-on-insulator waveguide taper’, *Photonics Res.*, vol. 2, no. 3, p. A41, Jun. 2014.